

AEDC-TR-95-36

C.1

**ARCHIVE COPY  
DO NOT LOAN**

## Initial Calibration of the AEDC Impulse Tunnel

James R. Blanks  
Sverdrup Technology Inc., AEDC Group

August 1996

Interim Report for Period October 1992 — September 1995

Approved for public release; distribution is unlimited.

TECHNICAL REPORTS  
FILE COPY

PROPERTY OF U. S. AIR FORCE  
AEDC TECHNICAL LIBRARY

**ARNOLD ENGINEERING DEVELOPMENT CENTER  
ARNOLD AIR FORCE BASE, TENNESSEE  
AIR FORCE MATERIEL COMMAND  
UNITED STATES AIR FORCE**

AEDC TECHNICAL LIBRARY



## NOTICES

When U. S. Government drawings, specifications, or other data are used for any purpose other than a definitely related Government procurement operation, the Government thereby incurs no responsibility nor any obligation whatsoever, and the fact that the Government may have formulated, furnished, or in any way supplied the said drawings, specifications, or other data, is not to be regarded by implication or otherwise, or in any manner licensing the holder or any other person or corporation, or conveying any rights or permission to manufacture, use, or sell any patented invention that may in any way be related thereto.

Qualified users may obtain copies of this report from the Defense Technical Information Center.

References to named commercial products in this report are not to be considered in any sense as an endorsement of the product by the United States Air Force or the Government.

This report has been reviewed by the Office of Public Affairs (PA) and is releasable to the National Technical Information Service (NTIS). At NTIS, it will be available to the general public, including foreign nations.

## APPROVAL STATEMENT

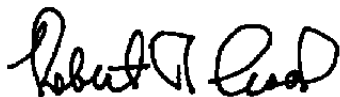
This report has been reviewed and approved.



RONALD T. BISHEL  
Technology Project Engineer  
Applied Technology Division  
Test Operations Directorate

Approved for publication:

FOR THE COMMANDER



ROBERT T. CROOK  
Asst. Chief, Applied Technology Division  
Test Operations Directorate

<b>REPORT DOCUMENTATION PAGE</b>			<b>Form Approved</b> <b>OMB No. 0704-0188</b>	
Public reporting burden for this collection of information is estimated to average 1 hour per response, including the time for reviewing instructions, searching existing data sources, gathering and maintaining the data needed, and completing and reviewing the collection of information. Send comments regarding this burden estimate or any other aspect of this collection of information, including suggestions for reducing this burden, to Washington Headquarters Services, Directorate for Information Operations and Reports, 1215 Jefferson Davis Highway, Suite 1204, Arlington, VA 22202-4302, and to the Office of Management and Budget, Paperwork Reduction Project (0704-0188), Washington, DC 20503.				
1. AGENCY USE ONLY (Leave blank)		2. REPORT DATE August 1996		3. REPORT TYPE AND DATES COVERED Interim Report for Period October 1992 - September 1995
4. TITLE AND SUBTITLE Initial Calibration of the AEDC Impulse Tunnel			5. FUNDING NUMBERS PE 65807F JN - 0116	
6. AUTHOR(S) Blanks, James R., Sverdrup Technology, Inc., AEDC Group				
7. PERFORMING ORGANIZATION NAME(S) AND ADDRESS(ES) Arnold Engineering Development Center/DOT Air Force Materiel Command Arnold Air Force Base, TN 37389-9011			8. PERFORMING ORGANIZATION (REPORT NUMBER) AEDC-TR-95-36	
9. SPONSORING/MONITORING AGENCY NAME(S) AND ADDRESS(ES) Arnold Engineering Development Center/DO Air Force Materiel Command Arnold Air Force Base, TN 37389-9010			10. SPONSORING/MONITORING AGENCY REPORT NUMBER	
11. SUPPLEMENTARY NOTES Available in Defense Technical Information Center (DTIC)				
12A. DISTRIBUTION/AVAILABILITY STATEMENT Approved for public release, distribution is unlimited.			12B. DISTRIBUTION CODE	
13. ABSTRACT (Maximum 200 words) Shakedown and calibration tests are being conducted in the new free-piston shock-heated Impulse Tunnel at AEDC. These tests have successfully demonstrated the facility's ability to produce high-velocity test gas at high density. The low-pressure calibration is considered completed. Nozzle stagnation pressures to 650 bar at enthalpies to 12.5 MJ/kg are available for test programs				
14. SUBJECT TERMS free-piston shock tube, stalker tube, real-gas aerodynamics			15. NUMBER OF PAGES 108	
			16. PRICE CODE	
17. SECURITY CLASSIFICATION OF REPORT UNCLASSIFIED	18. SECURITY CLASSIFICATION OF THIS PAGE UNCLASSIFIED	19. SECURITY CLASSIFICATION OF ABSTRACT UNCLASSIFIED	20. LIMITATION OF ABSTRACT SAME AS REPORT	

## **PREFACE**

The work reported herein was performed by the Arnold Engineering Development Center (AEDC), Air Force Materiel Command (AFMC), under Program Element 65807. The Air Force Program Manager was Mr. R. T. Bishel, DOT. The work was performed by Sverdrup Technology Inc., AEDC Group, support contractor for testing at the AEDC, AFMC, Arnold Air Force Base, TN. The work discussed in this report was performed in the impulse tunnel of the von Karman Gas Dynamics Facility (VKF) under AEDC Project Number 0116. The author appreciates the following individuals' contributions to the development and calibration of the Impulse Tunnel: Dr. J. R. Maus for development of the math model and data analysis; J. R. DeWitt for diaphragm development; and E. E. Edenfield for nozzle heat-transfer analysis. The manuscript was approved for publication on April 22, 1996.

## CONTENTS

	<u>Page</u>
1.0 INTRODUCTION .....	7
2.0 APPARATUS .....	7
2.1 Test Facility .....	7
2.2 Test Articles .....	12
2.3 Test Instrumentation .....	12
3.0 TEST TECHNIQUE .....	15
3.1 Calibration Runs .....	15
4.0 RESULTS AND DISCUSSION .....	18
4.1 Diaphragm Performance .....	18
4.2 Nozzle Reservoir Conditions .....	19
4.3 Pitot Rake Survey .....	20
4.4 Test Run Duration .....	20
4.5 Flow Field - Blunt Cone Interaction .....	21
4.6 Facility Math Model Comparison with Calibration Data .....	22
4.7 Computational Results and Comparison with Calibration Data .....	23
4.8 Flow-Field Contamination .....	24
5.0 CONCLUSIONS .....	25
REFERENCES .....	26

## ILLUSTRATIONS

<u>Figure</u>	<u>Page</u>
1. Light-Gas Gun and Shock Tunnel Components .....	29
2. Impulse Tunnel Layout .....	30
3. Downrange View of Powder Chamber and Compression Tube .....	31
4. Nozzle/Test Section Detail .....	32
5. The Impulse Tunnel Showing Nozzle Exit .....	33
6. Nozzle Insert Installation/Configuration .....	34
7. Projected Operating Envelope - Molier Diagram .....	35
8. Projected Operating Envelope - Altitude/Velocity .....	36
9. Shaped Diaphragm Dimensions .....	37
10. Diaphragm Test Rig .....	37
11. Diaphragm Burst Pressure Results .....	38
12. Facility Components and Initial Region Boundaries .....	38

**Figure**

	<b>Page</b>
13. Mass Points, Cells, and Regions .....	39
14. Pitot Rake Configuration .....	39
15. Calibration Model Dimensions .....	40
16. Impulse Facility Flow Probe .....	40
17. Location and Designation of Shock Tube Pressure Transducers .....	41
18. High-Pressure Section Pressure, Run 7 .....	42
19. Posttest Pistons and HPS Diaphragms .....	43
20. Piston Velocity Comparison to Math Model, Run 15 .....	44
21. Shock Tube Pressure Traces, Run 7 .....	44
22. Shock Wave Mach Number History .....	45
23. Comparison of Measured to Shock-Reflected Reservoir Pressure .....	46
24. Example of Non-Tailored Run .....	48
25. Visible Band Radiometer Helium Detector .....	49
26. Effect of Particulates on Rayleigh Scattering Helium Detector, Run 23 .....	50
27. Rayleigh Scattering Helium Detector .....	51
28. Calibration Cone Sidewall Pressures .....	52
29. Calibration Cone Surface Temperatures .....	53
30. Calibration Cone Heat-Transfer Rates .....	54
31. Math Model Comparison with Calibration Data .....	55
32. One-Dimensional Nozzle Computation, Run 13 .....	57
33. Computed Density Field and Measured Shock Shape, Run 16 .....	58
34. Computed Pressure Distribution on Test Article, Run 13 .....	58
35. Comparison of Computed Pressures at $X = 0.2526$ m with Data .....	59
36. Computed Heat-Transfer Distribution, Run 13 .....	59
37. Comparison of Computed Stagnation Point Heat Transfer with Measurement, Run 13 .....	60
38. Comparison of Computed Afterbody Heat Transfer with Measurement, Run 13 .....	60
39. Laser Beam Transmission Measurements .....	61
40. Flow Probe Measurements, Run 20 .....	62

**TABLES****Table**

	<b>Page</b>
1. Dimensions of Principal Components of the Impulse Facility .....	64
2. Impulse Facility Instrumentation .....	64
3. Impulse Facility Run Matrix .....	65

<u>Table</u>	<u>Page</u>
4. Nozzle Insert Materials and Performance .....	68
5. Nozzle Reservoir Conditions .....	69
6. Free-stream Conditions .....	71
7. Impulse Tunnel Spatial and Temporal Flow Variation .....	73
8. Math Model Predication of Gas Arrival Times .....	75
9. Calibration Cone Pressure Measurements .....	76
10. Flow Probe Average Heat-Transfer Rates .....	77

## APPENDICES

A. THERMAL ANALYSIS OF THROAT HEATING IN THE FREE-PISTON IMPULSE TUNNEL .....	79
NOMENCLATURE .....	102

## 1.0 INTRODUCTION

With the renaissance of hypersonics in the mid-1980's, the need for ground test facilities that can achieve flow conditions that simulate high-speed flight has re-emerged. In response to this need, the construction of a number of new test facilities has been undertaken in the U. S., Asia, and Europe. Among these facilities are several shock-heated devices that use adiabatic compression by a free piston to energize the driver gas. These free-piston shock tunnels have the capability to produce very high-velocity flow for a very short duration. Facilities of this type were pioneered by Stalker in the early 1960's (Ref. 1) and have undergone extensive improvements and upscaling by him and his colleagues at Australian National University and the University of Queensland. The latest of a series of Australian tunnels is designated T4 and is located at the University of Queensland (Ref. 2). A high-enthalpy free-piston shock tunnel (HEG) has been constructed at Göttingen, Germany, and located at DRL, German Aerospace Research Establishment (Ref. 3). The only free-piston shock tunnel currently operational in the U. S. is the GALCIT Tunnel T5 which began shakedown testing in late 1990 (Ref. 4).

As a part of the modernization of the AEDC G-Range (Ref. 5), a special-purpose impact range was constructed that can also be configured as a free-piston shock tunnel. In the shock tunnel mode, this facility will be referred to as the AEDC Impulse Tunnel. This device uses a gunpowder-propelled expendable piston, and has the potential for higher performance than other free-piston facilities currently in operation or being built. The Impulse Tunnel is directed toward flow-field measurements in air with a velocity regime where chemical nonequilibrium effects are important. The facility will also be able to conduct hydrogen combustion experiments at simulated hypersonic conditions. Calibration of the facility began in April 1993 and is a continuing effort supported by the AEDC Technology Program (Ref. 6). This report documents the initial calibration runs in the Impulse Tunnel.

## 2.0 APPARATUS

### 2.1 TEST FACILITY

#### 2.1.1 Description of Free-Piston Shock Tunnel

The similarities of both the hardware and operational cycles of a light-gas launcher and a free-piston shock tunnel are illustrated in Fig. 1. For a light-gas launcher, shown in the upper part of Fig. 1, a gunpowder charge accelerates a piston down the compression tube, compressing a light gas (usually hydrogen) to high pressure. At a prescribed pressure, a diaphragm ruptures, causing the projectile to be driven down the launch tube. The projectile is normally enclosed within a sabot to protect it during its travel down the launch tube. In the blast tank, the sabot is stripped from the

projectile and free flight continues to the target. For the free-piston shock tunnel, a moderate-to-high pressure propellant gas (usually air) accelerates a piston into a compression tube, compressing and heating a light driver gas (usually helium) to high pressure and temperature. This compression is a shock process rather than an isentropic process. At some prescribed pressure, the main diaphragm bursts, causing a shock wave to propagate down the shock tube, heating and compressing the test gas. The shock reflects from the end of the shock tube and processes the test gas a second time, bringing the test gas to rest. The shock-heated test gas expands through a nozzle to produce a hypervelocity test stream for a very short time (1-2 msec). The AEDC Impulse Tunnel uses gunpowder to drive a disposable piston with the potential of attaining nozzle stagnation pressures as high as 7,000 bar with enthalpies over 20 MJ/kg.

Figure 2 shows the principal components of the Impulse Tunnel. The compression tube, high-pressure section, and dump/target tank are common to both the free-piston shock tunnel and the impact range. Figure 3 shows a downrange view of the powder chamber and compression tube common to both facilities. In order to change from an impact model of operation to shock tube operation, the 6.35-cm-diam launch tube is replaced by a 7.62-cm bore by 12.19-m-long shock tube, coupled to an 8-deg semi-angle, 45.72-cm-diam exit conical nozzle. Figure 4 is a sketch of the nozzle and test section region of the tunnel. The dimensions of the major components are listed in Table 1.

The high-pressure section shown in Fig. 2 contains the primary diaphragm which is located at the end of the transition between the compression tube and the shock tube. This transition consists of a gradual taper over about 0.9 m, reducing the compression tube diameter from 20.3 to 19.7 cm, followed by a more rapid reduction of diameter to 7.62 cm over the last 0.3 m. The diaphragm region of the high-pressure section is designed to accommodate the opened diaphragm petals without restricting the flow. The high-pressure section and associated mass addition also acts as an inertial mass (15,500 kg) for the system, reducing the recoil of the shock tube and nozzle. The high-pressure section, shock tube, and nozzle throat region have a design pressure rating of 10,000 bar.

As shown in Fig. 4, the current nozzle for the Impulse Tunnel is an 8-deg half-angle cone with replaceable throat section. Figure 5 shows the nozzle exit and associated nozzle housing prior to assembly with the test section. A secondary Mylar® diaphragm is located near the nozzle throat to isolate the test gas in the shock tube from the evacuated test section and dump tank. The facility assembly includes the installation of the throat insert, and a 0.127-mm-thick Mylar diaphragm is shown in Fig. 6. There is a slip joint between the nozzle block and the test section housing to accommodate the recoil during tunnel operation. The test models are fixed with respect to the foundation, and the compression tube, high-pressure section, shock tube, and nozzle are allowed to slide in their mounts. The recoil is a function of piston mass and velocity with maximum move-

ment of 5.6 cm measured during the series of calibration runs. Good optical access is provided to the test section by four windows located just downstream of the nozzle exit plane. Current window configuration provides two 30-cm-diam viewing ports in each window frame.

### 2.1.2 Facility Testing Envelope

A plot of the nozzle stagnation conditions for a reflected shock tunnel with air as a test gas is shown in Fig. 7. The shock tube parameters used in this figure are the shock Mach number  $M_s$  and the initial pressure  $P_i$  in the test gas. The principal axes on this plot (Mollier Diagram) are stagnation enthalpy and dimensionless entropy. Also shown on the diagram are the test section velocity and simulated altitude assuming isentropic expansion of the test gas to the correct pressure. Lines of constant stagnation pressure are displayed. The envelope contained between shock Mach numbers of 8 to 14 represents the current goal for the Impulse Tunnel operating envelope. The plotted points represent calibration runs in the facility.

The asymptotic frozen composition of air, expanded from high-enthalpy reservoir conditions, can be conveniently correlated with reservoir entropy. Vertical lines on Fig. 7 show the mole fraction of monatomic oxygen predicted for the fully expanded test gas. The figure shows that high-pressure operation results in less dissociated oxygen in the test section flow. As noted, Fig. 7 is drawn for air, which is considered to be the primary test gas for this facility. The altitude scale of the abscissa of Fig. 7 is based on the entropy of a standard atmosphere. Thus, expanding isentropically from the given stagnation conditions to the atmospheric pressure will produce free-stream static conditions (temperature and density) that duplicate those in the atmosphere. Other test gases can be used, however, and offer advantages for certain applications. Pure nitrogen, for example, behaves more nearly like an ideal diatomic gas at typical high-enthalpy test conditions. In addition, nitrogen is a much more benign substance at high temperatures and pressures than oxygen, the other major component of air. Other test gases may be useful for certain applications.

Another method of presenting the Impulse Tunnel operating envelope is shown in Fig. 8. This envelope is based on the flow velocity and altitude, where the altitude is based on the density or pressure at the nozzle exit. The expansion from nozzle stagnation conditions was assumed to be isentropic and in equilibrium. The temperature of the gas at the above density/pressure altitude is not matched to the true temperature. Throat sizes from 0.95- to 1.91-cm diam are assumed which yield area ratios of 2304 to 576 for the present nozzle configuration.

### 2.1.3 Diaphragm Development

Operating the Impulse Tunnel over the full range of conditions indicated in Figs. 7 and 8 will require primary diaphragms that burst at pressures above 6,000 bar. A development program was initiated to determine the design criteria for these high-pressure diaphragms (Ref. 7). Experience with the hypervelocity launchers in the AEDC ranges has shown that flat burst diaphragms do not open properly above approximately 1,400 bar. This is a result of the required petal thickness as compared to the opening diameter for these flat diaphragms. Petals which are thick compared to the opening diameter typically tear at the corners, resulting in loss of petals during operation and damage to the facility hardware. Type 304 stainless steel has typically been used for these flat diaphragms because of its combined ductility and strength. Consideration of principles for design of high-pressure vessels led to a diaphragm of high-strength material made in a hemispherical shape for burst pressures above 1,400 bar. The development of the high-strength material hemispherical diaphragms was an extension of work done, circa 1960, in a 40-mm combustion gun at AEDC. Burst pressures up to 3,650 bar were obtained with diaphragms made from heat-treated ASTM 4130 bar stock. This approach was extended to the 7.62-cm size of the Impulse Tunnel shock tube and to burst pressures of 6,800 bar. The shaped diaphragm is shown in Fig. 9. The design parameters were selected such that changing the remaining metal thickness (RMT) under the crown to change the burst pressure determined the other dimensions. The RMT under the groove at the crown was maintained at 0.77 of the crown thickness ( $T_c$ ). The thickness at the base of the petals ( $T_b$ ) was  $1.3 T_c$ . The outside radius was 5.08 cm to match the cavity opening of the shock tube. The groove was 30-deg half-angle with a bottom radius of approximately 20 percent of groove depth. The groove depth was constant around the dome. Material was ASTM 4340 round bar stock heat-treated to Rockwell C 34-36. Although the design shown is for a six-petal diaphragm, the test program also included four-petal diaphragms.

Development tests of the diaphragms were carried out in a special test device, illustrated in Fig. 10, that was pressurized by igniting a fast burning gunpowder charge in the chamber. Two pressure transducers were used to determine the diaphragm burst pressure. Nineteen tests were conducted with the diaphragm test device; seven with flat diaphragms and the remainder with hemispherical diaphragms. A summary of the results is presented graphically in Fig. 11. In this figure the diaphragm burst pressure is plotted as a function of the remaining metal thickness (RMT) at the base of the grooves normalized by the inside radius of the hemisphere ( $R_i$ ) for shaped diaphragms. Also shown on this figure are similar results for flat diaphragms made of 304 stainless steel, where the normalizing dimension is the radius of the shock tube bore (3.81 cm). The advantage of the hemispherical design with high-strength material (ASTM 4340,  $R_c = 34-36$ ) is apparent from this plot. A least-square fit to these two sets of data resulted in the following equations for designing diaphragm burst pressures:

### For Flat Diaphragms, 304 SS

$$\text{Burst Pressure} = 7633(\text{RMT}/R_s) + 50 \text{ (bar)}$$

### For Shaped Diaphragms, ASTM 4340

$$\text{Burst Pressure} = 33622(\text{RMT}/R_s) - 87 \text{ (bar)}$$

## 2.1.4 Facility Math Model

Even for a fixed geometry, there are a large number of independent parameters that affect the test conditions and test time in a free-piston shock tunnel. The influence of these parameters cannot be accurately predicted by simple theoretical considerations such as elementary shock tube theory. For this reason, a mathematical model for the AEDC Impulse Tunnel has been developed to aid in specifying test conditions and predicting performance. A computer code (Ref. 8) based on a solution scheme for the one-dimensional gas dynamic equations developed by Von Neumann and Richtmeyer (Refs. 9 and 10) has long been used at AEDC to describe the G-Range launch cycle. This code has been modified to adapt it specifically for the free-piston shock tunnel. The physical layout of the device being modeled is shown in Fig. 12. The solution domain is divided into five regions, as illustrated in Fig. 12. Each of these regions is assumed to have its own equation of state and may be subdivided into a number of cells or zones. The equation set used is quasi-one dimensional in the sense that area variations are permitted along the duct. Figure 12 also illustrates the number and type of area changes that are currently allowed in the code.

In the Lagrangian scheme that is used in the solution technique, a system of mass points that describe the initial mass distribution is labeled and tracked as the flow field evolves with time. Mass points containing one-half the mass of each of two adjacent cells are assumed to reside at the interface of the two cells. The dependent thermodynamic variables  $P$ ,  $V$ , and  $E$  are computed in the interior of the cell between mass points  $J$  and  $J + 1$ . This is illustrated in Fig. 13. To advance the solution one step in time, Newton's Second Law is applied to each mass point to compute its velocity and displacement. Next, conservation of mass is then applied to determine the specific volume  $V$  in each fluid cell. The energy equation and an equation of state are solved together for pressure  $P$  and energy  $E$  to complete the calculation for one time step.

Friction losses and heat transfer to the wall are included in the momentum and energy equations, respectively, in the compression tube and the shock tube. A friction coefficient and Stanton number are input parameters to the calculation. Equations of state for an ideal gas, equilibrium air, equilibrium nitrogen, and a pressure-volume relation appropriate for the plastic piston material are included in the formulation. A model for burning gunpowder that has been used

for the G-Range Launcher Code (Ref. 11) was retained. The mathematical model also includes the option to include the effective test gas loss due to the growth of the boundary layer in the shock tube. This boundary-layer option has a minor influence on computed shock speed but substantially reduces the time at which helium first arrives in the facility test section.

## 2.2 TEST ARTICLES

Three test articles have been used in the Impulse Tunnel to measure and evaluate the quality of the test flow and its effect on a typical blunt body configuration. An array of pitot probes has been used to assist in evaluation of the uniformity and duration of the test gas flow. A sketch of this instrument is shown in Fig. 14. The pitot probe spacing was 5.08 cm, which provides a survey of the core flow of 30.48-cm diameter. The probe data do not extend into the boundary-layer region at the nozzle exit. The hemispherical elements shown on the vertical array were included in an unsuccessful attempt to use noscap radiation for determining helium arrival. In the future, the hemispheres will be fitted with coaxial thermocouples to measure stagnation point heat transfer. A blunt cone, shown in Fig. 15, was used on selected runs during the calibration program. The calibration cone was instrumented with four equally spaced pressure transducers (C1, C2, C3, and C4) located on the sidewall near the cone base at a streamline distance of 26.64 cm, at axial station  $X/L = 0.8$ . The initial selection of pressure gage type was based on the maximum estimated facility operational pressure (7,500 bar) which resulted in the installation of 100-psi PCB® transducers (Model No. 113A02). These gages proved to be unacceptable for the lower pressure run conditions and were replaced by 5-psi Kulite® transducers (Model No. XCS-093-5D). The body was fitted with a like number of coaxial thermocouple gages (T1, T2, T3, and T4) at axial station,  $X/L = 0.8$ . The thermocouple gage and pressure gage were mounted 15 deg apart with a 90-deg spacing between each group. A coaxial thermocouple (T5) at the stagnation point was also included. Both copper and stainless steel have been used for the replaceable nosetip. The calibration cone provides a representative configuration for the evaluation of the effects of hypersonic flow. A flow probe containing five coaxial thermocouples was also used on selected runs during the calibration program. The probe configuration and thermocouple channel identification are shown in Fig. 16. This probe is similar in design to contamination probes used in AEDC Tunnel F during the 1970's. Probes of this type were used to make judgments concerning the concentration of solid particles in the flow produced in the arc heating/vaporization process with a resolidification during the nozzle expansion.

## 2.3 TEST INSTRUMENTATION

### 2.3.1 G-Range Data System

The G-Range data acquisition and control system (GDACS) is used in the Impulse Tunnel for all control and selective data logging functions. The GDACS is composed of the HCS (Host Computing Subsystem), TMS (Time Measurement Subsystem), SDS (Static Data Subsystem),

TDS (Transient Data Subsystem), FCS (Fire Control Subsystem), ECS (Event Control Subsystem), and BCS (Bus Control Subsystem.).

The HCS is a multi-user, multi-tasking computing system that supports the GDACS subsystems. Four terminals can be used at any time to permit simultaneous pre-operation and post-operation tasks to occur on the G-Range and Impulse/Impact Facilities without interference. All setups for the other subsystems (TMS, ECS, FCS, SDS) are completed by the HCS prior to a run. All subsystems must verify to the HCS that they are set up properly and ready to continue before the run is initiated. Once the countdown starts, the HCS is used only to abort the run. All control is turned over to the FCS and ECS. After the run is completed, the HCS gathers all data from the TMS and archives them on the hard drive. The TMS has an internal clock with a 10-nsec resolution to time stamp the collected data. The SDS is the subsystem used to gather static data, which consist primarily of facility pressure and temperature data. The FCS turns equipment on and off that is time sequential in nature and generates the fire command for the run. The ECS triggers equipment in the tunnel during the run using preset delays, if required.

#### 2.3.1.1 Transient Data Subsystem

A transient data subsystem that records pressure, facility recoil, heat flux gage response, and other data consists of individual channels of A/D converters and memory. Forty-eight channels are dedicated to the Impulse Tunnel, and an additional 80 channels are available from G-Range as the testing schedule permits. The standard sample rate for the Impulse Tunnel transient data measurements is 0.2 MHz per channel and 128 K data points per channel. Amplitude resolution is 12 bits. The large data memory for each channel allows triggering of each channel when the gunpowder is ignited, minimizing the possibility of improper triggers and lost data. This system can be reconfigured to provide faster or slower sampling rates.

#### 2.2.2 Standard Facility Measurements

The principal facility transient instrumentation are pressure transducers installed at various positions in the facility (see Table 2). Piezoelectric type (PCB®) pressure transducers are used on the facility. The location of the pressure gages along the shock tube and their designation are shown in Fig. 17. These gages provide information on the incident shock speed which, as shown by Fig. 7, is closely related to the stagnation enthalpy of the test gas. The gage designated ST6 gives the reservoir pressure for the conical nozzle. The gage designated HPS2 is just upstream of the main diaphragm and provides information on the time and driver gas pressure at diaphragm burst. Static pressures along the last third of the nozzle wall are also measured. A linear voltage differential transformer (LVDT) is used to measure the facility recoil during the run. Static-type pressure gages are used to measure the pretest charge in the compression tube, shock tube, and the dump tank vacuum.

### 2.2.3 Schlieren

The Impulse Tunnel is equipped with a system of schlieren-quality optics arranged in the classical single-pass (or z) configuration. This flow visualization system can be employed in any one of several operational modes: horizontal or vertical knife-edge schlieren, color schlieren, dark-field schlieren interferometer, or focused shadowgraph. This system can also be arranged for holographic recording and later reconstruction in a schlieren, shadowgraph, or interferometer. Flow details of special interest during a particular test are considered in selecting the optical configuration in which the system is operated. A pulsed ruby laser provides the light source to produce a single photographic image.

### 2.2.4 Nonintrusive Measurement Systems

The concurrent technology development of nonintrusive flow diagnostics is a companion effort to test and evaluation of the Impulse Shock Tunnel at AEDC. The requirements for measurement technology are to characterize both the free-stream flow approaching the test article and the local test article flow field, with particular emphasis on the aerodynamic parameters most sensitive to the high-temperature conditions of the test gas. The static properties of the test gas of most interest are the vibrational and rotational temperatures and the concentrations of major flow species ( $N_2$ ,  $O_2$ ,  $NO$ ,  $O$ ). Other instrumentation requirements stem from the nature of high-pressure shock tunnels, where the actual run duration and the relative cleanliness of the flow must be determined experimentally. Nonintrusive diagnostic solutions for the specified requirements are centered on the fluorescence diagnostics in development for both arc and shock tunnel applications. With the first goal for simultaneous, 2-D,  $NO$  concentration and rotational temperature measurements, a development path that included a Planar Laser-Induced Fluorescence (PLIF) system for  $NO$  measurements, a means to compare images to CFD predictions, and subsequent dual PLIF- $NO$  measurements has been followed.

PLIF- $NO$  measurements were successfully acquired during initial Impulse Tunnel shake-down testing (Ref. 13). Image processing and data analysis methods were developed to process raw images into fluorescence intensity maps. Comparison of measured PLIF images to CFD predictions was provided by extending the algorithms of typical CFD prediction codes with a spectro-physical model, providing theoretical fluorescence intensity maps. Following the successful acquisition of PLIF images in Impulse testing, refinement of both experimental and theoretical data analysis methods has continued (Refs. 14 and 15). In follow-on testing, a dual PLIF system was successfully demonstrated, acquiring two essentially simultaneous images of fluorescence from different  $NO$  transitions. Demonstration of flow-monitoring diagnostics (Ref. 16) includes acquisition of Filtered Rayleigh Scattering measurements that reveal the arrival of helium in the driver gas, and thus determine the end of the test run. Emission measurements from

the stagnation region of the blunt cone test article identify the presence of atomic copper and atomic iron contaminants in the flow. Also, visual laser beam transmission measurements have verified the presence of particulates during intermittent failures of key facility components (nozzle throat, liner) as the operational pressure is pushed to new high limits.

### 3.0 TEST TECHNIQUE

Preparation of the Impulse Facility for a run includes a pretest cleaning of the powder chamber, compression tube, high-pressure section, and shock tube. The high-pressure diaphragm is installed and the joints between the nozzle throat block and downrange end of shock tube, shock tube to high-pressure section, and high-pressure section to compression tube are assembled. The assembled facility is then positioned to the prefire location with respect to the test article. The usual prefire location leaves a gap of 12.7 mm between the nozzle exit and the nose of the test article. The facility transient pressure transducers are checked and installed prior to the run. An expendable piston is loaded in the uprange end of the compression tube prior to loading of the powder charge. Personnel are excluded from the test area during a run. The evacuation and purging of air from the compression and shock tube is a remote operation. The compression tube is charged with helium to the desired level, and the shock tube is charged with pure air to the required level. The facility is fired by the GDACS.

#### 3.1 CALIBRATION RUNS

The run conditions and results of the first 25 runs in the Impulse Tunnel are summarized in Table 3 and are indicated by the filled circles on Figs. 7 and 8.

The compression tube charge pressures and HPS diaphragm burst pressures were selected to produce isentropic compression ratios which varied between 22 and 41. Assuming that helium is an ideal gas, the following equations were used to calculate the isentropic compression:

$$r_v = (P_4/P_3)^{1/\gamma} = (P_4/P_3)^{0.6}$$

$$T_4 = T_3(P_4/P_3)^{(\gamma-1)/\gamma} = T_3(P_4/P_3)^{0.4}$$

where

- $r_v$  = isentropic compression ratio =  $V_i/V_f$
- $P_3$  = initial compression tube charge pressure
- $P_4$  = high-pressure section diaphragm burst pressure
- $T_3$  = initial helium temperature
- $T_4$  = helium temperature at diaphragm burst pressure
- $\gamma$  = ratio of specific heats for helium
- $V_i$  = initial helium volume
- $V_f$  = final helium volume at diaphragm burst

For piston velocities typical of this facility, the helium compression is a shock-type process. Therefore, the actual compression ratio is less than the isentropic process. The actual temperature of the helium at diaphragm burst is higher than that in an isentropic process (see Table 3). Figure 18 is an example of the pressure trace generated at HPS2, just upstream of the diaphragm station, and illustrates the shock compression process with step increases in the pressure level. This figure also illustrates the difficulty in determining the exact time and pressure at which the diaphragm bursts.

Most of the diaphragms employed for the calibration runs were of the flat design, fabricated from type 304 stainless steel plate. Based on petal thickness considerations, the flat design is used for all burst pressures up to 1,380 bar. The hemispherical diaphragms described in Section 2.1.2 were used on Runs 14, 18, 22, and 25. Note that the diaphragms did not open fully for the first two runs. The diaphragms for both of these shots were the flat six-petal design, a type successfully used in the G04 launcher. Although this diaphragm had been tested in the diaphragm test rig and had performed satisfactorily in that situation, the design did not work well in the Impulse Tunnel. All diaphragms for the remaining runs were of a four-petal design which opened fully for most runs. The burst pressures given in Table 3 are the nominal values based on the data from the diaphragm tester.

The pistons used during the calibration runs are an expendable item, similar in design to those used in the hypervelocity two-stage launchers. They are fabricated with a polyethylene outerbody and an internal lead slug to provide the desired mass; see Fig. 19 for photographs of posttest pistons and diaphragms from Runs 23 and 25. The piston is driven into the tapered portion of the high-pressure section, HPS, during operation. At the higher piston velocities, the piston is normally recovered in three pieces: front section of polyethylene, center section of lead deformed to HPS diameter, and a rear section of polyethylene. A lip seal is used on the front face of the piston to prevent blowby of high-pressure gas. The piston mass for all of the runs shown in Table 3 was approximately 77.6 kg. Piston masses ranging from 77.6 to 180 kg are available.

The gunpowder charges were selected to produce a certain maximum piston velocity. The difference between the 105-mm and the 155-mm gunpowder is grain size. The 105-mm gunpowder is finer grained and, consequently, faster burning. This type of powder is preferred for light powder charges because it produces better repeatability. Six piston probes, spaced over the last 6 m of the compression tube, permit measurement of the piston velocity through this region. Figure 20 presents the measured piston velocity for Run 15, compared to the math model prediction. The measured maximum piston velocity was 338.34 m/sec, compared to the calculated value of 341.73 m/sec over the same interval. It will be noted that the piston approaches its maximum velocity after a short travel distance and maintains a relatively constant velocity for the majority of its motion. Piston velocities from 240 to 495 m/sec have been used on the current calibration runs.

Four materials have been used for nozzle inserts during the test program to date: molybdenum, TZM, Fansteel-60® (90-percent Ta, 10-percent W), and tungsten alloy (80-percent W, 20-percent Cu). The remarks column of Table 3 indicates some of the material problems which have been encountered. The initial facility runs were made using molybdenum and TZM throat inserts because of their high melt temperature, thermal conductivity, and heat capacity. Materials that have a relatively large value for  $\rho c_p K T_m^2$  are potentially better for resisting the ablation associated with the high heating loads produced in reflected shock facilities (see Appendix A). Unfortunately, the molybdenum and TZM throat inserts develop cracks after one or two runs, resulting in a mechanical failure of the part. The Fansteel-60 and tungsten alloy throats have proved to be much more durable and have withstood the environment produced by the test conditions run to date. Table 4 presents performance data for the various throats with respect to runs to failure. All runs except two have been made with a 19.05-mm-diam throat which produces an area ratio,  $A_{exit}/A^*$ , of 576. The two exceptions had a throat diameter of 12.7 mm with an area ratio of 1296.

The values of average shock Mach number given in Table 3 are calculated from measured shock tube pressure data at ST2 and ST6 (see Fig. 17). Figure 21 shows examples of shock tube pressures for the last four measurement stations ST3-ST6. There is clear evidence that the shock is slowing as it progresses along the tube, as indicated in Fig. 22. The data are plotted for a combination of all available intervals. The reflected shock Mach number is obtained by extension of the plotted data to the distance representing the end of the shock tube (12.2 m). Pressure transducer ST6 measures the stagnation pressure or the reservoir pressure for the nozzle. The values for stagnation pressure given in Table 3 are determined using engineering judgment by inspecting the ST6 pressure traces. Based on the ST6 pressure distribution for Run 7, one would infer a useful run time of greater than 2 msec for approximately uniform pressure. The useful run time based on helium arrival in the test section cannot be determined from these pressure data. For most of the runs in Table 3, the initial shock tube pressure was set at a level designed to produce a tailored interface (Ref. 17) in order to maximize the pressure plateau and produce a long run time.

This objective was reasonably well achieved in Run 7. Figure 23 presents data on the reservoir pressure for Run 19 where the shock tube charge conditions did not produce a tailored run.

In the original facility installation, the shock tube was fabricated of high-strength steel. At diaphragm burst pressures above 1,200 bar, the downrange end of the steel shock tube was eroded due to the high heat flux in that area. After the first eight runs, the calibration program was interrupted to provide a copper liner for the last 0.45 m of the shock tube. The balance of the runs shown in Table 3 were made with the copper liner in place. The data indicate that the copper liner is a satisfactory material for reservoir pressures up to 1,000 bar.

## 4.0 RESULTS AND DISCUSSION

### 4.1 DIAPHRAGM PERFORMANCE

The initial two calibration runs indicated that the petaling performance in the diaphragm test rig and in the facility were different. The six-petal flat diaphragm design used on the first two runs performed satisfactorily in the test rig but did not open fully in the facility. This difference in performance of the flat diaphragms is likely attributable to the difference in the pressure loading in the test rig and in the facility (see Ref. 7). For this reason, all later calibration runs in the Impulse Tunnel used a four-petal design which provided better petaling performance. The diaphragm burst pressure measured in the test rig is a good indication of the burst pressure experienced in the facility. However, it is possible to generate a higher effective helium pressure at burst due to the step shock compression process shown in Fig. 18.

A number of runs have been made with flat diaphragms having a burst pressure of 1,380 bar (see Table 3). These diaphragms do not open fully due to their 9.65-mm petal thickness. The average open area for this burst pressure is 26.4 cm<sup>2</sup>, as compared to 45.6 cm<sup>2</sup> for a full open diaphragm. This condition tends to reduce the performance of the run by reducing the magnitude of the shock Mach number. The lower burst pressure flat diaphragms (690 and 1,035 bar) tend to open more fully due to the thinner petal thickness.

The petaling performance of the four-petal hemispherical diaphragms was good in all of the calibrations runs. The first run with a shaped diaphragm (Run 14) identified a problem with the counterbore in the uprange end of the shock tube. This counterbore (10.16-cm-diam) which accommodates the open diaphragm petals did not have sufficient depth. Therefore, the tips of the diaphragm were broken off on this run. The shock tube was modified by increasing the depth of the counterbore prior to additional runs with the shaped diaphragms. A problem was encountered on Run 25 which used a hemispherical diaphragm with a burst pressure of 2,760 bar. The tips of this shaped diaphragm were broken off during the opening process, resulting in minor facility

damage. The impact of the petal tips on the counterbore surface, coupled with the somewhat brittle behavior of the 4340 hardened material ( $R_c = 34-36$ ), are contributing factors to the tip failures.

Two runs were made in which the material lost by the diaphragm was determined by a pretest and posttest weighing using scales with a least count of 1 mg. On Run 24, which used a flat diaphragm, a total of 16 mg was lost. This loss compares favorably with the GALCIT Tunnel T5 experience of 10 to 100 mg of diaphragm material lost during their runs. On Run 25, which used a hemispherical diaphragm, 28.642 gm of material was lost. The diaphragm tips were lost on this run, which accounts for the large amount of lost material.

## 4.2 NOZZLE RESERVOIR CONDITIONS

The nozzle reservoir stagnation conditions attained during the Impulse Tunnel calibration are presented in Table 5. The reflected shock Mach number was determined from an analysis of the shock wave Mach number history with an extension of the data to the downrange end of the shock tube. An example of this type of data is shown in Fig. 22. Using the initial shock tube charge pressure  $P_1$  and the reflected shock Mach number, the reflected shock conditions were determined. The final nozzle stagnation conditions ( $H5'$ ,  $T5'$ ) were determined using the assumption that an isentropic process occurred from the reflected shock pressure ( $P5$ ) to the measured (ST6) reservoir pressure ( $P5'$ ). The final state conditions were determined using curve-fitted equations for equilibrium air (Ref. 18). The calculated reflected shock pressure  $P5$  and the measured nozzle reservoir pressure  $P5'$  (ST6) are shown in Fig. 23 for two of the calibration runs. The reflected shock pressure level can be considered the theoretical "tailored" value which would be obtained if the reflected shock waves passes through the helium-air interface without generation of additional compression or refraction waves which reprocess the reservoir gas. The data shown in Fig. 23a for Run 7 are an example of near "tailored" run conditons. A non-tailored run condition is shown in Fig. 24, where the multiple shock reflections between the nozzle entrance and the helium-air interface are well defined.

The nozzle reservoir conditions were used in an isentropic, real gas, expansion under equilibrium conditions to estimate the free-stream test conditions (see Table 6). An estimate was also made of a model's stagnation conditions when exposed to these free-stream conditions. Also listed are the heat-transfer rates expected from the flow conditions based on the Fay-Riddell method for a model with a nose radius of 1.78 cm, which corresponds to the calibration model shown in Fig. 15.

### 4.3 PITOT RAKE SURVEY

The pitot rake shown in Fig. 14 was used to evaluate the uniformity of the test section flow on Runs 1 through 8 (see Table 7). No pitot data were obtained on Run 1 due to an incorrect setup of the data recording system. Since the high-pressure section diaphragm did not burst on Run 4, no flow was generated on this run. The spatial and temporal variation in pitot probe measurements are presented in this table. The spatial variation in the flow ranged from 2.6 to 12.4 percent. The temporal variation in pitot probe measurements ranged from 4 to 13.4 percent, with lower values associated with those runs which were more nearly "tailored" conditions. All runs were analyzed with a time slice of 1 msec, except Run 5, which used a 1.27-cm-diam nozzle throat, and was averaged over a 2-msec period.

### 4.4 TEST RUN DURATION

The test run duration is an important consideration in the analysis of data from a free-piston shock tunnel. Since the arrival of helium in the test section determines the usable testing period, it is necessary to know the arrival time of the test gas (air) and the helium with respect to the test measurements. It is not possible to determine these arrival times from an inspection of data recorded by pressure and heat-transfer gages. The facility math model with the turbulent boundary-layer option was used to estimate the arrival times of the air and helium at the entrance and exit of the nozzle (see Table 8). The normal flow area at the high-pressure section diaphragm location is 45.6 cm<sup>2</sup> and is shown with a reduced flow area on some runs in which the diaphragm did not open fully. It is suggested that the delta time between the arrival of the air and helium at the nozzle exit be used as the theoretical test time. Since the math model assumes a perfect interface between the air and helium with no mixing, the actual test time will be shorter than the theoretical test time. The math model predictions indicate theoretical test times in the 2.5- to 4.3-msec range for the calibration runs made to date.

A hemispherical probe was mounted on the pitot rake during the initial runs in the Impulse Facility. A broadband unfiltered visible radiometer, S20, was focused on the stagnation region of this probe to determine the arrival of helium at this location. It was speculated that the reduction in shock cap radiation due to the arrival of helium would be detectable in the radiometer output. An example of the radiometer output is shown in Fig. 25, along with the theoretical run time. The initial spike in the radiometer output is thought to be associated with the nozzle start phenomenon. These data indicated that the radiometer output was not a reliable indication of the helium arrival in the test section.

A second technique for determining the arrival of helium in the test section is under investigation. A Filtered Rayleigh Scattering system was operated on Runs 16 through 25. In

theory, this system should have a significantly different output when traversing air and helium due to their differences in scattering cross section. At least two problems complicate the analysis and definition of helium arrival. It is speculated that a significant zone exists which contains a mixture of helium and air, so no instantaneous change in the recorded signal is evident in the data. The presence of particulates, including facility ablation products, affects the measurements of the Filtered Rayleigh Scattering system. The particulates complicate the identification of the signal drop (see Fig. 26) normally indicative of the decreased molecular Rayleigh scattering cross-section of flow dominated by the helium driver gas. Additional examples of the Rayleigh scattering data are presented in Fig. 27, along with the estimated theoretical test times predicted by the facility math model. These data indicate the difficulty in determining helium arrival in the test section using the Filtered Rayleigh Scattering technique.

#### 4.5 FLOW-FIELD — BLUNT CONE INTERACTION

The calibration cone (see Fig. 15) was used on Runs 9 through 25 as a representative simple configuration for the evaluation of the effects of hypersonic flow. The cone bluntness of 25 percent generates stagnation conditions where a significant quantity of gas is processed through a near-normal shock, resulting in dissociation and real-gas effects which persist in the boundary-layer flow.

The resulting cone pressure measurements and their standard deviations are presented in Table 9. Typical cone pressure measurements as a function of time are shown in Fig. 28 with all data processed through a low-pass (10,000 Hz) Butterworth filter prior to plotting.

The calibration cone was also instrumented with four equally spaced coaxial thermocouples (T1, T2, T3, and T4) located on the sidewall near the cone base at a streamline distance of 26.64 cm. A fifth thermocouple (T5) was mounted at the model stagnation point. The coaxial surface thermocouples (Type E) were selected for making transient heat-flux measurements in the transient hypersonic flow environment of the Impulse Tunnel. The principle of operation of the coaxial surface thermocouple normally assumes that the entire assembly is a homogeneous semi-infinite solid. This includes the model material, as well as the thermocouple elements. The equation (Ref. 19) used to extract timewise heat-flux data is shown below:

$$q(t) = \frac{2\sqrt{\rho C_p} K}{\sqrt{\pi}} \left[ \sum_{i=1}^n \frac{T_i - T_{i-1}}{(t_n - t_i)^5 + (t_n - t_{i-1})^5} \right]$$

where  $\rho$ ,  $C_p$ , and  $K$  are the density, specific heat, and thermal conductivity, respectively, of the coaxial assembly.  $T$  is the temperature rise of the sensing surface and  $t$  is time. The value of the constant,  $\sqrt{\rho C_p K}$ , used in the data reduction was 0.425 where

$$\begin{aligned}\rho &\text{ is in gm/cm}^3 \\ c_p &\text{ is in cal/gm-}^\circ\text{K} \\ K &\text{ is in watt/cm-}^\circ\text{K}.\end{aligned}$$

which was considered appropriate for the measured temperature range of the Chromel® outerbody. A detailed description of a typical installation and data reduction techniques can be found in Refs. 20 and 21. The coaxial thermocouple measurements of stagnation and sidewall temperature are shown in Fig. 29 for two run conditions. The resulting heat-transfer rates for the measured surface temperatures are presented in Fig. 30. The maximum stagnation point heat-transfer rates for Runs 10 and 13 were 4,000 and 2,500 w/cm<sup>2</sup>, respectively. The sidewall heat-transfer rates for these same two runs were in the range of 100 to 150 w/cm<sup>2</sup>. These data indicate the importance of having clean, noise-free data from the thermocouples. The sidewall gages measure a small temperature increase during the run and are subject to problems with noise in the recorded signal.

#### 4.6 FACILITY MATH MODEL COMPARISON WITH CALIBRATION DATA

Facility pressure measurements have been compared to the math model predictions for two of the calibration runs (see Fig. 31). The math model described in Section 2.1.3 was exercised using the turbulent boundary-layer option to predict the pressures at selected measurement locations. Figure 31a for Run 8 shows the comparison for shock tube gage ST6 which measures the nozzle stagnation pressure. The relative agreement between the measured and calculated value is seen to be good; however, the calculated values do not track the spikes in the measured data. Figure 31b shows a similar comparison between computed pitot pressure at the nozzle exit plane and the measurement from the center rake probe, PT4. The computed distribution assumes that the pitot pressure is given by  $\rho U^2$ , twice the dynamic pressure. Again, the overall level of the pitot pressure is predicted fairly well. Figures 31c-d present data on shock tube pressure gages ST5 and ST6 for Run 21. Since the high-pressure section diaphragm did not open fully on this run, the orifice option in the math model was used to approximate this restriction to the helium flow. As shown previously, there is excellent agreement between the measured and calculated pressure distribution. In general, it appears that the math model can predict the facility performance reasonably well.

## 4.7 COMPUTATIONAL RESULTS AND COMPARISON WITH CALIBRATION DATA

A substantial computational effort is associated with the calibration of the Impulse Facility (see Ref. 22). Several CFD codes are being used in conjunction with the free-piston shock tunnel to aid in selecting run parameters and interpreting data. The fact that the free-stream flow is generated with a conical nozzle and contains nitric oxide (NO) and monatomic oxygen must be accounted for in comparing data with theoretical predictions. The most efficient way to make such comparisons is to carry out CFD solutions over the test article using free-stream conditions that model as nearly as possible the actual tunnel free stream. One of the advantages of using CFD as an integral part of the calibration program is to be able to tie together, in a coherent manner, data gathered under very different conditions by different instrumentation packages. One of the principal CFD codes used in the analysis of data from the Impulse Facility is the three-dimensional, thin-layer Navier-Stokes code TUFF (Ref. 23) developed at NASA Ames. This code solves the strongly coupled species conservation equations in a finite-volume framework. A time-marching algorithm is used in conjunction with Total Variation Diminishing (TVD) techniques to obtain an asymptotic steady-state solution. No attempt is made to model the transient nature of the flow. The second CFD code being used in the analysis of data is NEDANA (Ref. 24) developed by Rock and Tramel at AEDC. NEDANA employs a three-dimensional, time-accurate, locally implicit algorithm for the solution of the thin-layer Navier-Stokes equations expanded for thermochemical nonequilibrium. The code employs the AEDC-developed chemistry package NEQPAK (Ref. 25) which provides the chemical, thermodynamic, and transport properties required to simulate the flow of a gas in thermochemical nonequilibrium. Two-dimensional axisymmetric computations were performed to model the flow about the blunt-cone calibration model. These computations differ from those produced by TUFF, primarily because they account for the partitioning of the energy between the translational-rotational and vibrational-electronic energy modes.

From the nozzle stagnation conditions, an isentropic equilibrium expansion of the test gas is carried out to the nozzle throat. The conditions at the throat, including the mass fractions of the constituent gases, are used as upstream boundary conditions for a one-dimensional nonequilibrium flow calculation for the diverging portion of the nozzle. This calculation and others in the solution can be carried out with either TUFF or NEDANA, depending on whether thermal nonequilibrium is considered important for the final application of the results. Figure 32 shows some of the results of the one-dimensional computation in the diverging portion of the nozzle for Run 13. As expected, the rate of increase of velocity drops quickly in the diverging part of hypersonic nozzles. Despite a large area ratio ( $A/A^* = 576$ ), the exit Mach number is computed to be 7.40 because of the real-gas effects. Both monatomic oxygen and NO have frozen out well before the end of the nozzle,  $X = 1.6$  m.

Figure 33 shows the distribution of density about the test article computed with TUFF for free-stream conditions corresponding to Run 16. The nozzle exit conditions for this run were computed to be  $\rho_e = 0.008605 \text{ kg/m}^3$ ,  $U_e = 4,514 \text{ m/sec}$ , and  $M_e = 7.307$ . The upper part of the figure presents results for a computation with a conical free stream, and the lower part of the figure is for a uniform free stream. The experimental shock shape extracted from a schlieren photograph is also shown. As expected, the shock computed for the conical flow fits the experimental data better than that computed for a uniform free stream.

Figure 34 shows two independently computed pressure distributions along the calibration body for free-stream conditions corresponding to Run 13. Both computations assume a conical free-stream flow. The pressure taps on the model are located at a surface distance of  $S = 0.26 \text{ m}$  from the nose. Figure 35 shows the pressure trace from one of these transducers compared with the predicted pressure levels for a uniform free stream and a conical free stream. The level of the measurement during this period suggests that there is some contouring of the flow by the nozzle boundary layer.

A plot of the dimensionless heat transfer computed with TUFF along the blunt cone for Run 13 is given in Fig. 36. Two distributions (both for a conical free-stream flow) are given, one for a non-catalytic wall, and the other for a fully catalytic wall where only diatomic oxygen and nitrogen are allowed at the surface.

Figure 37 compares the computational results with data obtained from a coaxial thermocouple gage at the stagnation point. Also shown on this figure is the value given by Fay-Riddell theory for a boundary layer in chemical equilibrium. The stagnation point heat transfer gives a good indication of the duration of the test. The 2 msec between 101 and 103 msec after fire pulse are considered to represent the test period for this run. The CFD solution for a fully catalytic wall agrees better with the data in this time interval than the solution for a noncatalytic wall. Also shown on this figure is a solution for flow at the stagnation point in chemical equilibrium. It is interesting that the equilibrium solution yields a heat-transfer rate that is closer to the noncatalytic wall than the fully catalytic wall. Figure 38 shows a comparison of computed heat-transfer rate for Run 13 with data for a gage on the cone frustum for a conical free-stream flow. Although the after-body heat transfer is more ambiguous than the heating at the stagnation point, the fully catalytic wall solution agrees better with the measured heating rate during the test period.

#### 4.8 FLOW-FIELD CONTAMINATION

One shortcoming of all high-energy shock tunnels is the contamination of the flow with facility ablation products from the nozzle throat and shock tube wall areas. The contamination becomes more severe as the enthalpy and pressure of the reservoir gas is increased. A visible laser

beam transmission detector is being used to monitor the facility flow. Results from this detector are plotted in Fig. 39 for a moderate pressure and a high-pressure test. The moderate pressure test (reservoir pressure = 586 bar) revealed only 5- to 15-percent blockage. The high-pressure test (reservoir pressure = 1,724 bar) resulted in near total blockage of the beam. Also shown on Fig. 39 is the corresponding cone model pressure gage output, C2, which indicates the time history of the flow. The flow-field contamination on high-pressure runs also affects the measurements made by the PLIF and Filtered Rayleigh Scattering systems. At high-pressure conditions, an essentially opaque flow field scatters both the incident laser energy and any resulting fluorescence, and no measurable radiation is incident at the camera of the PLIF system.

A flow probe instrumented with a total of five coaxial thermocouples was used on tests beginning with Run 20 (see Fig. 16). On Runs 20 through 25, the cone model shown in Fig. 15 was used as the test model, and the flow probe was located 22.86 cm downstream of the cone nose at a radial distance of 15.24 cm from the nozzle centerline. Data from this probe from Run 20 are shown in Fig. 40. A complete summary of data obtained from this flow probe is shown in Table 10. The averaged data were taken over a 1-msec interval which began 1 msec after the initial thermocouple gage response. The heat-transfer rates were determined using the techniques described in Section 4.5 with a moving average smoothing technique for the recorded temperature data. A study of the data in Table 10 indicates the heat-transfer rate from T7 and T9 (gages 60 deg from stagnation point) was less than that from T8 (sidewall gage) on two out of three runs where this comparison was possible. This was an unexpected result since the flow should be laminar based on the facility free-stream conditions. No conclusions concerning debris and/or particles in the flow were possible, due to the poor precision of the heat-transfer measurements.

## 5.0 CONCLUSIONS

Shakedown and calibration tests are being carried out in the new free-piston shock-heated Impulse Tunnel at AEDC. These tests have successfully demonstrated the facility's ability to produce high-velocity test gas at high density. The low-pressure calibration is considered completed. Nozzle stagnation pressures to 650 bar at enthalpies to 12.5 MJ/kg are available for test programs. The spatial and temporal test section flow uniformity was considered to be good based on pitot rake pressure measurements. For six runs, the overall average spatial pressure variation was 6.4 percent, and the temporal pressure variation was 9.2 percent during a 1-msec time period. The theoretical test times based on the facility math model ranged from 2.5 to 4.3 msec. Due to air and helium mixing at the interface, the actual test time was estimated to be in the 1.25- to 2.15-msec range.

The design criteria for high pressure diaphragms have been developed to burst pressures of 6,800 bar. Calibration experience in the laboratory and the Impulse Tunnel indicates that flat

diaphragms are satisfactory to approximately 1,400-bar burst pressure. Burst pressures above 1,400 bar require a hemispherical design. Additional development is required for hemispherical diaphragms with respect to material type and design to minimize problems with particles generated during the opening process.

A one-dimensional computer model of the Impulse Tunnel has been developed for solution of the equations of gas dynamics associated with a free-piston shock tunnel. Options are available to include the shock tube boundary-layer losses in the solution. Certain model parameters were adjusted based on the early data from T5 at Caltech and from the Impulse Tunnel. The facility model is used to help select run parameters and to produce desired flow conditions. Comparison of the model predictions to measured pressures in the facility resulted in good agreement.

A 90-percent tantalum, 10-percent tungsten alloy and an 80-percent tungsten, 20-percent copper alloy have proved to be superior throat insert materials as compared to molybdenum and molybdenum alloys for conditions run to date. A copper liner in the downrange end of the shock tube was effective in preventing erosion of the tube up to stagnation pressures of 1,000 bar. Attainment of nozzle stagnation pressures in excess of 2,000 bar will require solution to the ablation problems with the nozzle throat area and downrange end of the shock tube wall which were experienced during these tests.

## REFERENCES

1. Stalker, R. J. "The Free-Piston Shock Tube." *The Aeronautical Quarterly*, Vol. 17, November 1966, pp. 351-370.
2. Stalker, R. J. "Recent Developments with Free Piston Drivers." 17th Symposium on Shock Waves and Shock Tubes, 1989.
3. Eitelberg, G., McIntyre, T. J. Beck, W. H., and Lacey, J. "The High Enthalpy Shock Tunnel in Göttingen." AIAA Paper 92-3942, July 1992.
4. Hornung, H., et al. "Performance Data of the New Free Piston Shock Tunnel T5 at GALCIT." 18th Symposium on Shock Waves and Shock Tubes, 1991.
5. Cable, A. J. "Upgrade of the Ballistic Range Facilities at AEDC: Status as of October 1993." AIAA Paper 94-0542, January 1994.
6. Blanks, J. R. and DeWitt, J. R. "Calibration Tests of AEDC Free-Piston Shock Tunnel." AIAA Paper 94-2526, June 1994.

7. DeWitt, J. R. "Development of High-Pressure Diaphragms for the AEDC Impulse Tunnel." AEDC-TR-93-28 (AD-A277053), February 1994.
8. Piacesi, R., Gates, D. F., and Seigal, A. E. "Computer Analysis of Two-Stage Hypervelocity Model Launchers." NOL-TR 62-87, February 1963.
9. Von Neumann, J. and Richtmeyer, R. D. "A Method for the Numerical Calculation of Hydrodynamic Shocks." *Journal of Applied Physics*, Vol. 21, March 1950.
10. Richtmeyer, R. D. and Morton, K. W. *Difference Methods for Initial Value Problems*. Interscience, 1967.
11. DeWitt, J. R. and Cable, A. J. "Comparison of Experimental and Theoretical Launcher Kinematics." AEDC-TR-65-203 (AD-470966), October 1965.
12. Maus, J. R. and McKenzie, Nick R. "Modifications to the AEDC Shock Tunnel Code and Comparisons with Data." 20th International Symposium on Shock Waves, 1995.
13. Smith, M. S., Williams, W. D., Price, L. L., and Jones, J. H. "Shocktube Planar Laser Induced Fluorescence Measurements in Support of the AEDC Impulse Facility." AIAA 94-2649, June 1994.
14. Ruyten, W. M., Williams, W. D., and Heltsley, F. L. "Analysis of Planar Laser-Induced Fluorescence Images Obtained During Shakedown Testing of the AEDC Impulse Facility." AEDC-TR-94-14, March 1995.
15. Ruyten, W. M., Smith, M. S., and Williams, W. D. "On The Role of Laser Absorption in Planar Laser-Induced Fluorescence Imaging of High Enthalpy Flows." ISSW Paper No. 436, 20th International Symposium on Shock Waves, Pasadena, CA, July 1995.
16. Stepanek, S. A. "Non-Intrusive Flow Diagnostics Applied in High-Enthalpy Facilities." 16th International Congress on Instrumentation in Aerospace Simulation Facilities, Dayton, OH, July 1995.
17. Wittliff, C. E., Wilson, M. R., and Hertzberg, A. "The Tailored-Interface Hypersonic Shock Tunnel." *Journal of the Aerospace Sciences*, Vol. 26, April 1958.
18. Brahinsky, Herbert S. and Neel, Charles A. "Tables of Equilibrium Thermodynamic Properties of Air." AEDC-TR-69-89, April 1969.

19. Cook, W. J. and Felderman, E. J. "Reduction of Data from Thin-Film Heat-Transfer Gages: A Concise Numerical Technique." *AIAA Journal*, Vol. 4, No. 3, March 1966.
20. Kidd, C. T. "Coaxial Surface Thermocouples: Analytical and Experimental Considerations for Aerothermal Heat-Flux Measurement Applications." ISA Paper No. 90-126, 1990.
21. Matthews, R. K., Nutt, K. W., Wannenwetsch, G. D., and Kidd, C. T. "Developments in Aerothermal Test Techniques at the AEDC Supersonic-Hypersonic Wind Tunnels." AIAA Paper 85-1003.
22. Maus, J. R. and Rock, S. G. "Computational Results for AEDC Free-Piston Shock Tunnel and Comparison with Calibration Data." AIAA Paper 95-6039, April 1995.
23. Molvik, G. A. and Merkle, C. L. "A Set of Strongly Coupled, Upwind Algorithms for Computing Flows in Chemical Nonequilibrium." AIAA-89-0199, January 1989.
24. Rock, S. G. and Tramel, R. W. "A Three-Dimensional Thermo-Chemical Nonequilibrium Chimera Flow Solver for Moving Grids, Part 1: Steady State." AIAA Paper 95-0151, January 1995.
25. Curtis, J. T. and Tramel, R. W. "NEQPAK, the AEDC Thermochemical Nonequilibrium Package - Theory and Use." AEDC-TR-93-20, March 1994.

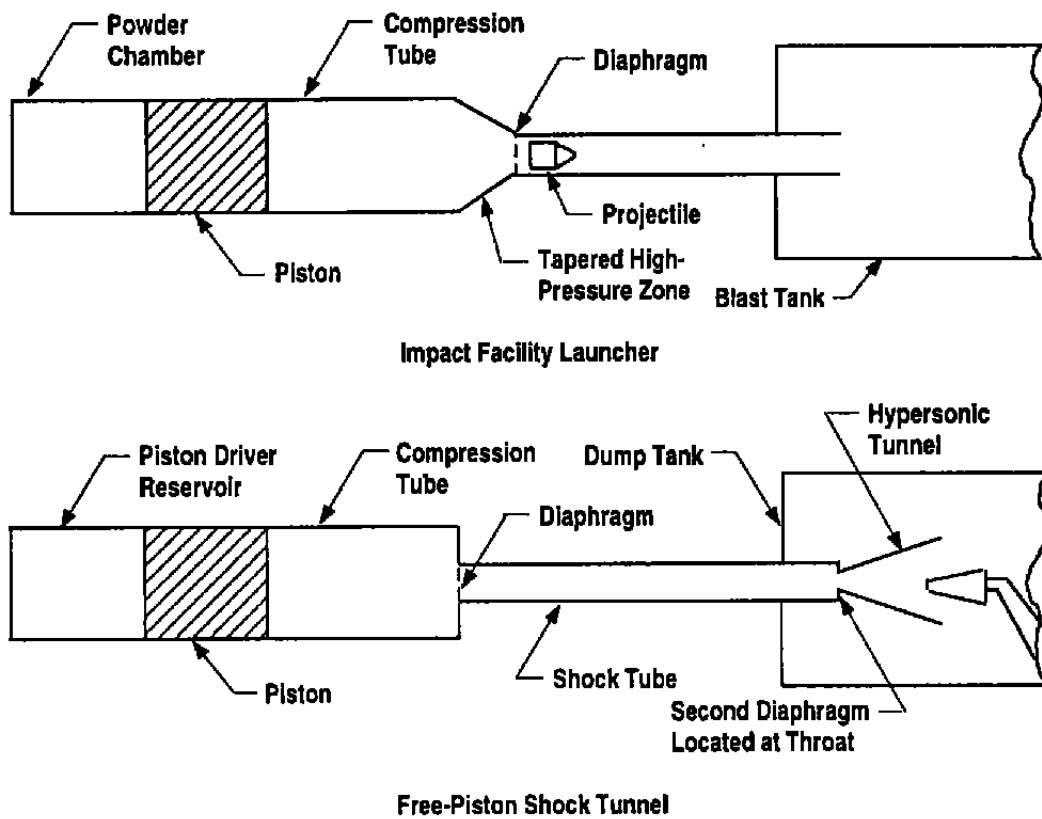


Figure 1. Light-gas gun and shock tunnel components.

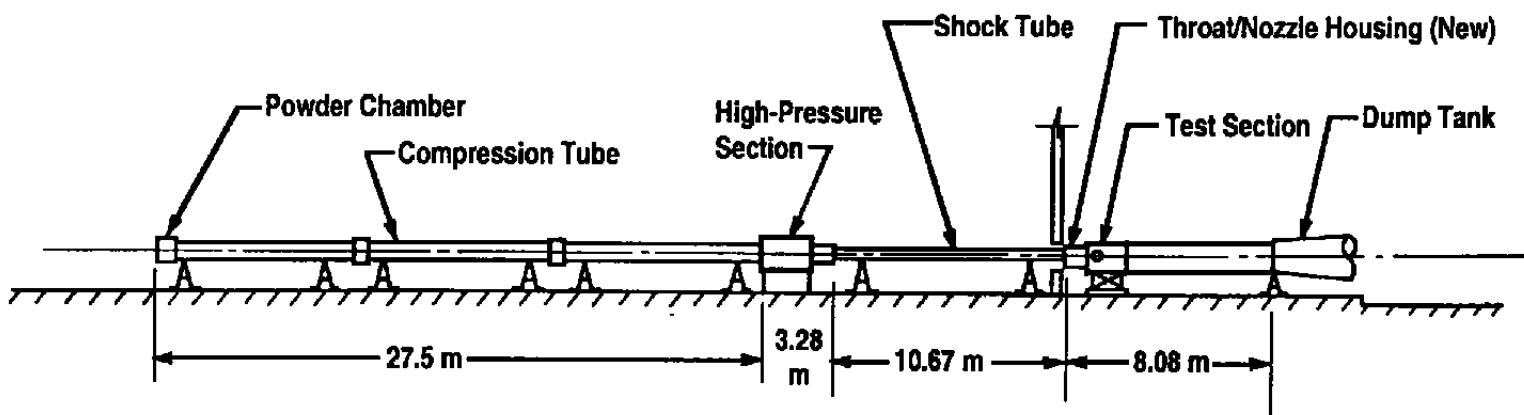


Figure 2. Impulse tunnel layout.

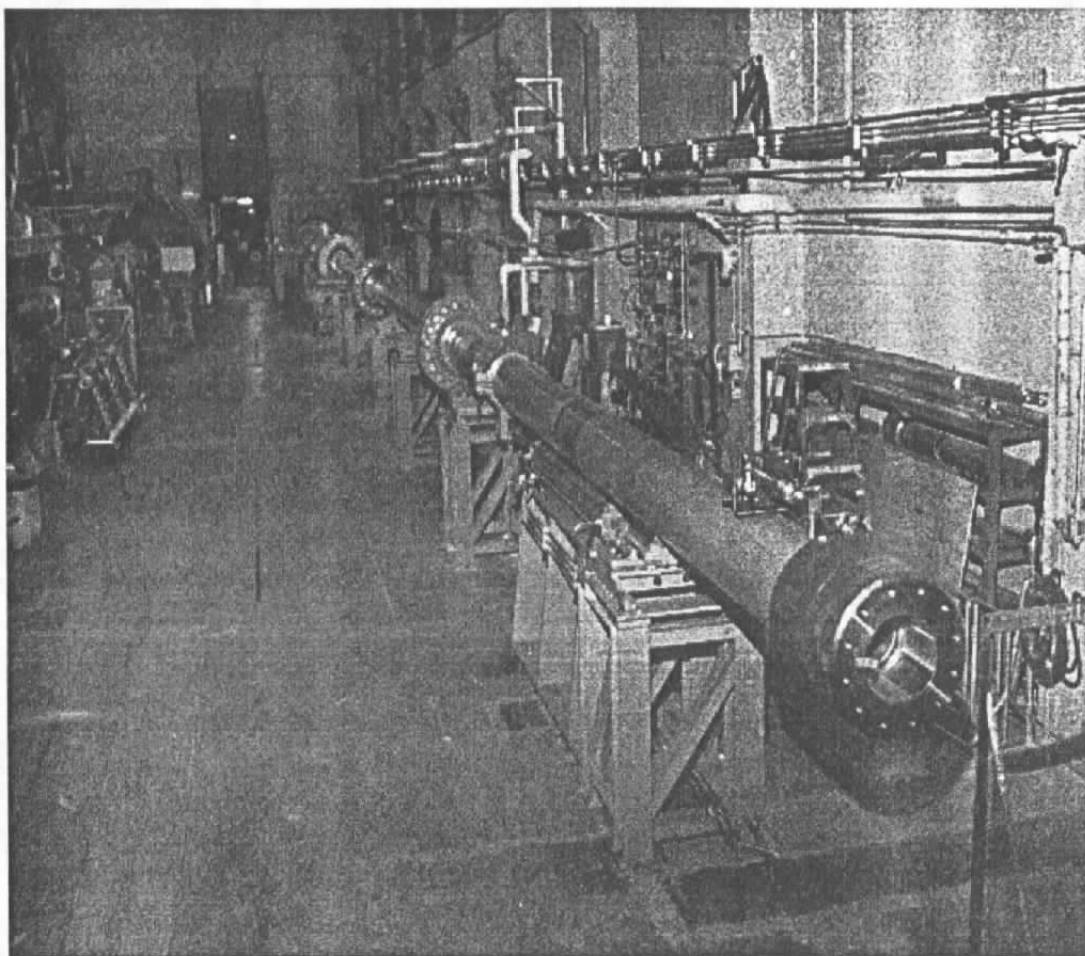


Figure 3. Downrange view of powder chamber and compression tube.

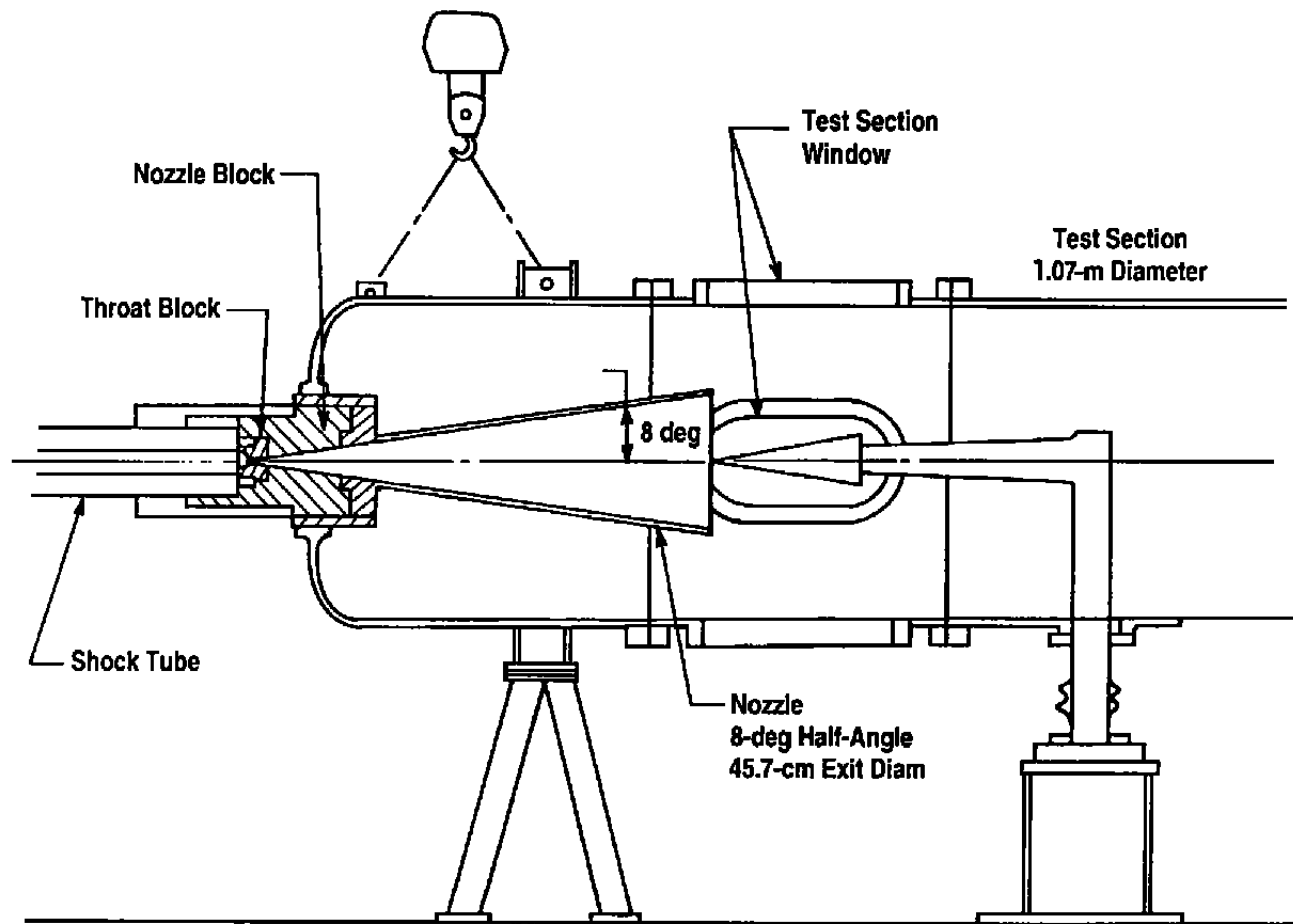


Figure 4. Nozzle/test section detail.

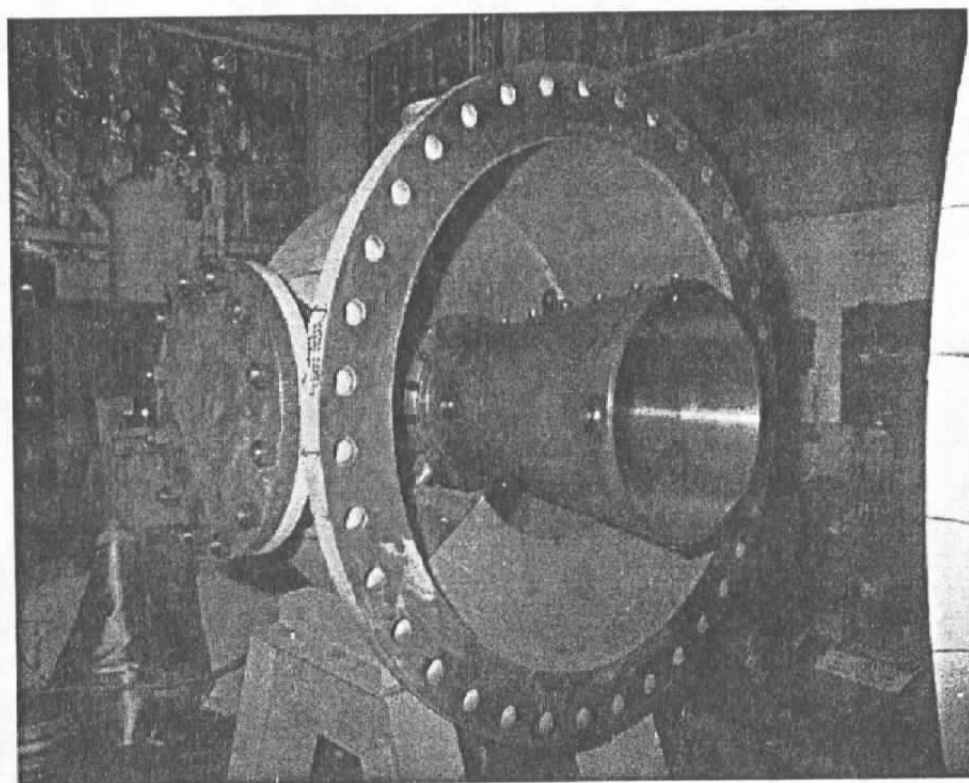


Figure 5. The Impulse Tunnel showing nozzle exit.

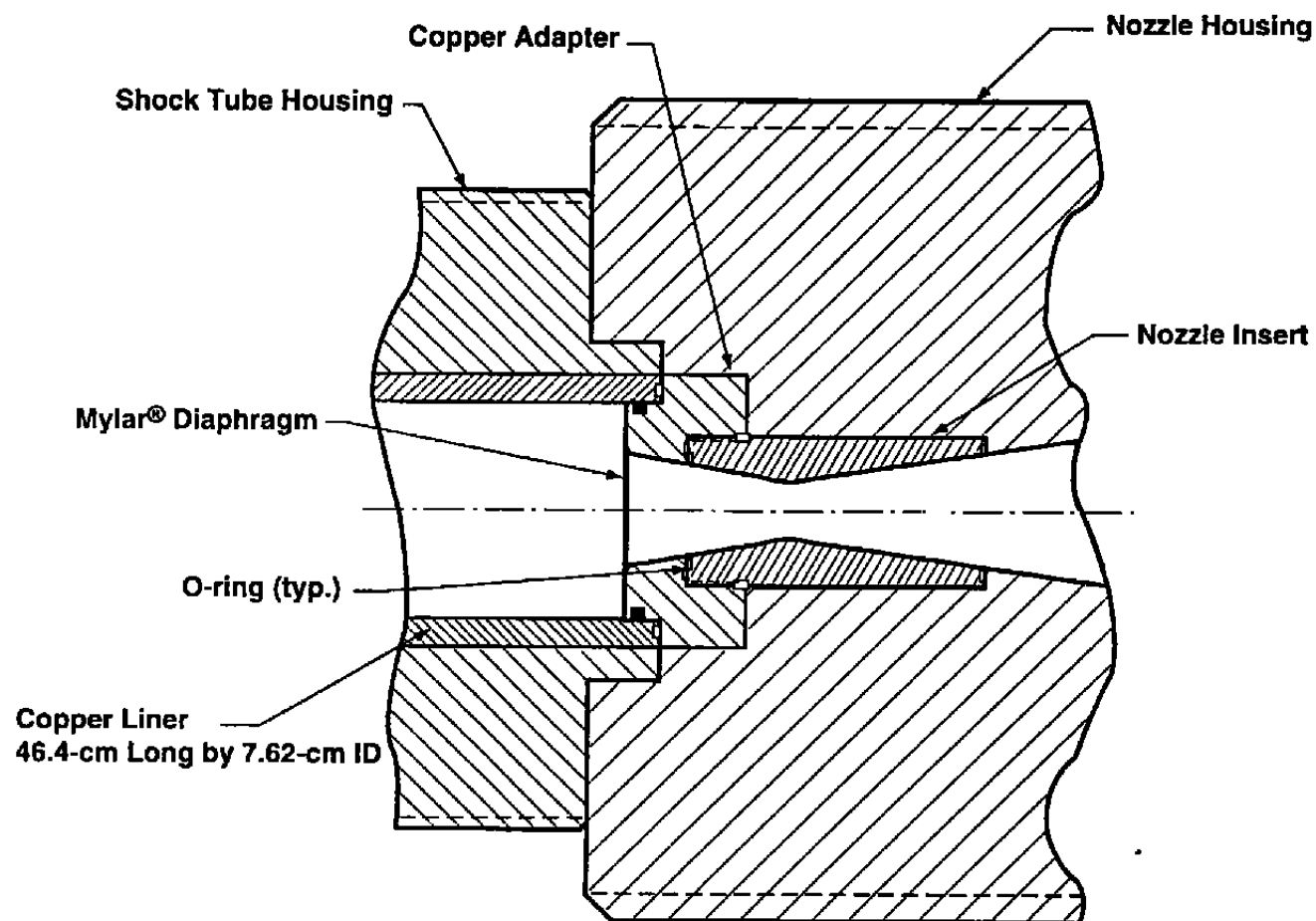


Figure 6. Nozzle insert installation/configuration.

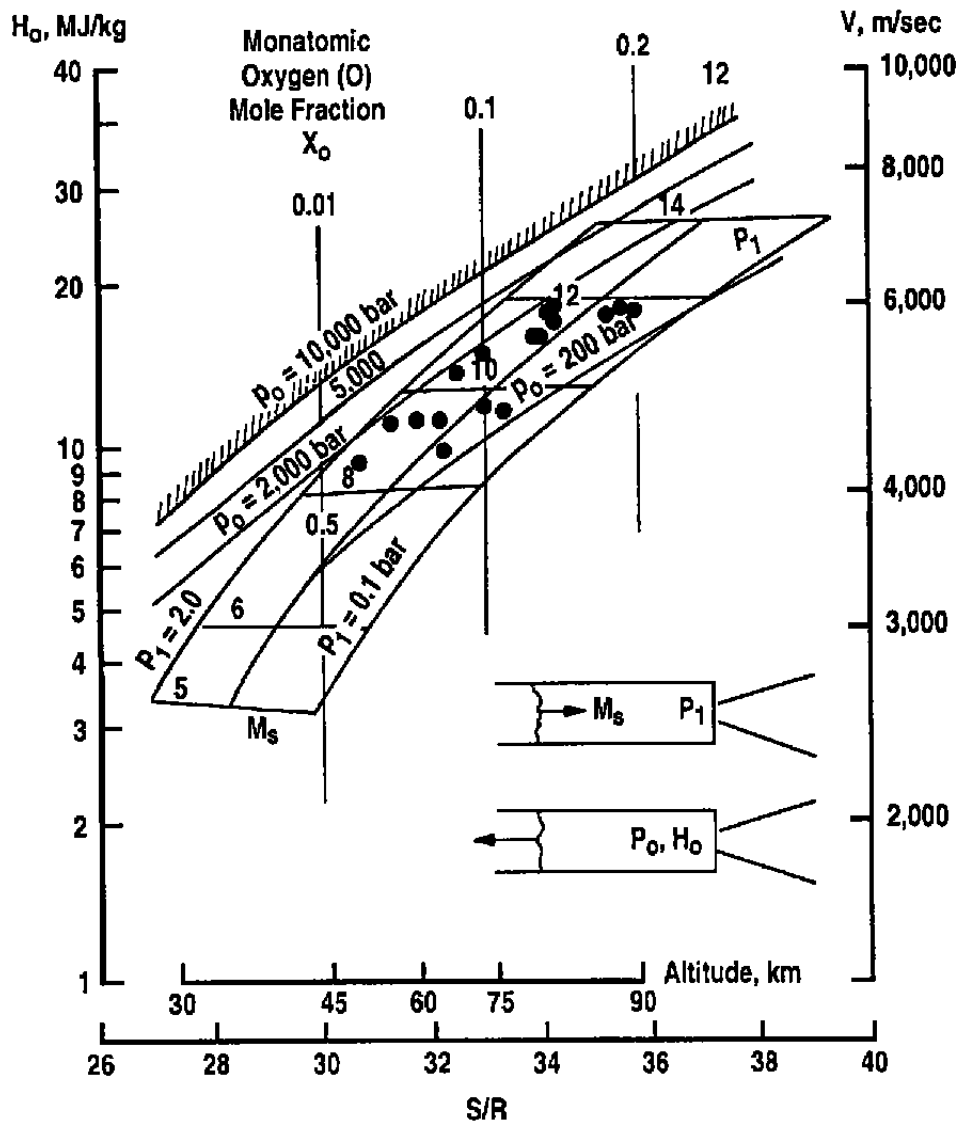
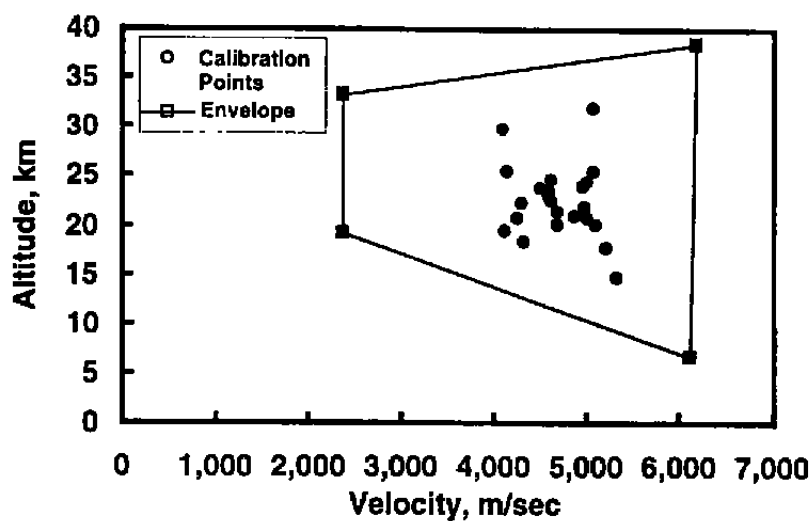
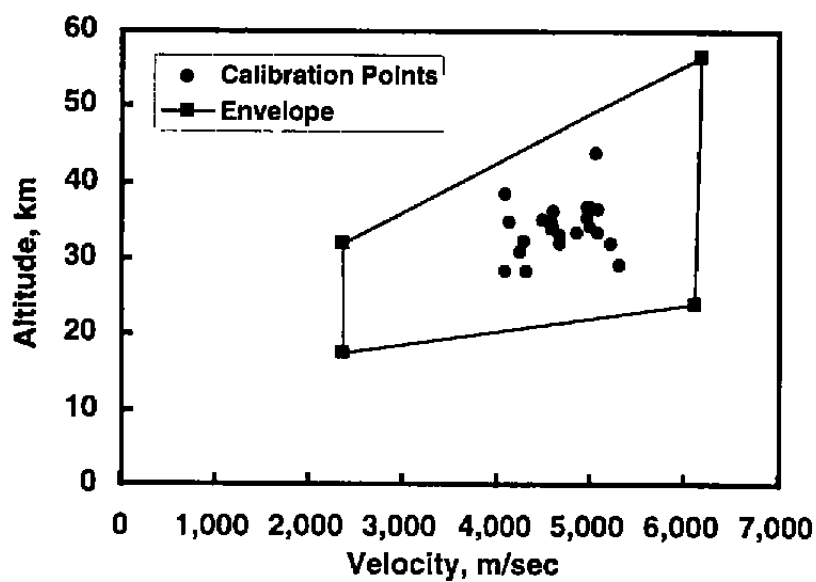


Figure 7. Projected operating envelope – Molier Diagram.



a. Altitude based on pressure at nozzle exit



b. Altitude based on density at nozzle exit

Figure 8. Projected operating envelope – altitude/velocity.

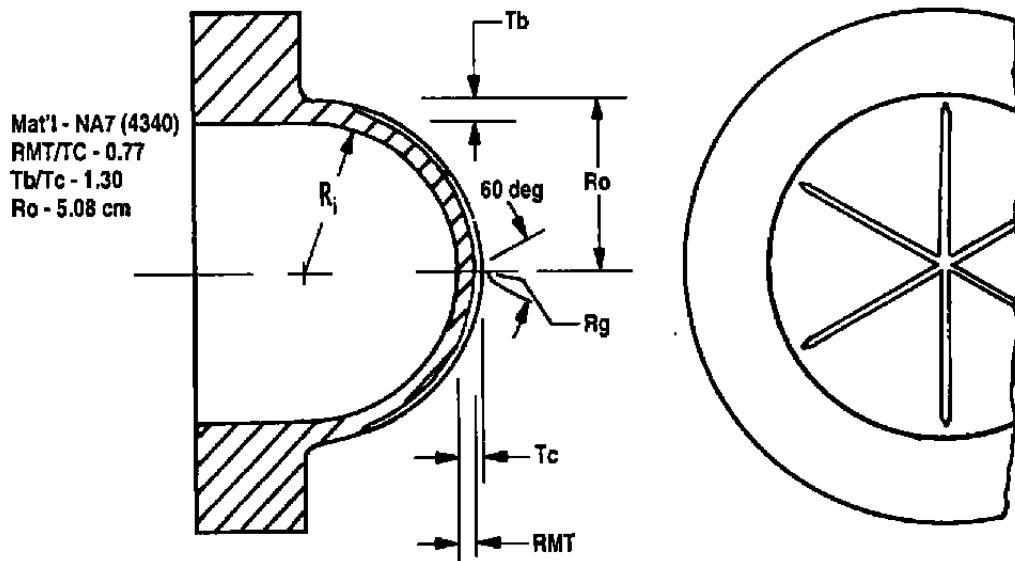


Figure 9. Shaped diaphragm dimensions.

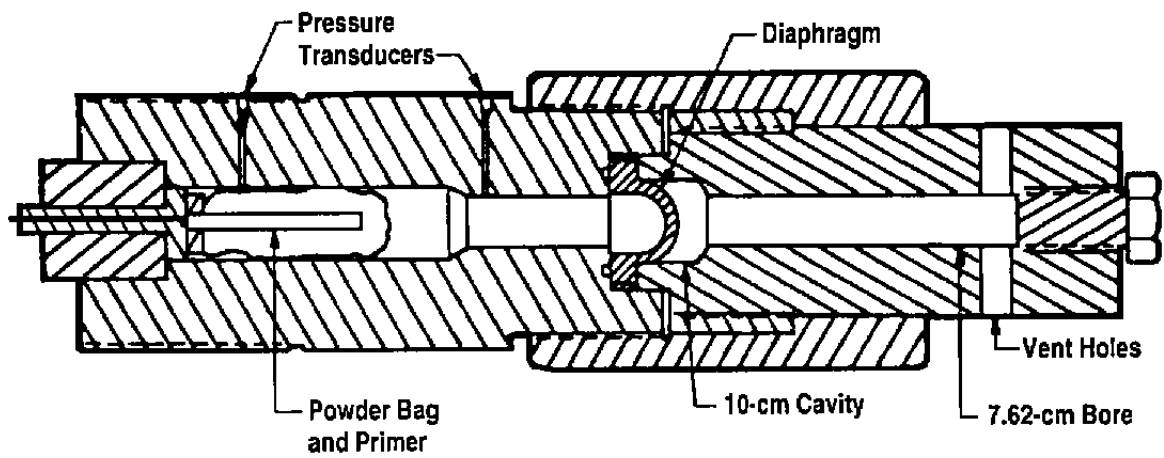


Figure 10. Diaphragm test rig.

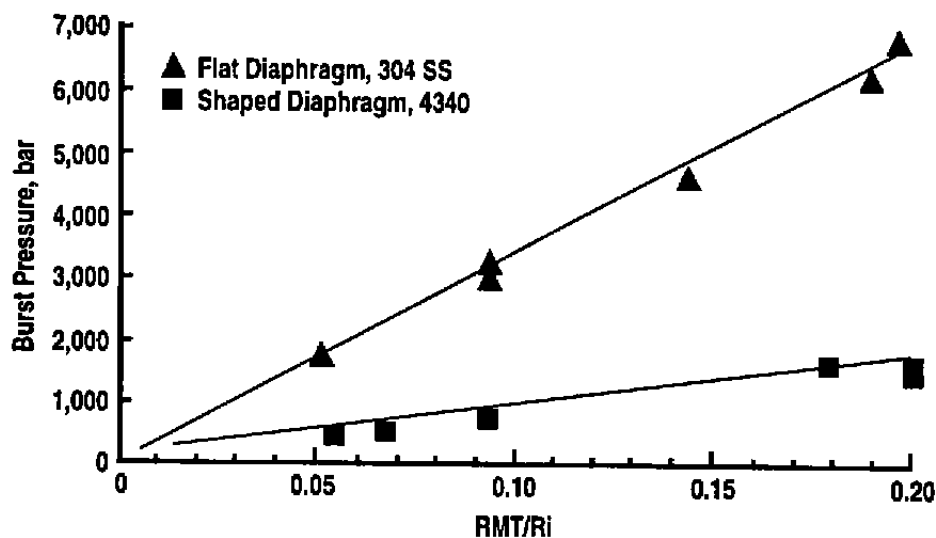


Figure 11. Diaphragm burst pressure results.

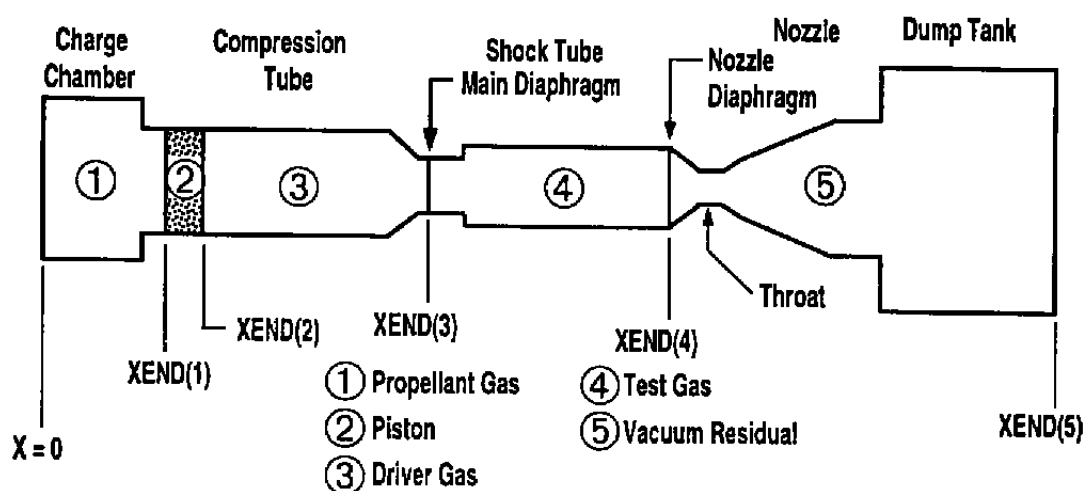


Figure 12. Facility components and initial region boundaries.

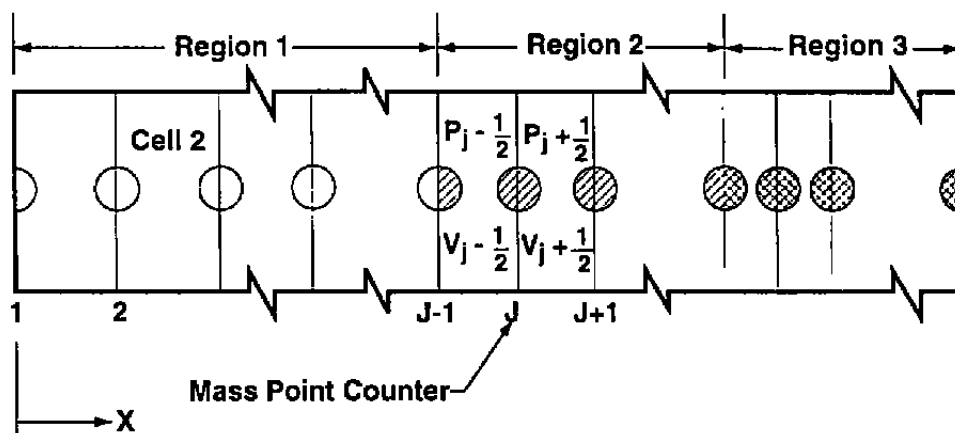


Figure 13. Mass points, cells, and regions.

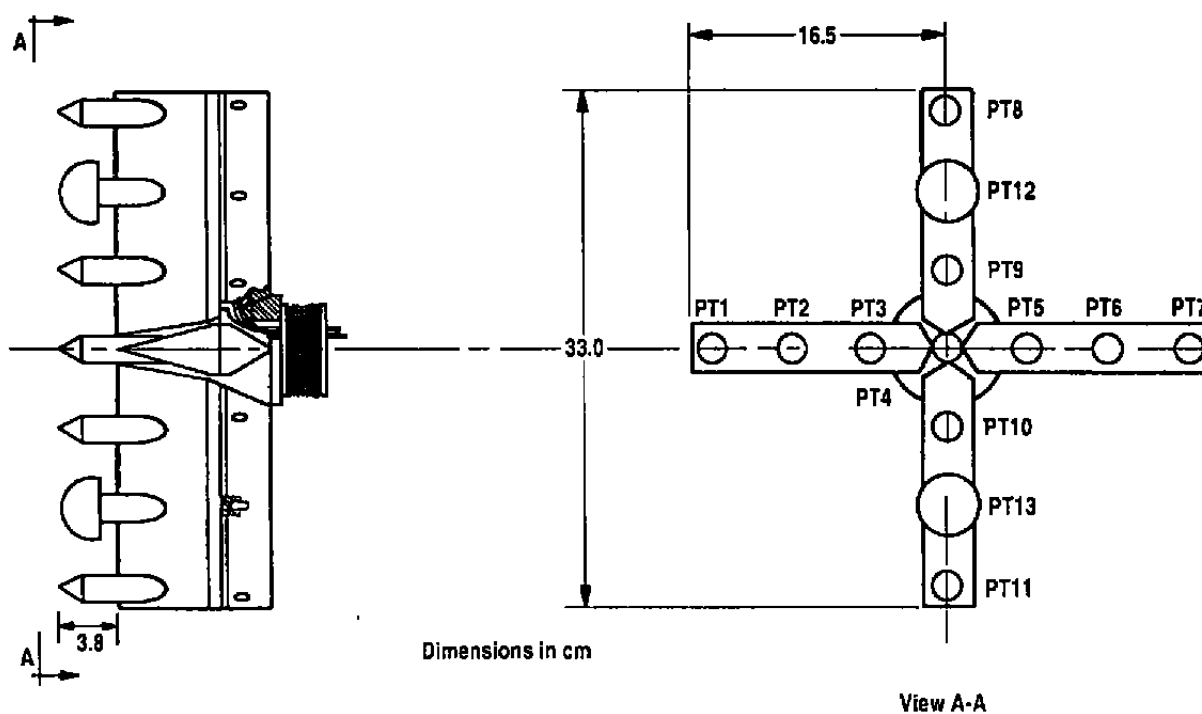


Figure 14. Pitot rake configuration.

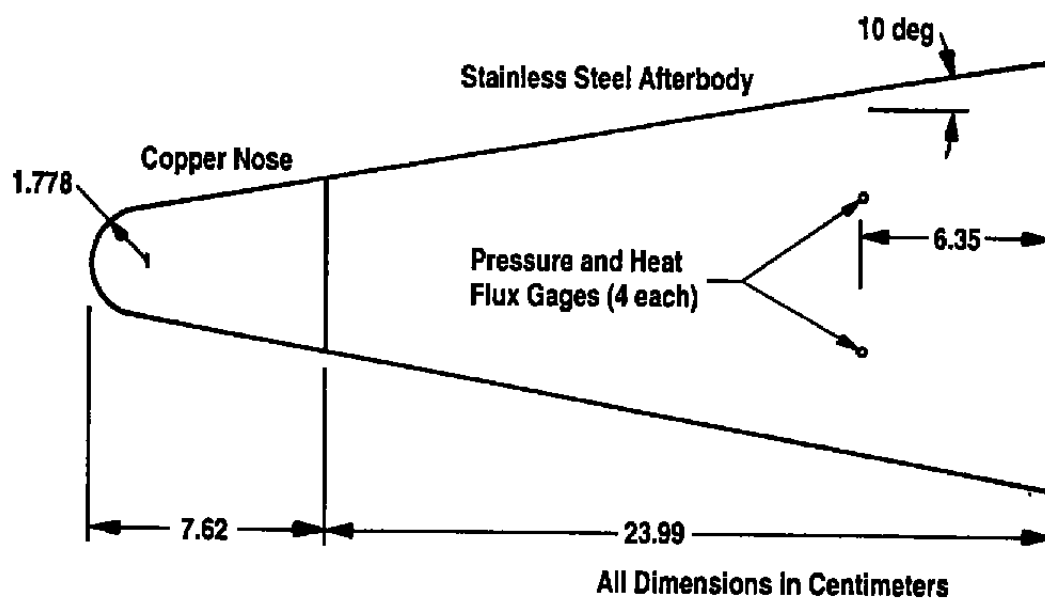


Figure 15. Calibration model dimensions.

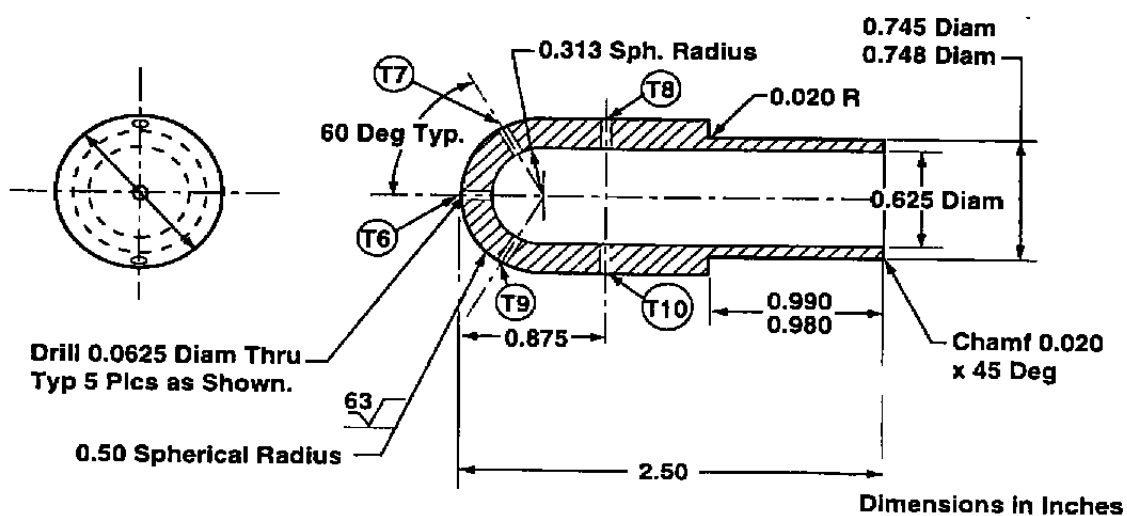


Figure 16. Impulse Facility flow probe.

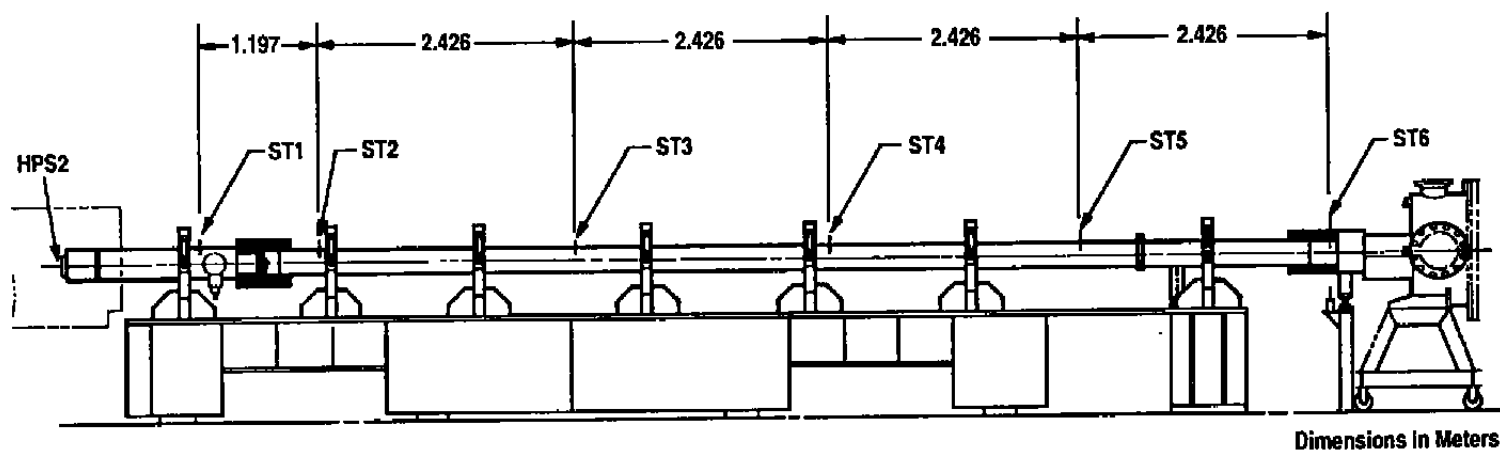


Figure 17. Location and designation of shock tube pressure transducers.

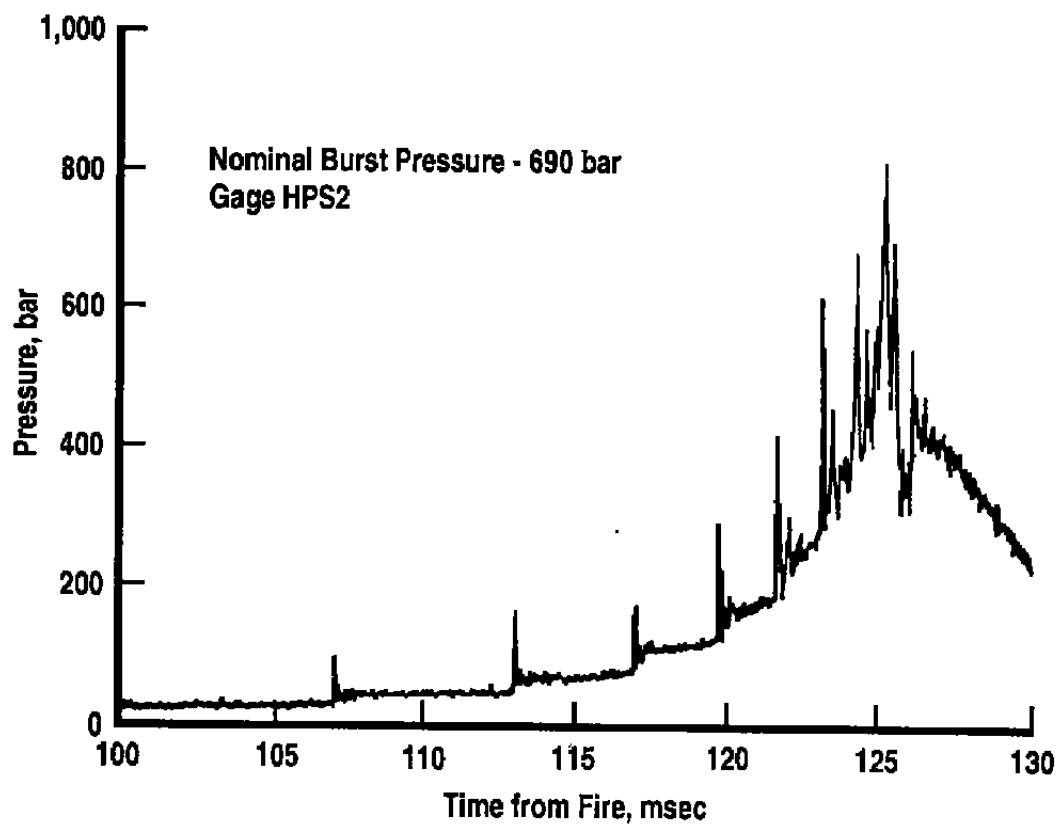
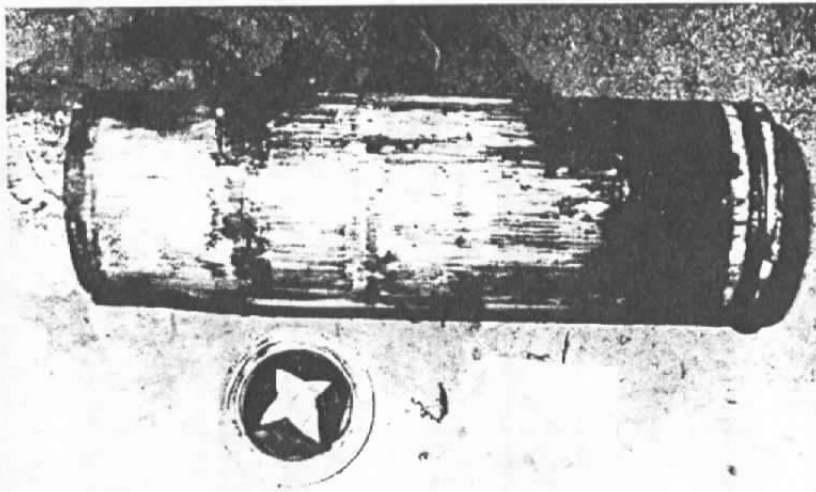
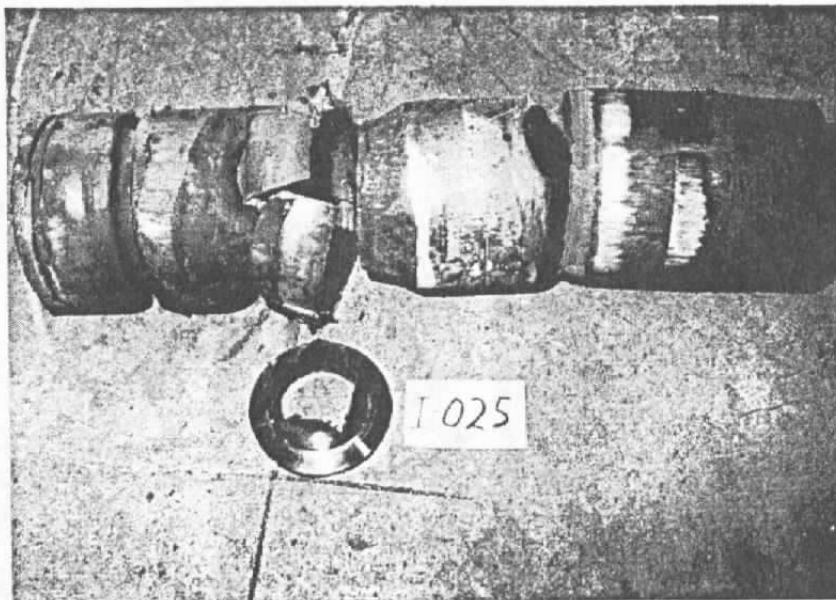


Figure 18. High-pressure section pressure, Run 7.



a. Run 23



b. Run 25

Figure 19. Posttest pistons and HPS diaphragms.

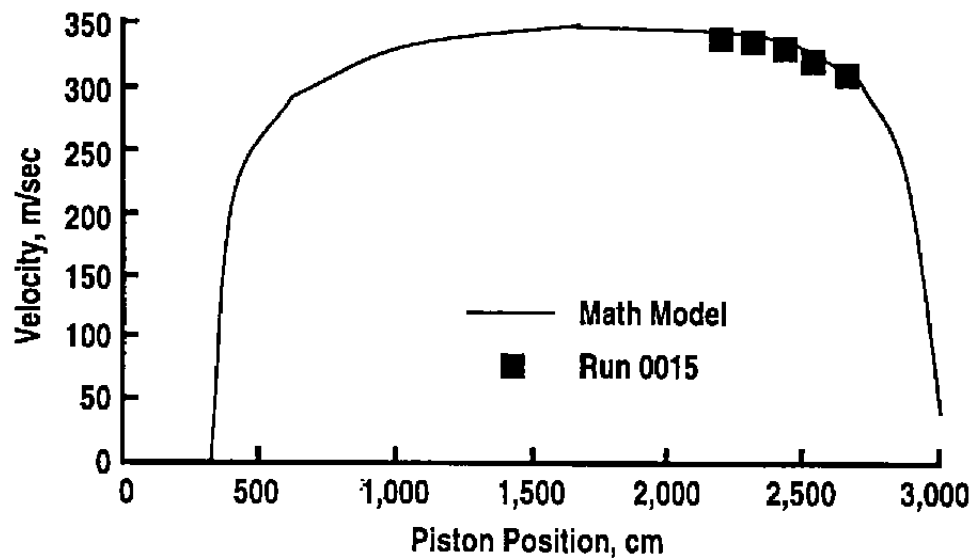


Figure 20. Piston velocity comparison to math model, Run 15.

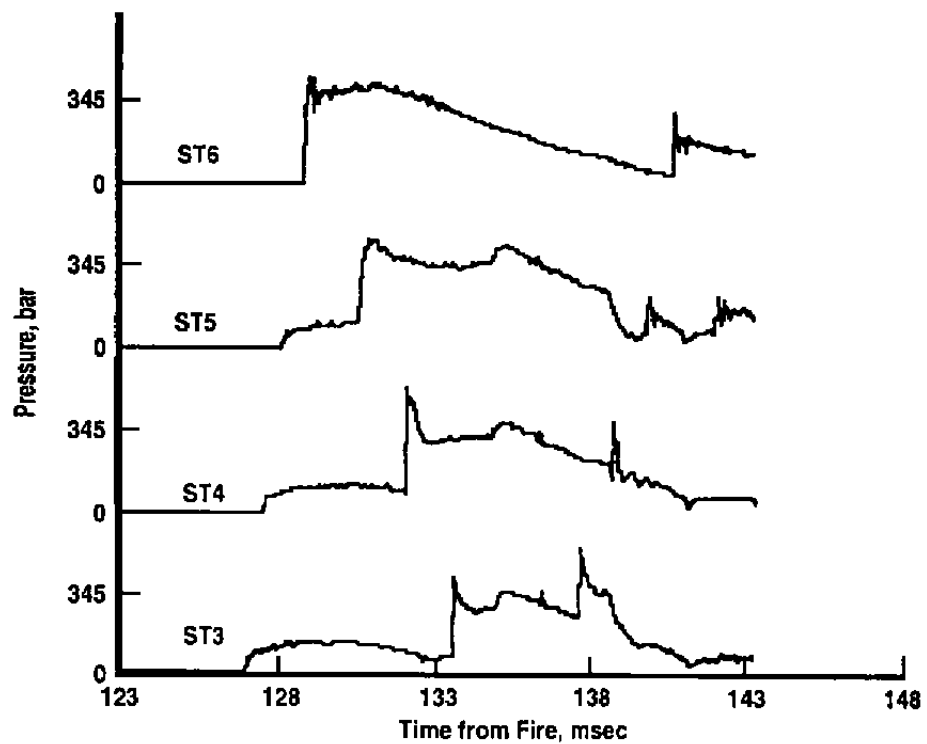
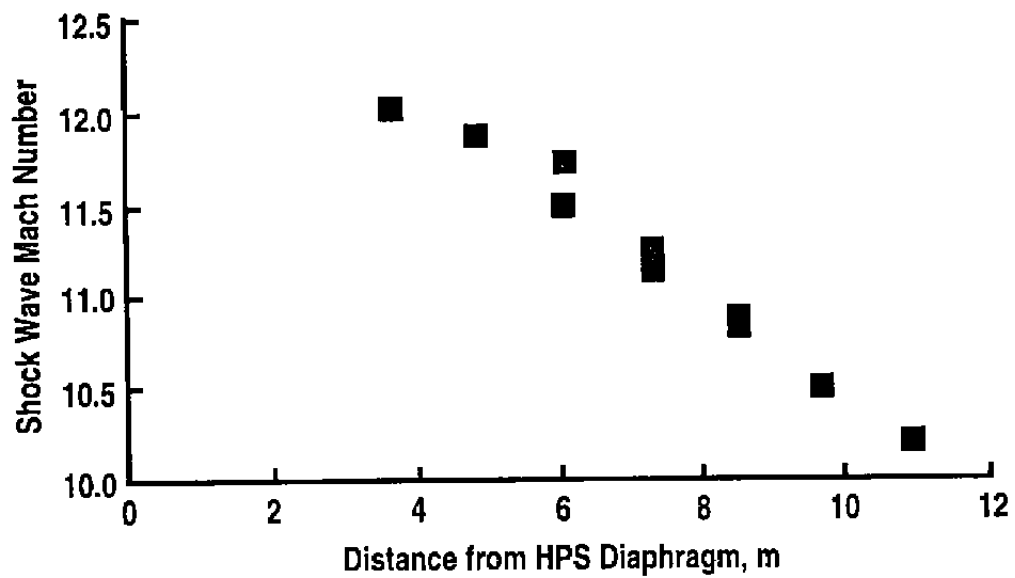
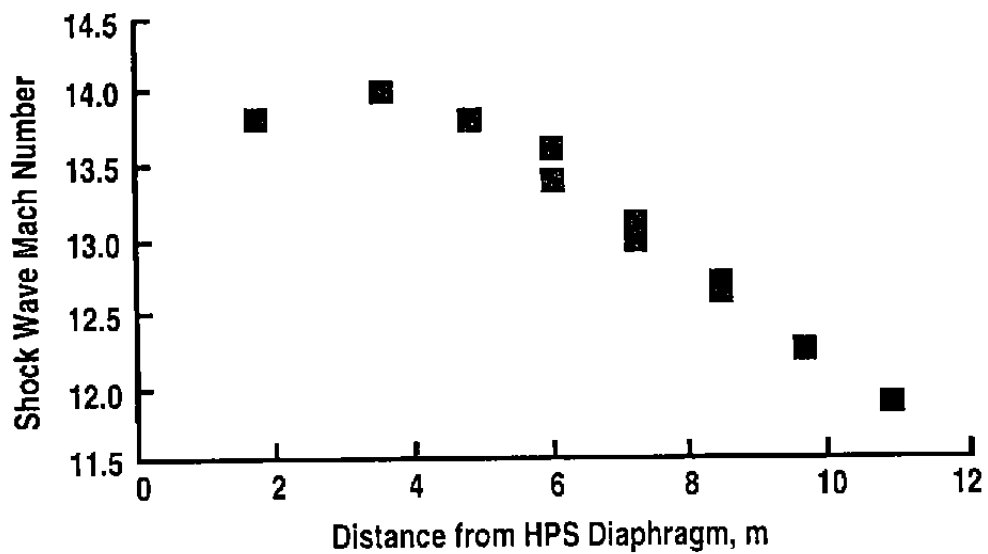


Figure 21. Shock tube pressure traces, Run 7.

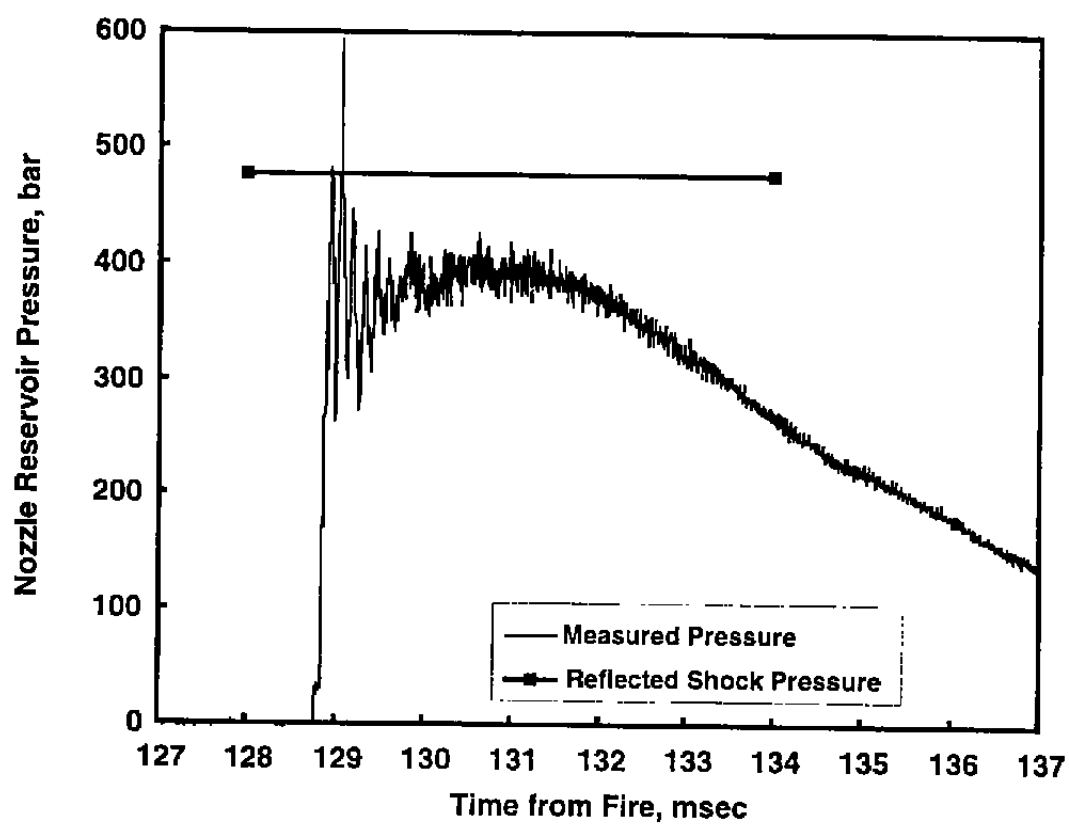


a. Run 7



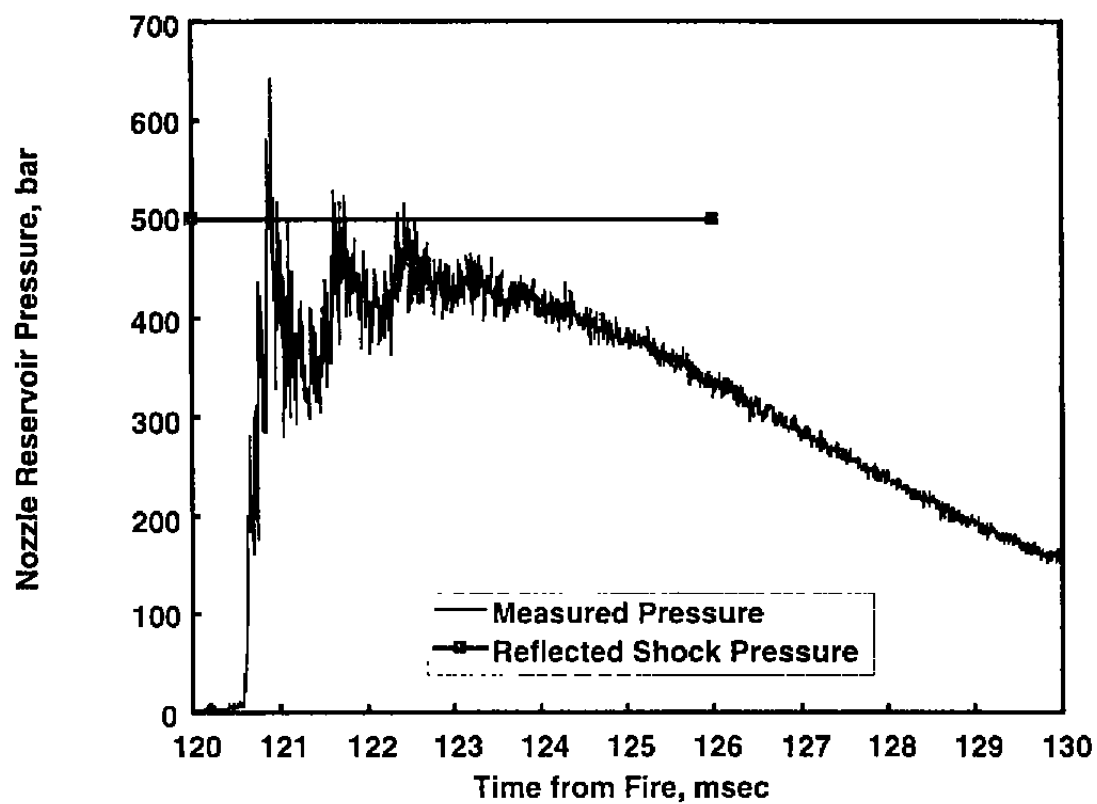
b. Run 17

Figure 22. Shock wave Mach number history.



a. Run 7

Figure 23. Comparison of measured to shock-reflected reservoir pressure.



b. Run 20  
Figure 23. Concluded.

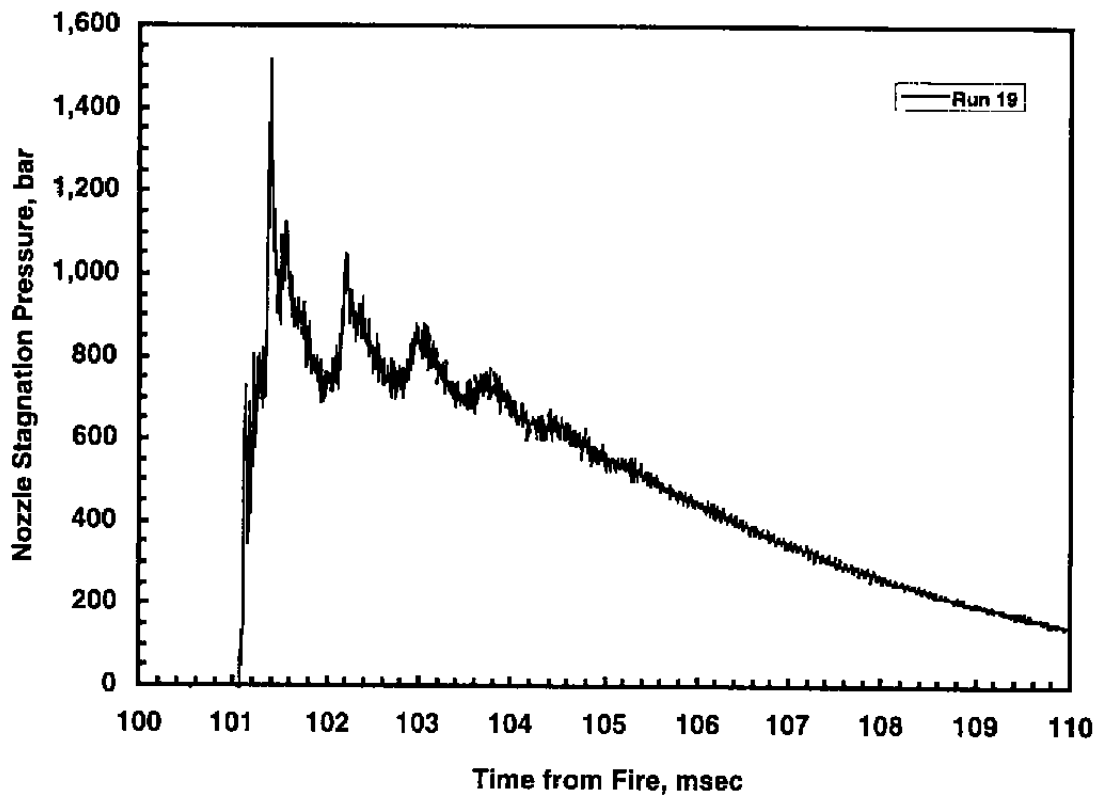
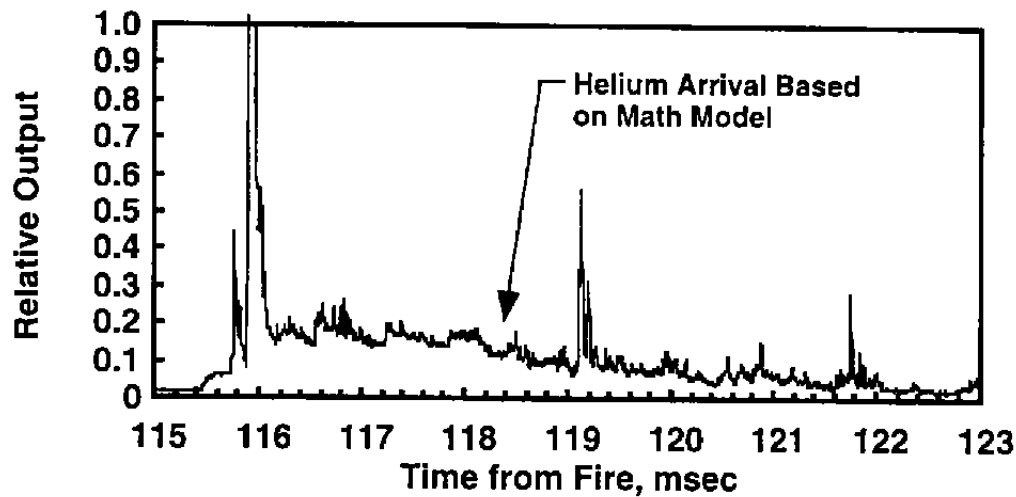
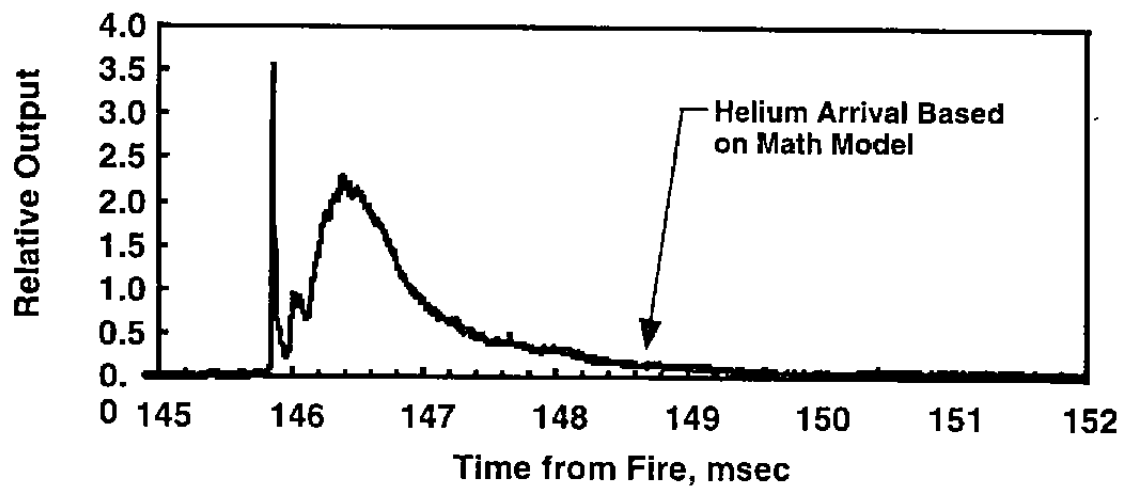


Figure 24. Example of non-tailored run



a. Run 2



b. Run 5

Figure 25. Visible band radiometer helium detector.

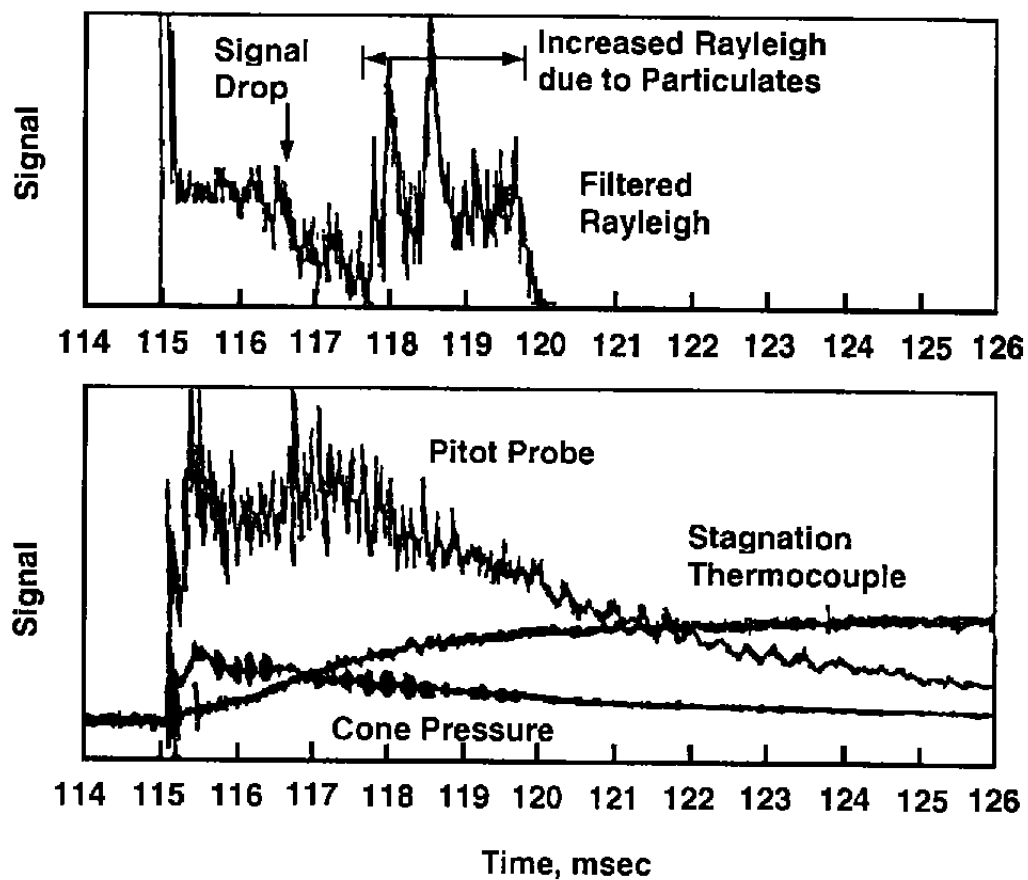
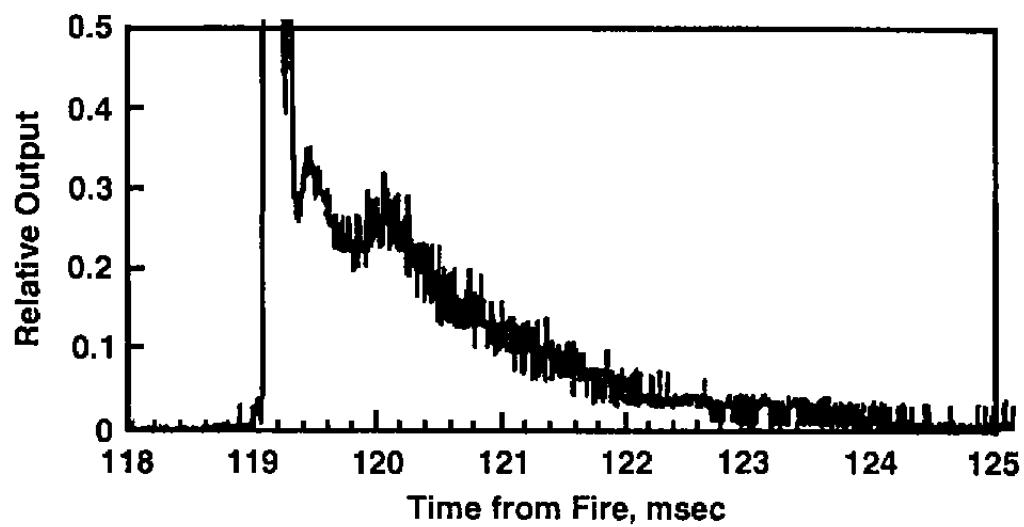
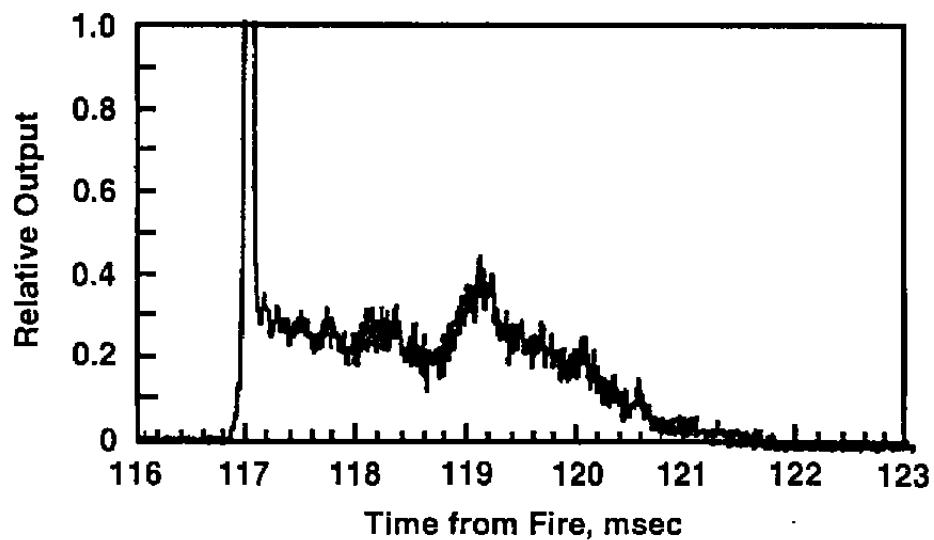


Figure 26. Effect of particulates on Rayleigh scattering helium detector, Run 23.

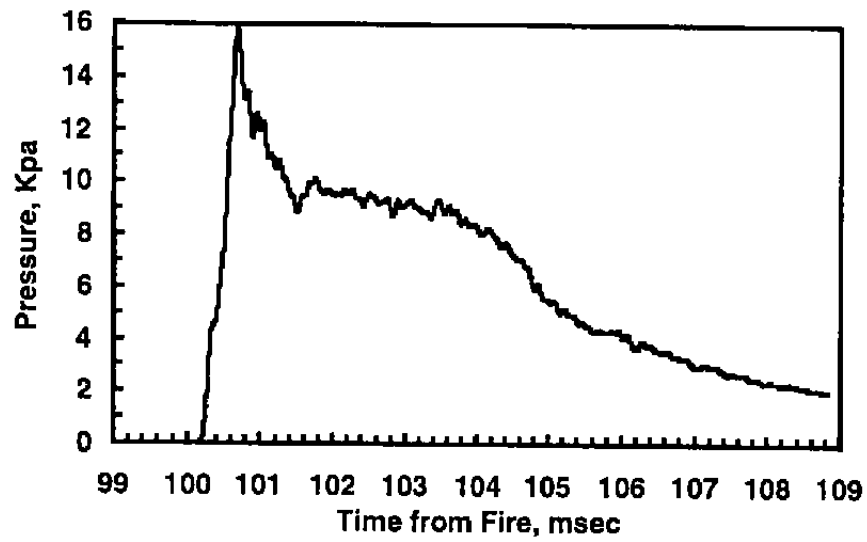


a. Run 20

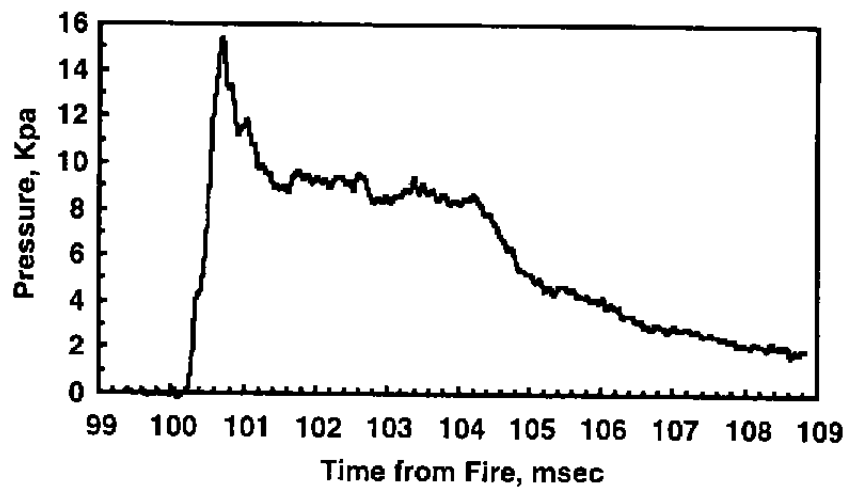


b. Run 21

Figure 27. Rayleigh scattering helium detector.

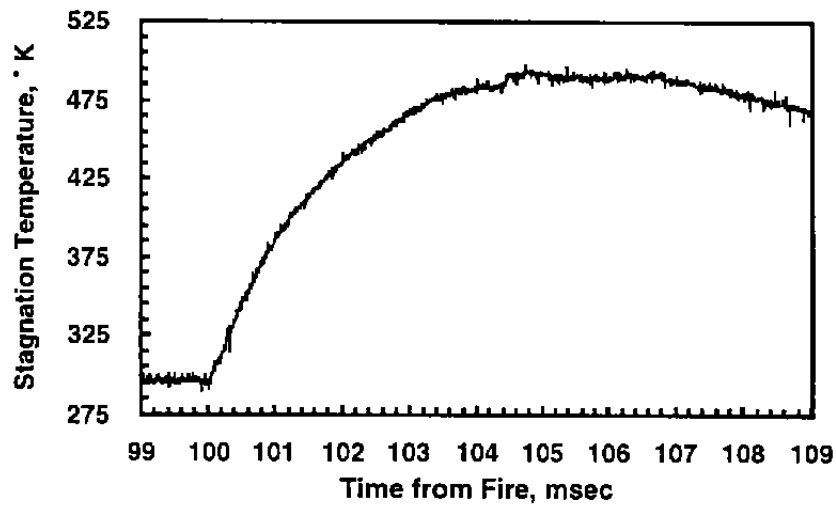


a. Run 13, Gage C1

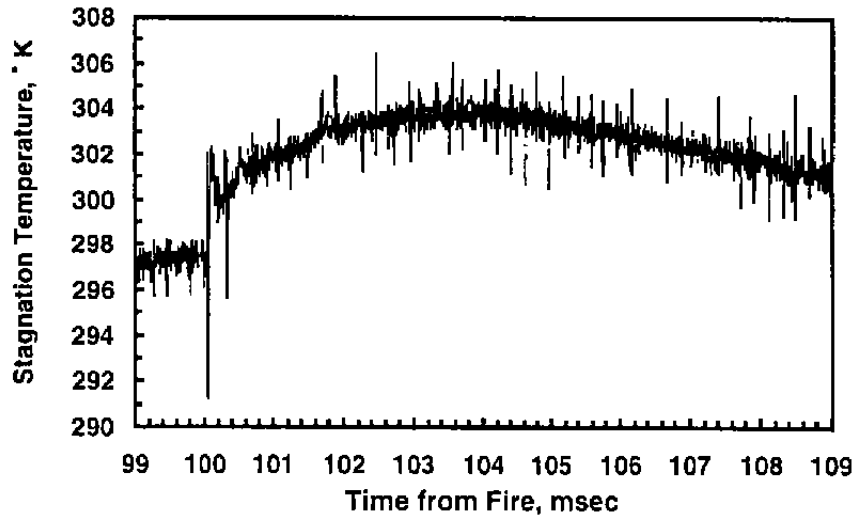


b. Run 13, Gage C3

Figure 28. Calibration cone sidewall pressures.

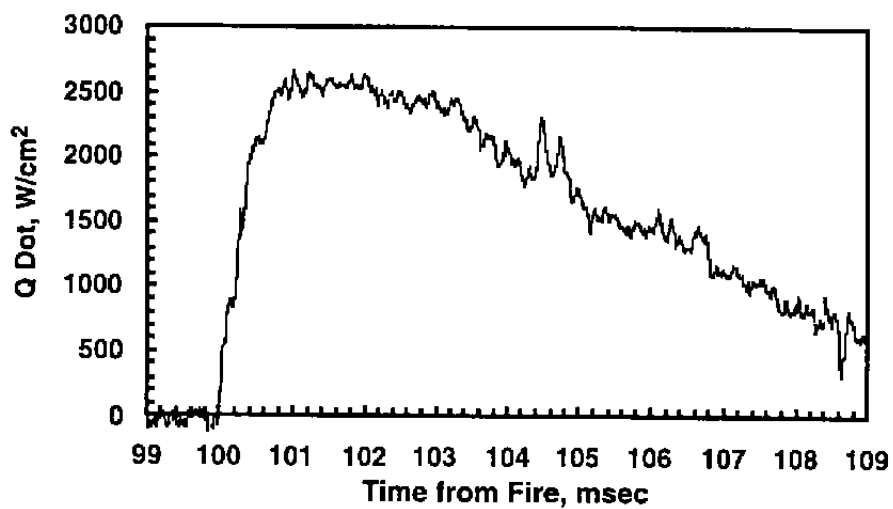


a. Stagnation Gage T5, Run 13

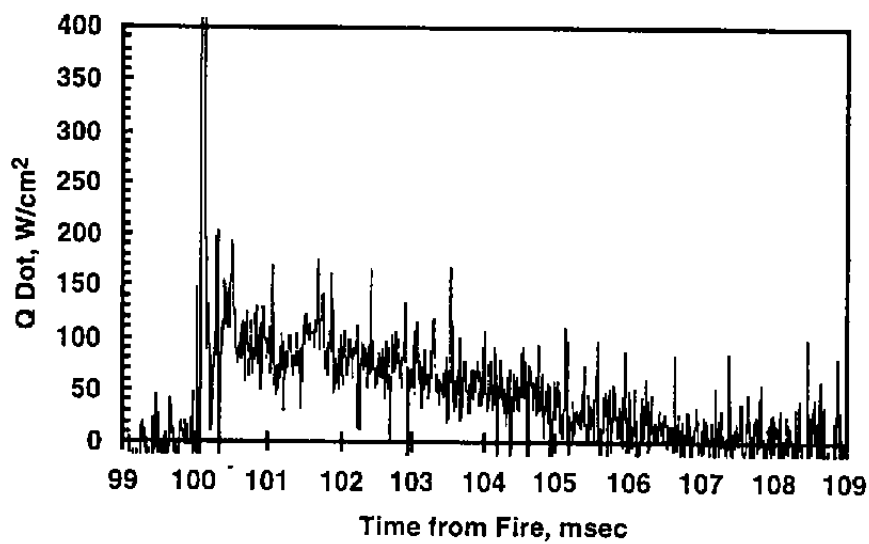


b. Sidewall Gage T1, Run 13

Figure 29. Calibration cone surface temperatures.

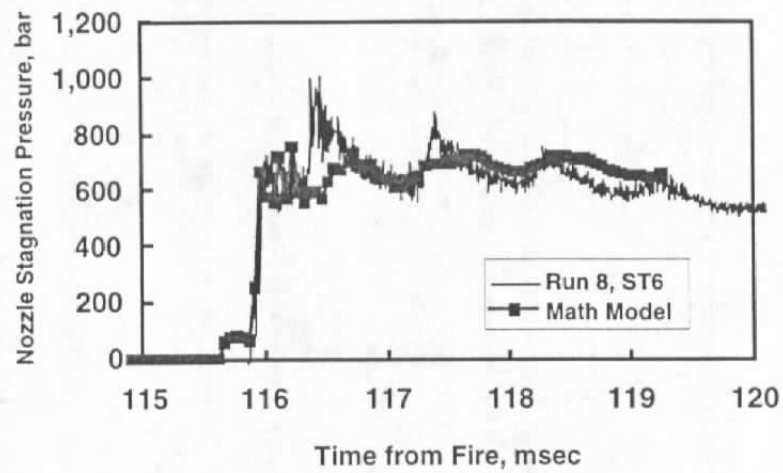


a. Stagnation Gage T5, Run 13

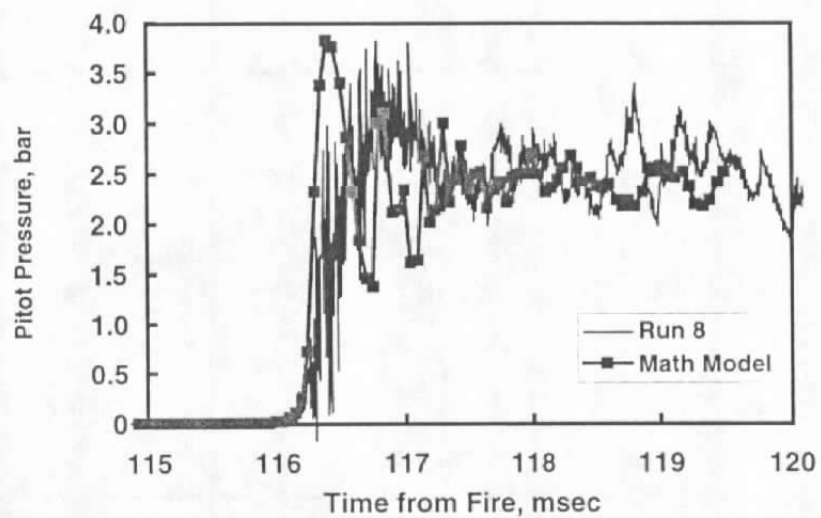


b. Sidewall Gage T1, Run 13

Figure 30. Calibration cone heat-transfer rates.

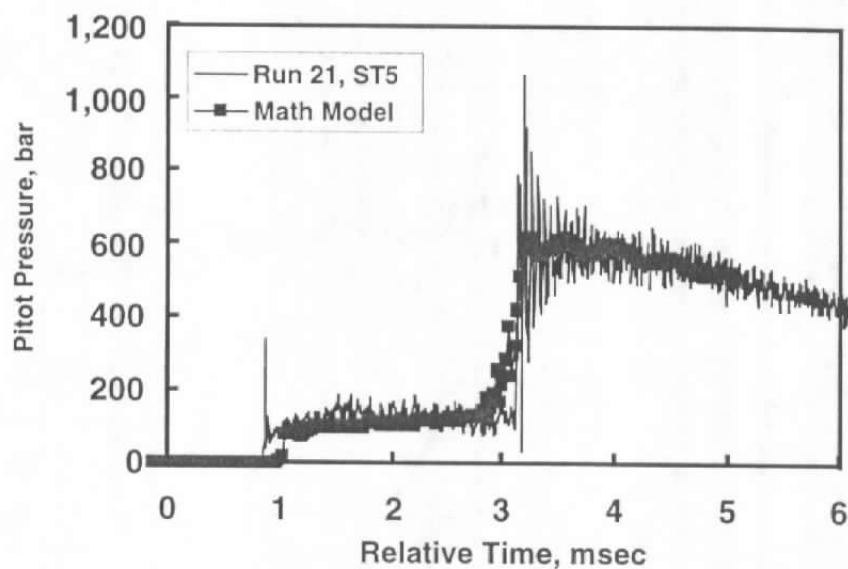


a. Run 8, Pressure Gage ST6

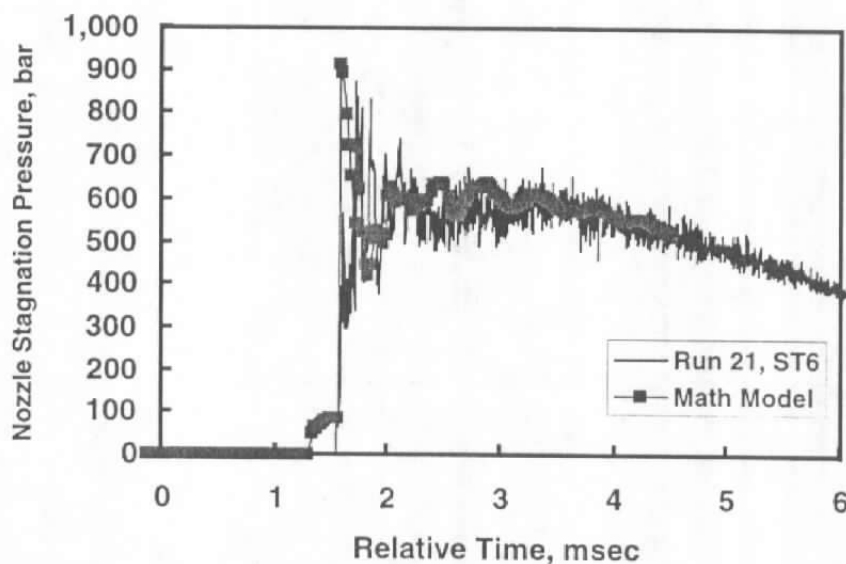


b. Run 8, Pressure Gage PT4

Figure 31. Math model comparison with calibration data.

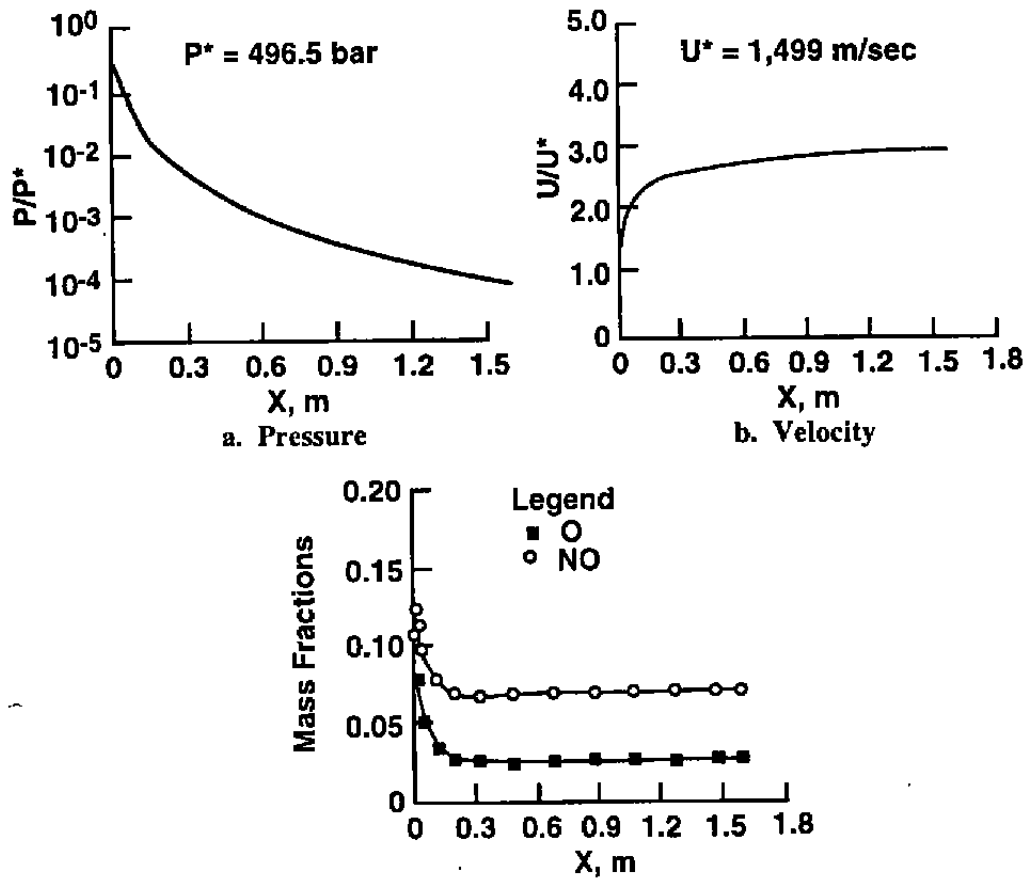


c. Run 21, Pressure Gage ST5



d. Run 21, Pressure Gage ST6

Figure 31. Concluded.



c. Species mass fraction  
 Figure 32. One-dimensional nozzle computation, Run 13.

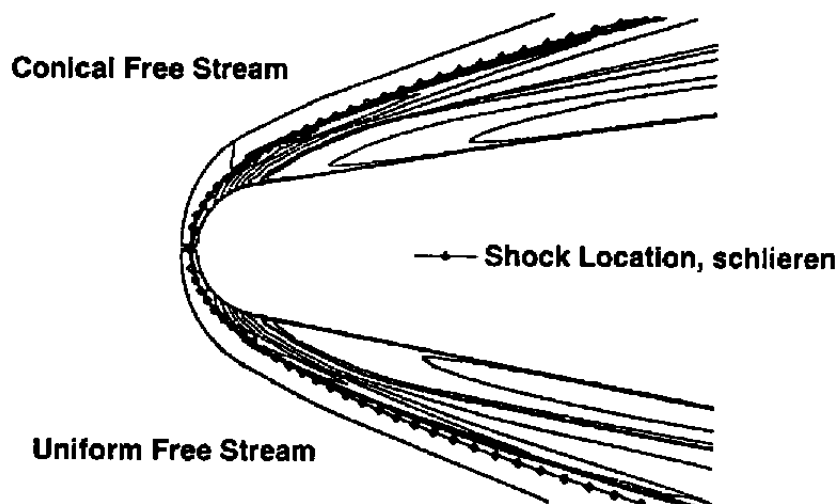


Figure 33. Computed density field and measured shock shape, Run 16.

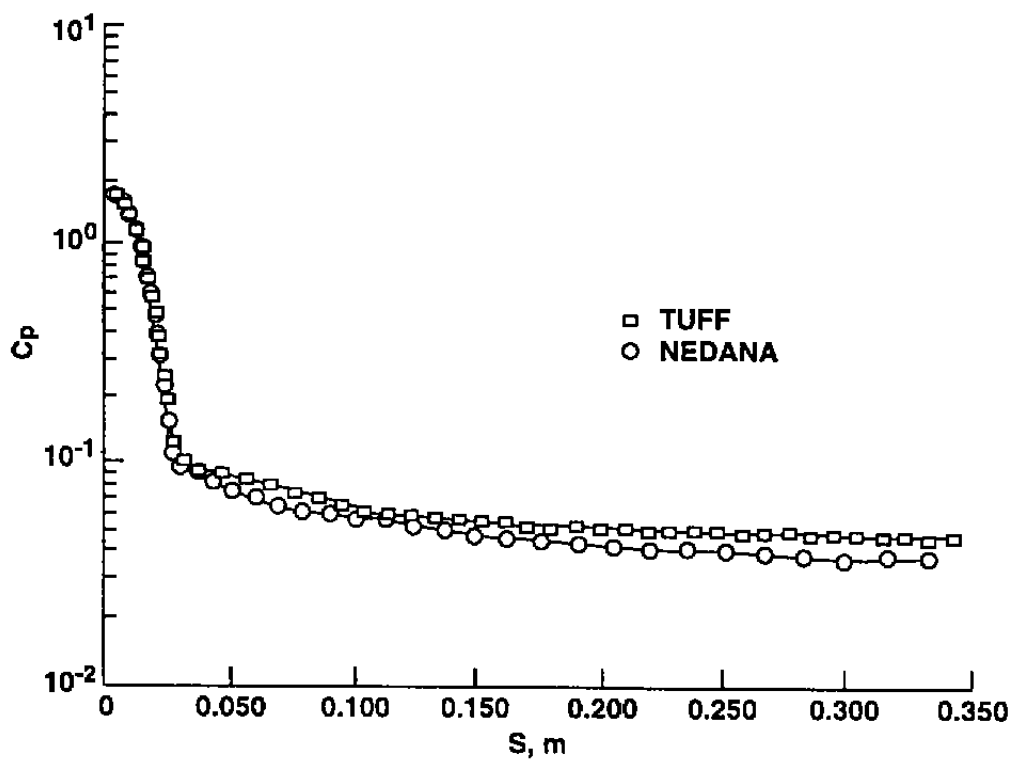


Figure 34. Computed pressure distribution on test article, Run 13.

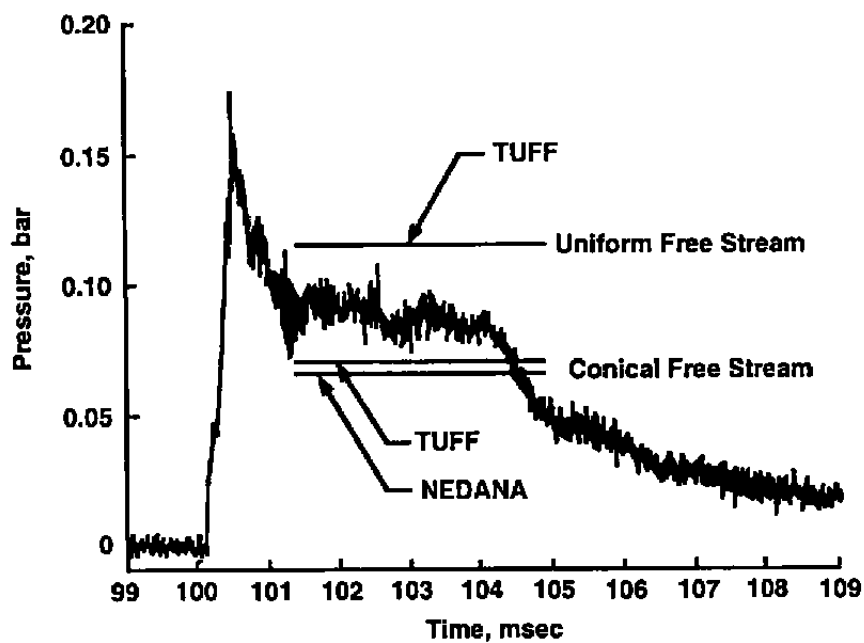


Figure 35. Comparison of computed pressures at  $X = 0.2526$  m with data.

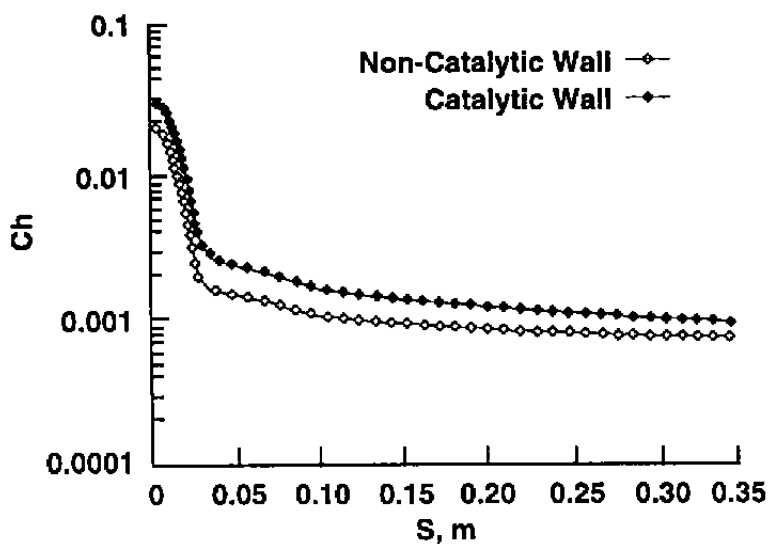


Figure 36. Computed heat-transfer distribution, Run 13.

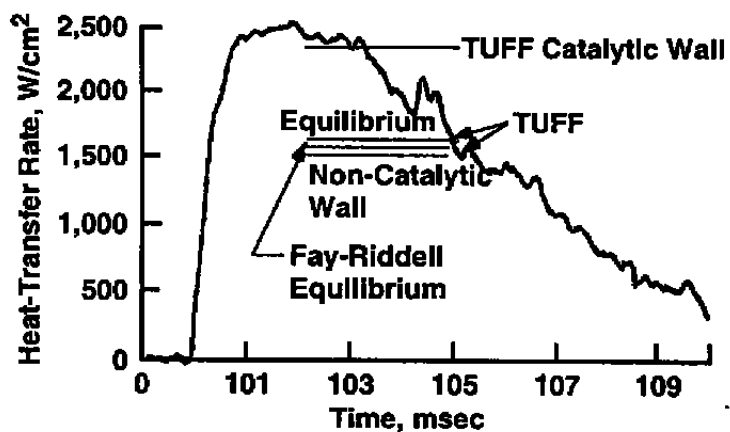


Figure 37. Comparison of computed stagnation point heat transfer with measurements, Run 13.

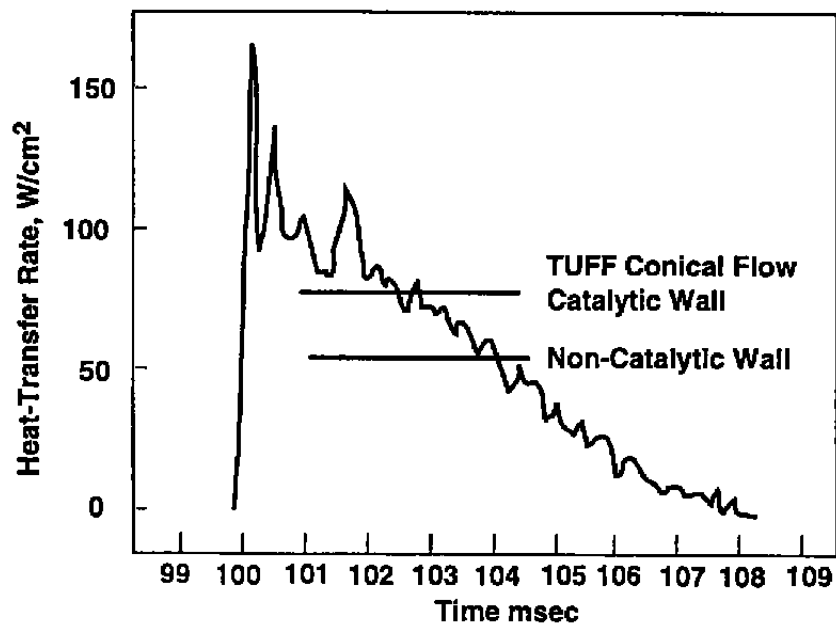
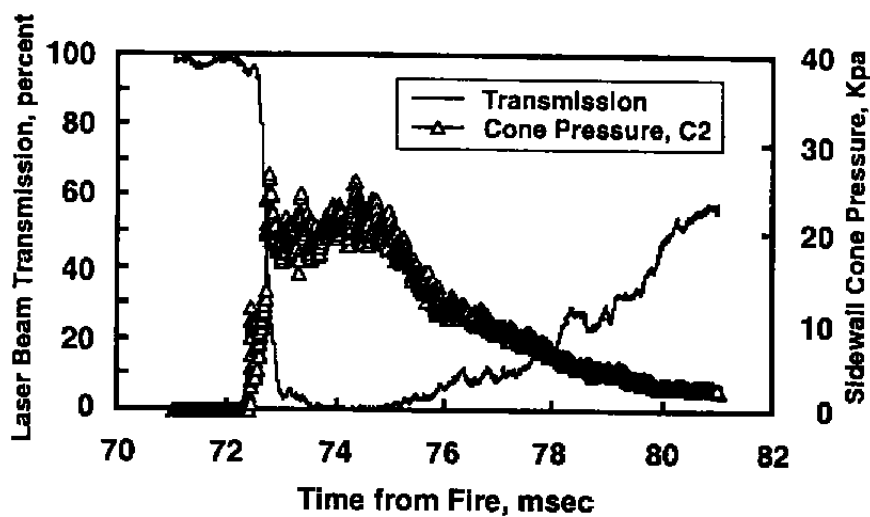
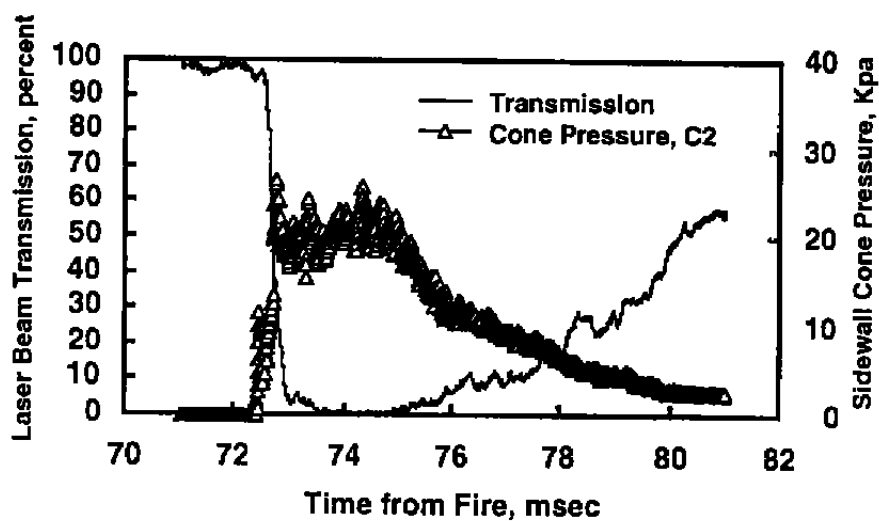


Figure 38. Comparison of computed afterbody heat transfer with measurement, Run 13.

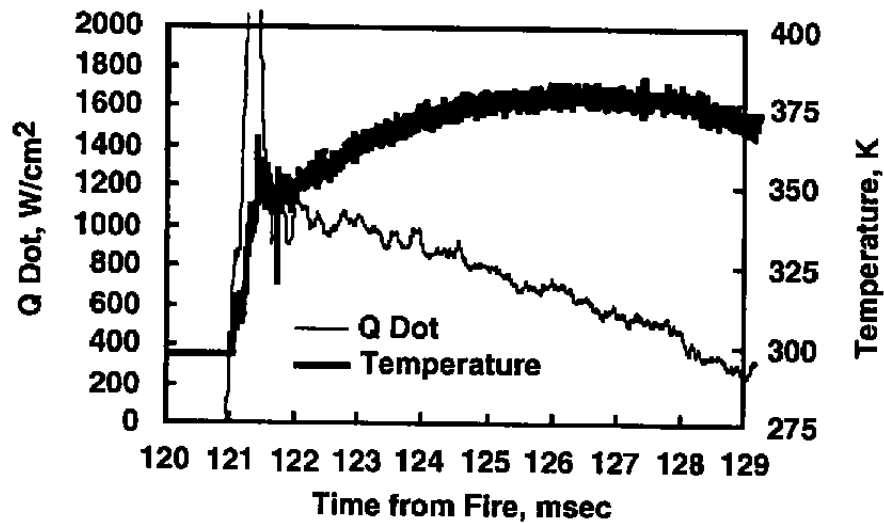


a. Run 21, ST6 = 586 bar

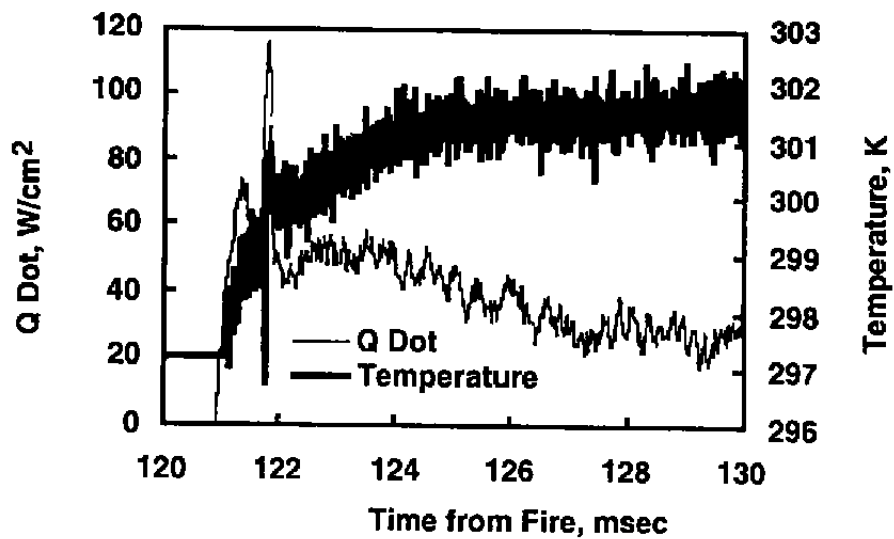


b. Run 25, ST6 = 1,724 bar

Figure 39. Laser beam transmission measurements.

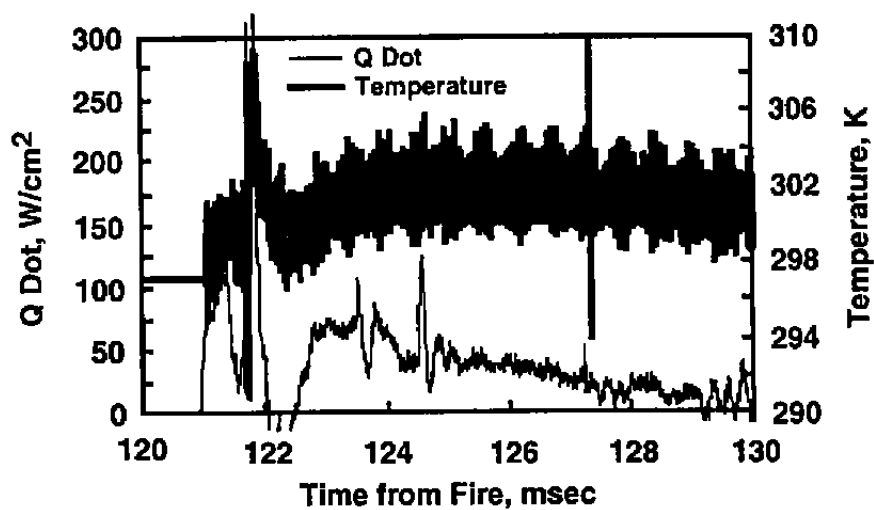


a. Coaxial Thermocouple Gage T6

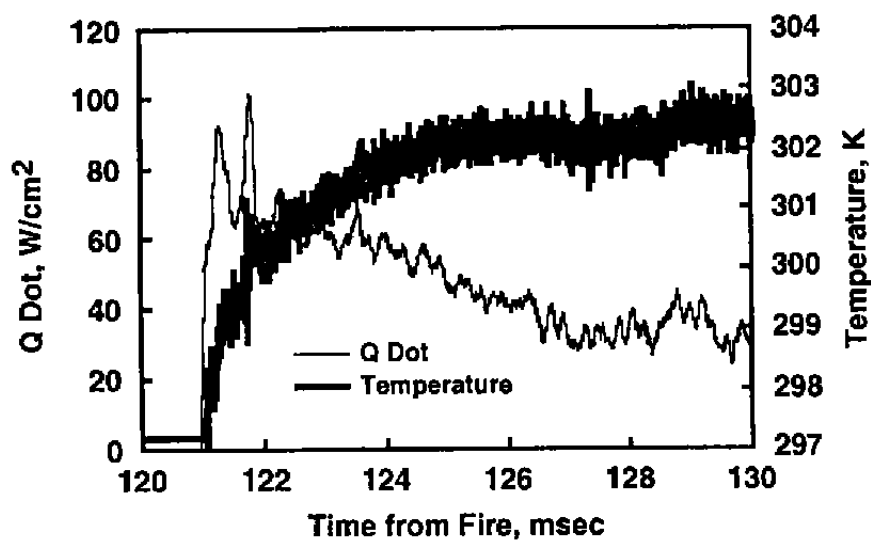


b. Coaxial Thermocouple Gage T7

Figure 40. Flow probe measurements, Run 20.



c. Coaxial thermocouple Gage T8



d. Coaxial Thermocouple Gage T9

Figure 40. Concluded.

**Table 1. Dimensions of Principal Components of the Impulse Facility**

Length of Compression Tube	27.5 m
Diameter of Compression Tube	20.3 cm
Powder Chamber Length	0.5 m
Piston Mass	50 – 115 kg
Length of Shock Tube	12.2 m
Diameter of Shock Tube	7.62 cm
Nozzle Throat Diameter	0.95 – 1.90 cm
Nozzle Exit Diameter	45.7 cm
Test Section Diameter	1.07 m

**Table 2. Impulse Facility Instrumentation**

Powder Chamber	2 Pressure Transducers
Compression Tube	6 Piston Probes
High-Pressure Section	2 Pressure Transducers
Shock Tube	6 Pressure Transducers
Facility Recoil	1 LVDT
Nozzle	12 Pressure Transducers
Data Recorders	48 Channels LeCroy 6810
Test Section Flow	Flow-Field Rake, 13 Pressure Transducers Cal. Model: 4 Pressure Transducers 5 Coaxial Thermocouples Probe: 5 Coaxial Thermocouples
Test Section/Model Flow	30-cm-diam Schlieren System

Table 3. Impulse Facility Run Matrix

Run Number	Date	Charge Pressure, bar		Shock Tube Temp., K	Diaphragm		Helium Compression			
		PT, He	ST, Air		Burst Pressure, bar	Material	Isentropic Process		Math Model Shock Process	
							Comp. Ratio	Temp., K	Comp. Ratio	Temp., K
1	04-07-93	3.57	0.30	298	690	304 SS	23.4	2,435	19.7	2,798
2	04-13-93	2.37	0.30	299	690	304 SS	23.5	2,455	17.2	2,730
3	04-21-93	6.99	0.30	298	690	304 SS	30.1	2,885	25.7	3,226
4	04-26-93	7.99	0.40	297	1,379	304 SS	23.8	2,462	---	---
5	04-30-93	1.80	0.86	298	1,379	304 SS	22.0	2,337	17.6	2,581
6	05-06-93	2.40	0.31	301	690	304 SS	35.5	3,245	31.8	3,596
7	05-12-93	5.04	0.40	301	690	304 SS	29.8	2,890	23.2	3,156
8	05-14-93	1.41	0.80	299	1,034	304 SS	24.4	2,519	18.5	2,709
9	06-17-93	3.50	0.40	302	690	304 SS	41.0	3,588	36.8	3,939
10	06-18-93	5.00	1.00	302	1,379	304 SS	36.1	3,293	25.2	3,580
11	06-22-93	4.99	0.81	302	1,034	304 SS	24.5	2,545	18.6	2,725
12	06-24-93	4.99	1.20	302	1,379	304 SS	29.2	2,859	20.6	3,134
13	06-28-93	4.92	1.20	302	1,379	304 SS	29.2	2,858	20.6	3,129
14	01-13-94	5.00	1.50	297	1,724	NA7	33.6	3,091	23.1	3,462

Table 3. Continued

Run Number	Date	Charge Pressure, bar		Shock Tube Temp., K	Diaphragm		Helium Compression			
		PT, He	ST, Air		Burst Pressure, bar	Material	Isentropic Process		Math Model Shock Process	
							Comp. Ratio	Temp., K	Comp. Ratio	Temp., K
15	01-18-94	3.06	0.80	293	1,034	304 SS	24.5	2,475	18.6	2,734
16	01-24-94	3.26	0.45	297	1,034	304 SS	32.9	3,049	27.7	3,404
17	03-14-94	3.97	0.81	298	1,379	304 SS	37.7	3,353	28.6	3,700
18	03-16-94	4.97	1.20	298	1,724	NA7	38.2	3,386	29.5	3,765
19	03-18-94	3.03	1.00	298	1,379	304 SS	29.2	2,832	20.1	3,119
20	01-11-95	3.02	0.45	299	1,034	304 SS	33.1	3,081	27.8	3,419
21	01-13-95	4.53	0.60	298	1,379	304 SS	39.4	3,456	34.7	3,830
22	01-17-95	3.02	1.46	299	2,069	NA7	39.5	3,464	29.8	3,892
23	01-20-95	2.99	0.60	298	1,379	304 SS	39.6	3,468	34.9	3,853
24	03-13-95	3.02	0.61	299	1,379	304 SS	39.4	3,468	34.7	3,830
25	03-14-95	6.99	1.30	300	2,759	NA7	36.1	3,278	26.4	3,737

Table 3. Continued

Run Number	Piston Mass, kg	Powder Type	Throat		Max. Piston Velocity, m/sec	Avg. Shock Tube Mach Number	Recoil, cm	(1) Stag. Press., bar	Remarks
			Diam, cm	Material					
1	78.0	105mm	1.91	MOLY	260	8.81	---	224	Diaphragm partial open
2	77.6	105mm	1.91	MOLY	331	9.03	---	497	Diaphragm partial open
3	77.3	105mm	1.91	MOLY	272	12.24		414	Cracked nozzle
4	77.8	155mm	1.27	MOLY	360	---	4.32	---	Diaphragm failed to burst
5	77.6	155mm	1.27	MOLY	418	11.15	4.57	1,034	Ablated ST wall
6	77.6	105mm	1.27	MOLY	240	12.81	3.35	345	Cracks in nozzle insert
7	77.1	105mm	1.91	FS60	286	11.15	3.99	400	
8	77.6	155mm	1.91	FS60	340	11.24	4.29	690	
9	77.1	105mm	1.91	FS60	267	12.17	3.94	400	Cu liner in ST; ST leak
10	77.6	155mm	1.91	FS60	358	12.72	4.57	(690)	Missed ST6
11	77.3	155mm	1.91	FS60	345	11.71	4.45	(690)	Missed ST6
12	77.6	155mm	1.91	FS60	408	12.50	---	(1,103)	Missed ST6 & Model Gages
13	77.6	155mm	1.91	FS60	390	10.44	4.57	897	Diap. didn't open fully
14	77.1	155mm	1.91	FS60	439	10.07	N/A	(1,172)	Failed throat, Lost Petals on piston rebound
15	77.1	155mm	1.91	TZM	338	10.46	4.14	(676)	Repeat Run 8

**Table 3. Concluded**

Run Number	Piston Mass, kg	Powder Type	Throat		Max. Piston Velocity, m/sec	Avg. Shock Tube Mach Number	Recoil, cm	(1) Stag Press., bar	Remarks
			Diam, cm	Material					
16	77.1	105mm	1.91	TZM	285	11.83	3.89	566	Failed throat
17	77.6	155mm	1.91	FS60	317	12.98	4.14	(759)	No PLIF; No ST6
18	77.6	155mm	1.91	FS60	367	10.95	4.55	897	Problem with shaped diaphragm: No PLIF
19	77.6	155mm	1.91	FS60	363	11.53	4.37	876	
20	77.6	105mm	1.91	FS60	289	10.34	N/A	428	Repeat of Run 16: Good Run
21	78.0	155mm	1.91	FS60	319	11.14	4.17	586	Good Run
22	77.1	155mm	1.91	FS60	413	10.55	4.93	1,310	Failed ST6 Gage, Ablation contaminated flow
23	77.6	155mm	1.91	FS60	321	11.19	N/A	490	Repeat of Run 21; Good Run
24	77.1	155mm	1.91	W-Cu	315	12.3	4.27	566	Good Run
25	77.6	155mm	1.91	W-Cu	495	12.5	5.61	1,724	HPS Diaphragm particles; Ablation contamination of flow

**Table 4. Nozzle Insert Materials and Performance**

Throat Number	Throat Diam, cm	Throat Material	Number Runs	Remarks
1	1.91	Molybdenum	3	Cracked Insert
2	1.27	Molybdenum	3	Cracked Insert
3	1.91	Fansteel 60 <sup>®</sup>	8	Cracked Insert
4	1.91	TZM	2	Cracked Insert
5	1.91	Fansteel 60 <sup>®</sup>	7	Retired for Analysis
6	1.91	W-20 Percent Cu	2	Damaged Run 25

Table 5. Nozzle Reservoir Conditions

Run Number	Reflected Shock Mach Number	Reflected Shock Conditions					Measured Pressure P5' (ST6), bar	Isentropic Adjustment	
		P1 Air, bar	P5, bar	H5, MJ/kg	T5, K	S5/R		H5, MJ/kg	T5, K
1	8.5	0.301	240.6	9.35	5,552	32.37	224	9.23	5,483
2	9.2	0.301	302.1	11.00	6,328	33.07	497	12.06	6,885
3	11.1	0.400	672.6	16.04	8,334	34.56	414	14.72	7,759
5	10.7	0.861	1,286.6	14.95	8,293	33.33	1034	14.37	8,002
6	10.9	0.308	496.9	15.46	8,046	34.68	345	14.50	7,625
7	9.8	0.398	475.8	12.52	7,051	33.35	400	12.13	6,852
8	10.8	0.802	1,229.7	15.22	8,366	33.50	690	13.71	7,617
9	11.0	0.402	660.2	15.76	8,248	34.47	400	14.42	7,617
10	11.5	1.001	1,804.7	17.26	9,151	33.88	690	14.54	7,904
11	10.2	0.811	1,063.8	13.59	7,718	32.95	690	12.55	7,173
12	11.8	1.199	2,300.1	18.17	9,533	33.94	1103	15.95	8,539
13	9.0	1.203	1,111.9	10.52	6,377	31.37	897	10.09	6,124
14	8.5	1.497	1,191.2	9.37	5,806	30.63	1172	9.34	5,790

Table 5. Concluded

Run Number	Reflected Shock Mach Number	Reflected Shock Conditions					Measured Pressure P5' (ST6), bar	Isentropic Adjustment	
		P1 Air, bar	P5, bar	H5, MJ/kg	T5, K	SS/R		H5', MJ/kg	T5', K
15	9.0	0.800	742.1	10.52	6,299	31.81	676	10.33	6,192
16	9.5	0.452	493.1	11.75	6,757	32.92	566	12.05	6,916
17	11.4	0.807	1,428.4	16.95	8,943	34.04	759	15.15	8,133
18	9.0	1.203	1,111.9	10.52	6,377	31.37	897	10.09	6,124
19	10.1	1.001	1,271.1	13.32	7,676	32.62	876	12.44	7,199
20	8.7	0.591	500.7	9.81	5,887	31.84	428	9.52	5,721
21	9.8	0.598	707.3	12.52	7,170	32.90	586	12.10	6,945
22	9.0	1.465	1,352.9	10.53	6,419	31.16	1310	10.46	6,380
23	9.7	0.599	687.3	12.27	7,059	32.81	490	11.52	6,661
24	11.1	0.607	1,009.1	16.06	8,526	34.09	566	14.49	7,810
25	11.6	1.303	2,389.8	17.57	9,392	33.67	1724	16.58	8,939

Table 6. Free-Stream Conditions

Run Number	Flow Conditions at Nozzle Exit						Model Stagnation Conditions			
	Mach Number	Static Pressure, torr	Enthalpy, MJ/kg	Static Temp, K	Velocity, m/sec	Density, kg/m <sup>3</sup>	Enthalpy, MJ/kg	Pressure, bar	Temp, K	Q DOT (1), w/cm <sup>2</sup>
1	6.76	9.78	0.759	996	4,176	4.55E-03	9.77	0.77	4,939	794
2	6.37	25.8	1.269	1,424	4,666	8.40E-03	12.44	1.77	5,759	1,596
3	6.00	23.6	1.944	1,949	5,060	5.60E-03	15.06	1.40	6,164	1,767
5	7.09	17.3	1.211	1,377	5,112	5.79E-03	14.56	1.47	6,101	1,745
6	6.85	5.6	1.290	1,441	5,044	1.78E-03	14.29	0.44	5,774	932
7	6.31	18.2	1.295	1,444	4,654	5.84E-03	12.40	1.23	5,673	1,323
8	6.21	35.3	1.589	1,682	4,916	9.72E-03	13.96	2.28	6,128	2,077
9	6.01	22.7	1.907	1,921	5,035	5.48E-03	14.89	1.35	6,133	1,717
10	6.10	37.7	2.137	1,873	5,063	9.36E-03	14.95	2.33	6,286	2,271
11	6.35	34.4	1.645	1,487	4,749	1.15E-02	12.90	2.51	5,932	1,986
12	6.07	61.7	2.462	2,099	5,285	1.36E-02	16.43	3.70	6,619	3,179
13	6.77	38.3	0.872	1,092	4,371	1.75E-02	10.71	3.22	5,468	1,819
14	7.09	45.0	0.898	857	4,081	2.43E-02	9.22	3.89	5,012	1,685
15	6.15	36.0	2.019	1,783	4,996	1.00E-02	14.49	2.43	6,228	2,235

Note. (1) Fay-Riddell equilibrium heat-transfer rate at stagnation point with 1.78-cm nose radius

Table 6. Concluded

Run Number	Flow Conditions at Nozzle Exit						Model Stagnation Conditions			
	Mach Number	Static Pressure, torr	Enthalpy, MJ/kg	Static Temp., K	Velocity, m/sec	Density, kg/m <sup>3</sup>	Enthalpy, MJ/kg	Pressure, bar	Temp., K	Q DOT (1), w/cm <sup>2</sup>
16	6.41	27.7	1.531	1,396	4,651	9.77E-03	12.33	2.05	5,768	1,700
17	6.04	42.5	2.364	2,037	5,194	9.67E-03	15.87	2.54	6,434	2,532
18	6.85	36.2	1.030	972	4,228	1.73E-02	9.96	2.98	5,228	1,609
19	6.43	42.7	1.573	1,428	4,715	1.39E-02	12.67	2.99	5,924	2,123
20	6.78	18.3	1.084	1,025	4,246	8.27E-03	10.10	1.44	5,141	1,132
21	6.43	28.5	1.508	1,382	4,639	9.56E-03	12.26	1.99	5,747	1,666
22	6.90	53.7	1.067	1,012	4,295	2.47E-02	10.29	4.39	5,401	2,029
23	6.43	23.8	1.476	1,356	4,599	8.12E-03	12.04	1.66	5,662	1,490
24	6.05	31.8	2.197	1,923	5,075	7.60E-03	15.09	1.91	6,251	2,071
25	6.10	98.3	2.619	2,207	5,419	2.06E-02	17.31	5.89	6,878	4,253

Note: (1) Fay-Ridell equilibrium heat-transfer rate at stagnation point with 1.78-cm nose radius

**Table 7. Impulse Tunnel Spatial and Temporal Flow Variation**  
**a. Spatial Variation in Pitot Probe Measurements**

Run Number	Range of Average, msec	Average Pitot Probe Measurements												Overall Average, bar	(1) Std Dev, bar	Std Dev, %
		PT1, bar	PT2, bar	PT3, bar	PT4, bar	PT5, bar	PT6, bar	PT7, bar	PT8, bar	PT9, bar	PT10, bar	PT11, bar	PT13, bar			
0001	N/A	N/A	N/A	N/A	N/A	N/A	N/A	N/A	N/A	N/A	N/A	N/A	N/A	N/A	N/A	N/A
0002	117-118	1.30	1.38	1.51	N/A	1.87	1.85	1.44	1.49	1.63	1.46	1.47	1.35	1.52	0.189	12.38
0003	147-148	1.39	1.44	1.38	1.30	1.42	1.41	1.31	1.39	1.38	N/A	1.64	N/A	1.41	0.092	6.57
0004	N/A	N/A	N/A	N/A	N/A	N/A	N/A	N/A	N/A	N/A	N/A	N/A	N/A	N/A	N/A	N/A
0005	96-98	2.10	2.07	2.11	2.12	2.15	2.14	1.97	2.01	2.08	2.13	2.09	2.04	2.08	0.054	2.61
0006	158-159	0.53	0.53	0.52	0.55	0.50	0.61	0.61	0.58	0.54	0.56	0.53	0.63	0.56	0.040	7.25
0007	130.5-131.5	1.44	1.43	1.43	1.50	1.52	1.46	1.38	1.47	N/A	1.41	1.38	1.34	1.43	0.054	3.76
0008	*117.5-118.5	2.21	2.49	2.49	2.52	2.84	2.60	2.43	2.53	N/A	2.58	2.50	2.50	2.52	0.148	5.88

Notes (1) Standard deviation based on a sample

(2) Position PT12 occupied by hemisphere rather than a pitot pressure gage

**Table 7. Concluded**  
**b. Temporal Variation in Pitot Probe Measurements**

Run Number	Range of Average, msec	Average Pitot Probe Measurements												Overall Average, Std Dev, %
		PT1, %	PT2, %	PT3, %	PT4, %	PT5, %	PT6, %	PT7, %	PT8, %	PT9, %	PT10, %	PT11, %	PT13, %	
0001	N/A	N/A	N/A	N/A	N/A	N/A	N/A	N/A	N/A	N/A	N/A	N/A	N/A	N/A
0002	117-118	14.17	13.70	12.53	N/A	13.81	12.58	16.72	11.34	12.96	14.60	11.78	13.47	13.42
0003	147-148	9.59	8.28	6.89	7.50	7.42	6.87	6.99	6.96	7.87	7.04	8.04	N/A	7.59
0004	N/A	N/A	N/A	N/A	N/A	N/A	N/A	N/A	N/A	N/A	N/A	N/A	N/A	N/A
0005	96-98	4.20	4.09	4.12	4.13	3.92	2.60	3.29	3.91	3.60	5.30	4.60	4.57	4.03
0006	158-159	14.26	15.22	14.42	12.24	15.96	11.01	11.16	18.23	15.54	12.44	10.51	5.96	13.08
0007	130.5-131.5	N/A	4.79	5.97	5.29	6.22	6.22	6.95	4.49	5.70	6.84	7.01	5.22	5.88
0008	117.5-118.5	12.68	9.44	10.30	8.65	10.20	9.94	8.81	8.68	N/A	13.47	13.09	14.88	10.92

**Table 8. Math Model Predictions of Gas Arrival Times**

Run Number	Gas Arrives at Nozzle Entrance			Gas Arrives at Nozzle Exit			Flow Area, (1) cm <sup>2</sup>
	Air, msec	Helium, msec	Delta, msec	Air, msec	Helium, msec	Delta, msec	
1	3 604	6 027	2 423	3 986	7 578	3 592	26 4
2	3 688	5 276	1 588	4 060	6 586	2 526	26 4
3	3 132	5 145	2 013	3 463	6 472	3 009	45 6
5	3 414	5 416	2 002	3 767	6 732	2 965	45 6
6	2 853	4 593	1 740	3 175	5 840	2 665	45 6
7	3 230	5 182	1 952	3 572	6 430	2 858	45 6
8	3 564	5 974	2 410	3 905	7 341	3 436	45 6
9	2 867	4 939	2 072	3 178	6 189	3 011	45 6
10	3 382	6 167	2 785	3 742	7 524	3 782	45 6
11	3 565	6 022	2 457	3 908	7 388	3 480	45 6
12	3 534	6 218	2 684	3 906	7 640	3 734	45 6
13	3 536	6 295	2 759	3 909	7 650	3 741	45 6
14	3 476	6 241	2 765	3 832	7 617	3 785	45 6
15	3 557	5 978	2 421	3 900	7 339	3 439	45 6
16	2 961	4 774	1 813	3 271	6 053	2 782	45 6
17	3 148	5 785	2 637	3 498	7 126	3 628	45 6
18	3 194	6 343	3 149	3 512	7 802	4 290	45 6
19	3 522	6 415	2 893	3 881	7 799	3 918	45 6
20	2 995	4 781	1 786	3 267	6 055	2 788	45 6
20A	3 189	5 254	2 065	3 534	6 615	3 081	30 4
21	2 770	4 545	1 775	3 082	5 766	2 684	45 6
21A	3 019	5 148	2 129	3 345	6 444	3 099	27 1
22	3 178	6 402	3 224	3 494	7 869	4 375	45 6
23	2 767	4 534	1 767	3 076	5 750	2 674	45 6
23A	3 058	5 189	2 131	3 389	6 459	3 070	25 6
24	2 778	4 576	1 798	3 088	5 804	2 716	45 6
25	2 944	4 919	1 975	3 262	6 138	2 876	45 6

Notes: (1) Assumed flow area at HPS diaphragm location. Math model uses turbulent boundary-layer option. Times calculated from burst of HPS diaphragm.

Table 9. Calibration Cone Pressure Measurements

Run Number	Cone Pressure Gage Measurements (1), (2), (4)							
	C1		C2		C3		C4	
	Pressure, kPa	Std. Dev., percent	Pressure, kPa	Std. Dev., percent	Pressure, kPa	Std. Dev., percent	Pressure, kPa	Std. Dev., percent
9	X	X	X	X	X	X	X	X
10	X	X	X	X	X	X	X	X
11	X	X	X	X	X	X	X	X
12	X	X	X	X	X	X	X	X
13	9 710	4 09	X	X	9 26	3 08	X	X
14	X	X	X	X	X	X	X	X
15	(3)	(3)	(3)	(3)	(3)	(3)	(3)	(3)
16	1 889	9 74	1 901	8 80	1 76	8 88	1 585	8 46
17	3 035	4 16	2 991	4 68	2 87	5 71	2 494	5 85
18	4 038	3 08	4 081	3 04	3 65	3 3	3 121	2 83
19	4 084	5 88	3 946	5 92	3 49	6 32	3 088	4 90
20	4 193	17 25	4 542	7 94	X	X	X	X
21	5 465	14 95	5 840	4 00	X	X	X	X
22	12 834	6 17	13 434	3 47	X	X	10 593	6 28
23	6 020	6 38	5 860	8 09	X	X	4 563	6 00
24	6 237	3 32	6 117	3 64	X	X	4 756	3 85
25	20 441	2 93	20 524	5 97	X	X	15 779	5 12

- Notes: (1) Averaged over 1-msec interval with interval beginning 1 msec from the initial pressure rise  
 (2) All data processed through a low-pass (10 000 Hz) Butterworth filter prior to analysis  
 (3) Data affected by a noise spike produced by the schlieren system laser  
 (4) PCB Pressure Gage Model No. 113A02, Range to 100 psi used on runs 9 – 12. Two PCB Pressure Gages Model No. 113A02 and two Kulite™ Pressure Gages, Model XCS-093-5D, used on Run 13. Kulite Pressure Gages Model XCS-093-5D used on Runs 14–25.

Table 10. Flow Probe Average Heat-Transfer Rates

Run Number	(1) Channel	Initial Rise Time, msec	Time Interval for Average Q DOT, msec	Average Q DOT, Btu/ft <sup>2</sup> -sec	Average Q DOT, w/cm <sup>2</sup>	(2) Q DOT Ratio
20	T6	121 025	122 025-123 025	956 3	1085 8	1 000
	T7	121 015	122 015-123 015	40 4	45 9	0 042
	T8	121 005	123 000-124 000	61 6	69 9	0 064
	T9	121 015	122 015-123 015	56 2	63 8	0 059
21	T6	116 885	117 885-118 885	878 1	997 0	1 000
	T7	116 885	117 885-118 885	51 5	58 5	0 059
	T8	116 885	119 000-120 000	64 8	73 6	0 074
	T9	116 885	117 885-118 885	61 7	70 1	0 070
23	T6	115 095	116 095-117 095	793 7	901 2	1 000
	T7	115 090	116 090-117 090	70 6	80 2	0 089
	T8	115 090	116 090-117 090	64 4	73 1	0 081
	T9	115 090	116 090-117 090	75 8	86 1	0 096
24	T6	122 395	123 395-124 395	2028 0	2302 7	1 000
	T8	122 405	123 405-124 405	79 4	90 2	0 039
	T10	122 405	123 405-124 405	118 4	134 4	0 058
25	T8	72 400	73 400-74 400	219 9	249 7	N/A

Notes: (1) Channels not listed produced no data.

(2) Defined as channel number divided by stagnation Q DOT.

Example: Run 21 (Q DOT 7)/(Q DOT 6) = 0 059

## APPENDIX A THERMAL ANALYSIS OF THROAT HEATING IN THE FREE-PISTON IMPULSE TUNNEL

### A1.0 INTRODUCTION

The extreme conditions ( $p_0 = 10,000$  atm,  $T_0 = 10,000$  K) desired in the AEDC Free-Piston Impulse Tunnel will cause intense throat heating (750,000 Btu/ft<sup>2</sup>-sec), resulting in melting, vaporization, or oxidation of even the best heat-sink throat materials. Innovative methods of cooling the throats will be necessary to test for even 1 to 1.5 msec at the more extreme test conditions. The analysis presented here is a detailed thermal study of several areas of importance. It includes an evaluation of convective throat heating prediction methods with comparisons of the available throat heating data from high-performance test facilities. A sophisticated computer code (the BLIMP Code, Ref. A-1) is used to calculate the chemically reacting (equilibrium) boundary layer through a Free-Piston Impulse Tunnel throat, and these calculations are also compared with the experimental data. The effectiveness of transpiration cooling the throat region by injecting air or helium is evaluated. It appears that reductions in the throat heat-transfer rate of a factor of five or more are feasible, with air coolant injection rates of 3.5 percent of the mass flowing through the throat. Helium is an even more effective coolant whenever the same mass is injected. Finally, a possible approach to the hardware design required for a transpiration-cooled throat is given.

Several other aspects of the throat heating problem still need to be investigated. For example, evaluation studies should be made of film cooling methods, as well as the feasibility of using an ablating throat (graphite, carbon phenolic, etc.). Further work needs to be done in the transpiration cooling area, including stress analysis of a typical throat structure, evaluation of the feasibility of high injection rates, estimation of coolant contamination effects, and hardware cost estimates.

### A1.1 PREDICTION OF CONVECTIVE HEATING

The objective here is to evaluate correlations or theoretical computations of nozzle throat heat-transfer rates at severe test conditions, through comparisons with the available experimental data. Once successful comparisons between theory and experiment are obtained, the prediction method will be used to extrapolate to the severe test conditions generated in the Free-Piston Impulse Tunnel. Experimental data from three test facilities are used here:

1. NOL 1.5-in. Hypersonic Shock Tunnel No. 2
2. HEAT-H1 Arc Facility
3. GALCIT T5 Free-Piston Shock Tunnel

## A1.2 EXPERIMENTAL DATA

### NOL 1.5-in. Hypersonic Shock Tunnel No. 2

Noonan and Rand presented turbulent heat-transfer rate measurements from the throat region (a constant diameter throat, 0.25 in. diameter by 3.5 in. long) of a reflected shock tunnel in Ref. A-2. The facility operated at total temperatures of 3,900 – 9,000 K and total pressures of 124 to 423 atm, while heat-transfer rates up to 50,000 Btu/ft<sup>2</sup>-sec were measured with a ring-type calorimeter heat-transfer rate gage. A total of five heat-transfer rate measurements taken at different facility reservoir conditions are given in Fig. A-1, where the data are presented in terms of correlation parameters similar to those used by Enkenhus and Maher, Ref. A-3.

### HEAT-HI Arc Facility

During each run in HI, the total integrated heat transfer in the throat region can be determined by measurements of the rise in the cooling water temperature as it flows through the nozzle. The peak throat heat-transfer rate can be deduced with the aid of a boundary-layer code (the TBL code was used) that calculates the heat-transfer rate distribution in the nozzle. The calculated integrated heat-transfer rate over the nozzle is forced to match the measured integrated heat-transfer rate by iterating on the flow enthalpy (which is not known because of the large enthalpy gradients across the HI flow).

The HI test conditions are less severe than the NOL shock tunnel data described above. The three HI data points presented in Fig. A-1 were obtained at total temperatures of 3,800 – 5,000 K, at total pressures of 122 – 127 atm, in different HI nozzles. Throat heat-transfer rates of 6,500 to 10,000 Btu/ft<sup>2</sup>-sec were deduced for the HI tests.

### GALCIT T5 Free-Piston Shock Tunnel

Data obtained in the T5 Facility were measured at conditions closer to the extreme conditions desired in the AEDC Free-Piston Impulse Tunnel. In T5, stagnation temperatures of 7 – 10,000 K, and stagnation pressures of 1,000 atm are run, giving peak throat heat-transfer rates of 80 – 90,000 Btu/ft<sup>2</sup>-sec. However, the T5 "measurements" consist solely of observations of the condition of the throat after a facility run. By observing the throat after the typical 3-msec run (2 msec of hot flow), it may be deduced whether or not the surface of the throat has reached the melt temperature of the particular throat material. From this information a maximum or minimum heat-transfer rate can be deduced (depending on whether or not the throat melted) using semi-infinite slab conduction heat-transfer rate theory. If the throat has melted, a minimum heat-transfer rate can be deduced, because the heat-transfer rate must be at least high enough to melt the throat in 2 msec (of hot flow). However, the throat could have melted earlier than 2 msec — say 1 or 0.5 msec, etc. This would imply a larger heat-transfer rate than if the throat melted in 2 msec.

On the other hand, if the throat has not melted in 2 msec, a maximum heat-transfer rate may be deduced. The heat-transfer rate cannot be higher than that required to melt the throat surface in 2 msec. However, the heat-transfer rate can be any amount lower than this.

Several throat materials have been tested at T5, including tungsten, copper, beryllium-copper, Narloy Z, steel, and molybdenum. A summary of the observations of the condition of the throats after the various T5 runs was given to the author by Dr. Hans Hornung during a visit to AEDC in April 1992. All throats were tested at  $T_0 = 7,280$  K and  $p_0 = 987$  atm, unless noted.

1. The molybdenum throat does not melt, but begins to form a longitudinal crack during the second run. (It looks okay after the first run.) The crack gets worse, until finally the throat must be discarded after five to six runs.
2. The steel throat melts at the  $p_0 = 500$  atm/ $T_0 = 7,280$  K test conditions.
3. The steel throat does not melt at the  $p_0 = 200$  atm/ $T_0 = 7,280$  K test condition.
4. The tungsten throat diameter gets bigger by 0.010 in. during the run ( $d^* = 1.22$  in.). It probably oxidizes.
5. The Narloy Z throat yields because it is too soft. The diameter is larger after the run.
6. The beryllium-copper throat gets bigger during the run.
7. The pure copper throat melts if it is rough (from diaphragm nicks). Otherwise it does not melt. Copper is too soft.

Observations 1–3 were used to deduce peak throat heat-transfer rates in T5 at the different test conditions. These three data points are shown in Fig. A-1. Note that the T5 data are shown as a maximum or minimum heat-transfer rate with an arrow indicating that the heat-transfer rate could be either higher ( $\uparrow$ ) or lower ( $\downarrow$ ) than the value calculated for 2 msec.

### A1.3 CORRELATIONS

Enkenhus and Maher (Ref. A-3) presented an aerodynamic design method for axisymmetric nozzles operating with high-temperature air. A correlation (referred to here as the "NOL correlation") of the peak heat-transfer rate for nozzles operating over a range of reservoir conditions is given in the report. This correlation has been used extensively at AEDC for fast estimates of throat heating rates, and the entire turbulent boundary-layer calculation procedure is available at AEDC in a computer code (TBL Code) that was written 25 years ago by this author. The correlation relates the peak throat heat rate to the nozzle reservoir conditions and the nozzle geometry as follows:

$$\frac{q}{(T_0 - T_w)} = 0.043 \frac{p_0^{0.74} T_0^{0.21}}{(r^* R_t)^{0.5}}$$

where:

- $p_o$  Reservoir pressure, atm
- $\dot{q}$  Peak heat-transfer rate in the throat region, Btu/ft<sup>2</sup>-sec
- $r^*$  Throat radius, ft
- $R_c$  Radius of curvature of the throat, ft
- $T_o$  Reservoir temperature, K
- $T_w$  Wall temperature, K

For the present application, it was necessary to modify the correlation by eliminating the geometry term, " $(r^*R_c)^{0.05}$ ", because the NOL Hypersonic Shock Tunnel No. 2 data were measured in a constant diameter throat (an infinite  $R_c$ ). The use of the geometry term was questionable for the Free-Piston Impulse Tunnel throats anyway. It was derived based on turbulent boundary calculations for typical, large  $R_c$  (1 to 5 ft), hypersonic nozzles, and its use for the small Free-Piston Impulse Tunnel throats ( $R_c = 0.5$  in. or less) represents a large extrapolation in scale. The geometry term was eliminated by substituting a value of 0.833 for " $(r^*R_c)^{0.05}$ ", which is the average value of the geometry term for the NOL hypersonic nozzles used in the correlation. The modified correlation becomes:

$$\frac{\dot{q}}{T_o - T_w} = \frac{0.0043}{0.833} p_o^{0.74} T_o^{0.31} = 0.00516 p_o^{0.74} T_o^{0.31}$$

Both the new correlation and the unmodified correlation are plotted in Fig. A-1. The unmodified correlation is given for the 0.5-in. throat diameter of the Free-Piston Impulse Tunnel, i.e., the intermediate size throat.

#### A1.4 SUMMARY OF PEAK THROAT HEATING

The summary in Fig. A-1 includes all the experimental data together with the correlations mentioned above. The correlation used by Mr. Brian Feather to predict throat heat-transfer rates for the Free-Piston Impulse Tunnel is also shown in the figure. Feather has published a series of handy graphs for rapidly estimating the peak throat heat-transfer rate based on the correlation line shown in the figure.

In general, there is considerable scatter in the experimental data, as might be expected with this type of data. From an overall point of view, though, the data from all the facilities fall into the expected trends with test conditions. All of the correlations shown in the figure fall within the broad limits of the T5 data. However, the unmodified NOL correlation (which includes the geometry

term) is too high, indicating that the " $(r^*R_c)^{0.05}$ " term is not a good extrapolating factor for the test conditions of the various experimental data presented here.

The line in Fig. A-1 referred to as the "best fairing" of the experimental data was chosen by giving less weight to the highest heat-transfer rate data point taken in the NOL facility ( $h = 8.8$ ), because this data point was not consistent with boundary-layer theories shown in Fig. 11 of Ref. A-2. Also, the "best fairing" was in good agreement with the BLIMP boundary-layer code results given in Fig. A-2 of this memorandum. The "best fairing" is about 20 percent lower than the correlation used by Feather. In view of the large scatter in the data, Feather's correlation could be considered a conservative estimate of the peak throat heat-transfer rate.

The BLIMP calculations given in Fig. A-2, and results given later in the transpiration cooling section, were made for the largest Free-Piston Impulse Tunnel throat ( $d^* = 0.75$  in.) shown in Fig. A-3. The pressure distribution required as input to the BLIMP code was calculated by performing a real-gas, one-dimensional expansion in the nozzle using the ACE code, Ref. A-4. The Cebeci turbulence model was used in BLIMP to be consistent with the present recommended method for calculating the heat-transfer rate in rocket nozzles. The results in Fig. A-2 show good agreement between the BLIMP code and the experimental data. It is important to have an analysis tool like the BLIMP code available because it can be used to calculate heat-transfer rate distributions in the nozzle (not just the peak heat-transfer rate); it can be used to confidently extrapolate the affect of  $R_c$ , for example, since it is based on boundary-layer fundamentals, and it can be used to estimate the affect of injecting various coolants into the boundary layer. It will be used later in this memorandum to estimate cooling effects.

Peak throat heat-transfer rates based on the BLIMP code results of Fig. A-2 are given in the following table for both a cold wall ( $540^\circ\text{R}$ ) and a hot wall ( $5,200^\circ\text{R}$ ). The hot wall has a temperature equal to the melting temperature of molybdenum.

**Free-Piston Impulse Tunnel  
Peak Throat Heat-Transfer Rates**

$p_{\infty}$ , atm	$T_{\infty}$ , K	$(T_w = 540^\circ\text{R})$ $\dot{q}$ (Btu/ft <sup>2</sup> -sec)	$(T_w = 5,200^\circ\text{R})$ $\dot{q}$ (Btu/ft <sup>2</sup> -sec)
10,000	10,000	756,600	554,700
4,000	10,000	368,600	270,200
3,500	9,700	310,200	230,000
1,800	9,000	165,300	116,100
1,000	7,280	76,800	48,300

Even with the wall at the melting temperature of molybdenum, the wall heat-transfer rates are extremely high.

### A1.5 HEAT-TRANSFER RATE DISTRIBUTION

In designing the throats for the Free-Piston Impulse Tunnel, it was not clear how long the throat ought to be – i.e., to what area ratio should the flow be expanded before a steel wall could handle the heat loads? It was decided to expand the flow to the point where the largest diameter nozzle ( $d^* = 0.75$  in.) would have a heat-transfer rate not more than 1/4 to 1/5 of the peak heat-transfer rate at the throat. In order to do this, the heat-transfer rate distribution in the supersonic part of the throat had to be estimated.

A review was made of numerous throat heat-transfer calculations that had been made previously for the arc facilities using both the Turbulent Boundary Layer (TBL) code (Edenfield's code) and the Patanker-Spalding Code (calculations by Shope). These data were correlated as a function of area ratio, as shown in Fig. A-4. Later, the BLIMP calculations were available for the large Free-Piston Impulse Tunnel throat, and these calculations corroborate the correlations. Based on these results, the large throat was designed with a supersonic area ratio of 4 (exit diameter = 1.5 in.). The smallest throat ( $d^* = 0.375$  in.) has an area ratio of 16, since all throats have the same exit diameter.

### A2.0 TEMPERATURE RESPONSE FOR A HEAT-SINK THROAT

Even during the short (2 to 3 msec) runs in the Free-Piston Impulse Tunnel, the extremely high heat-transfer rates discussed in the previous section will melt, vaporize, oxidize, or crack any known heat sink material. A few calculations will be given here to show the severity of the problem. The analysis here was made for one test condition – the most severe throat heating condition from a list of tailored-interface shock tunnel runs calculated by Mr. Jim Blanks. The reservoir conditions for this shot are  $p_0 = 3,500$  atm and  $T_0 = 9,700$  K, and the predicted cold-wall heat transfer was given previously as 310,200 Btu/ft<sup>2</sup>-sec. The heat-transfer rate drops off to 230,000 Btu/ft<sup>2</sup>-sec when the wall reaches the melting temperature of molybdenum (5,200°R).

Calculations for the temperature rise in various throat materials are given in Fig. A-5 for the most promising materials. These results were obtained using a semi-infinite solid approximation with a convective boundary condition (see chart 22 of Ref. A-5), which accounts for the reduced heat-transfer rate as the wall heats up. At this test condition, either copper or steel will melt in less than 0.1 msec. The time to melt either molybdenum or tungsten is 3 to 5 times longer, but this performance could be realized only in a nitrogen environment. Both molybdenum and tungsten start to oxidize at relatively low temperatures – around 1,300°F – and this can drastically affect their

performance. Mr. Hank Moody (ATSS) indicates that the internal structure of molybdenum changes from a fine grain structure to a coarse grain structure (brittle material) whenever molybdenum is heated to 2,000°F. With this 2,000°F limitation, a molybdenum throat could be run for only 0.04 msec. The need for throat cooling or another approach to the problem is obvious.

A convective boundary condition was assumed for all of the calculations made here, but the interactions between the various thermal parameters are more easily seen with the constant heat-transfer rate solution:

$$\theta = \frac{\pi p c k}{4 q^2} (T - T_i)^2$$

where:

- c Heat capacity, Btu/lb°F
- k Thermal conductivity, Btu/lb°F ft
- q Heat-transfer rate, Btu/ft<sup>2</sup>-sec
- T<sub>i</sub> Initial temperature, °F
- ρ Density, lb<sub>m</sub>/ft<sup>3</sup>
- θ Time, sec

The constant heat-transfer rate formulation clearly separates the effects of material thermal properties and the effect of cooling. The material thermal properties are included in the term "pck (T-T<sub>i</sub>)<sup>2</sup>", which indicates that the run time of the Free-Piston Impulse Tunnel is directly proportional to "pck" of the throat material, and depends on the square of the operational temperature (i.e., the melt temperature, or the oxidation temperature, or the temperature at which the material loses significant strength, etc.). The effect of cooling is included in the "1/(q)<sup>2</sup>" term. If the heat-transfer rate can be reduced by a factor of 5 by injecting a coolant, then the Free-Piston Impulse Tunnel run time could be increased by a factor of 25. Cooling effects will be discussed in the next section.

A summary of the "pck T<sup>2</sup>" term (assuming that T is negligible compared to T<sub>m</sub>) for some common metals is given in the following table, based on the melt temperature (T<sub>m</sub>). Thermal data were obtained from Refs. A-6 - A-8.

Material	$T_m$ , ° F	$\sqrt{\rho c k} T_m$ , Btu/ft <sup>2</sup> √sec	$\rho c k T_m^2$ , Btu <sup>2</sup> /ft <sup>4</sup> sec
Aluminum	1,220	1,598	$2.55 \times 10^6$
Copper	1,981	3,373	$11.4 \times 10^6$
OFHC	1,981	4,522	$20.4 \times 10^6$
Molybdenum	4,752	5,344	$28.6 \times 10^6$
Steel (4130)	2,700	2,816	$7.9 \times 10^6$
Ta - 10W	5,425	3,361	$11.3 \times 10^6$
Tungsten	6,152	5,520	$30.5 \times 10^6$

The data in the table indicate that tungsten and molybdenum are superior materials, based on the melt temperatures. As mentioned before, this performance could probably be realized in a nitrogen atmosphere, but both of these metals oxidize, and the operational temperature should be limited to 2,000°F or so. In addition to the thermal properties, other important material characteristics required are a high yield strength, a low coefficient of expansion, and a high hardness.

The calculations in this section were made using constant thermal properties, constant heat-transfer rate coefficient (with wall temperature variations), and by assuming a semi-infinite solid heat conduction model. All of these assumptions can be removed by using the CMA code, Ref. A-9, to incorporate varying thermal properties and a finite thickness material, and by using the BLIMP code to predict the heat-transfer rate coefficient for different wall temperatures. This did not seem necessary at this point in the analysis.

### A3.0 TRANSPIRATION COOLING

#### A3.1 BACKGROUND

The summary of the heat sink potential of various candidate throat materials given in Fig. A-5 indicates that none of the materials is satisfactory for the severe test condition ( $p = 3,500$  atm,  $T_i = 9,700$  K). Even in a nitrogen atmosphere where no oxidation of the tungsten or molybdenum is present, the run time would not be more than 0.5 msec. It was the objective here to see if it is feasible

to cool the throat so that air could be used as the test gas at the severe ( $p_o = 3,500$  atm,  $T_o = 10,000$  K) test condition, with a run time of 1 msec or more.

A transpiration-cooled throat would be very expensive to build, and it would be desirable to use it for many runs (100 runs or more). If the throat were made of molybdenum, it would probably be necessary to keep the wall below  $2,000^\circ\text{F}$ . A copper wall would be limited to a temperature of  $1,500^\circ\text{F}$ . Referring to Fig. A-5, it may be seen that run times of only 0.04 to 0.05 msec could be made before these metals would reach their temperature limit if they were not cooled. However, by reducing the heat-transfer rate with cooling (film cooling or transpiration cooling) by a factor of 5, the run time could be increased by a factor of 25, giving run times of 1 to 1.25 msec. This extrapolation comes from the constant heat solution presented above.

### A3.2 BLIMP COOLING CALCULATIONS

Calculations were made using the BLIMP code, Ref. A-1, to determine if a factor of 5 reduction in peak throat heat-transfer rate is achievable, and to estimate the required coolant flow rates. Both air injection and helium injection runs were made. This analysis was made for the large ( $d^* = 0.75$  in.) Free-Piston Impulse Tunnel nozzle shown previously in Fig. A-3, at  $p_o = 3,500$  atm,  $T_o = 9,700$  K.

These calculations were all made with a wall temperature of  $5,200^\circ\text{R}$ , which is approximately the melting temperature of molybdenum. The original purpose in making these calculations was to see if it was feasible to maintain a molybdenum throat just below the melt temperature by injecting a relatively small amount of coolant. This approach was abandoned because of the problems associated with using a transpiration-cooled molybdenum throat at this temperature level, i.e., the molybdenum gets brittle when heated above  $2,500^\circ\text{R}$ , and it would be very expensive to build a complicated transpiration-cooled molybdenum throat which might not last. The  $T_w = 5200^\circ\text{R}$  calculations are used here to estimate the cooling effectiveness at a temperature of  $2,000 - 2,500^\circ\text{R}$ . Since the free-stream temperature ( $16,000^\circ\text{R}$ ) is much higher than either wall temperature, it is expected that the cooling efficiency would be about the same at both temperatures. BLIMP calculations will be made with the correct wall temperature, whenever optimization of the injectant flow distribution is made.

#### Air Injection

The effect of injecting air into the throat region of the  $d^* = 0.75$  in. Free-Piston Impulse Tunnel throat is shown in Fig. A-6. A scaled sketch of the throat is presented at the top of the figure. At the test conditions shown here, the boundary layer will be turbulent at the beginning of the nozzle, based on a momentum thickness Reynolds number of 250 at the first station. The boundary-

layer transition point assumed for the BLIMP calculations is shown in the nozzle sketch ( $x = 0.21$  in.). The air was injected at a constant rate throughout the nozzle beginning at  $x = 0.32$  in. Calculations were made for injection rates of 30 and 60 lb/ft<sup>2</sup>-sec.

In the absence of cooling, a peak turbulent heat-transfer rate of 230,000 Btu/ft<sup>2</sup>-sec is indicated, at a location slightly upstream of the throat. Air injection at a rate of 60 lb/ft<sup>2</sup>-sec will reduce the peak throat heat-transfer rate by a factor of 6 or so, to a peak heat-transfer rate of 36,000 Btu/ft<sup>2</sup>-sec. Note that the high heat-transfer rates near the boundary-layer transition point can be reduced by altering the distribution of the air injection. Optimization of the coolant injection distribution has not been done. The air injection results are summarized below:

$\dot{m}_{inj}$ , lb/ft <sup>2</sup> -sec	Peak $\dot{q}$ Btu/ft <sup>2</sup> -sec	Integrated Mass Flow Rate (lb/sec) at $x = 2.60$ in.	Percent of Throat Mass Flow	Percent of Boundary-Layer Mass Flow
0	230,000	0	0	0
30	123,000	1.35	1.72	21.5
60	36,000	2.70	3.44	43.0

The mass flow rate through the throat is 78.6 lb/sec and the mass flow through the uncooled boundary layer at  $x = 2.60$  in. is 6.23 lb/sec. It appears that the cooling could be cut off or reduced drastically at  $x = 2.60$  in. (Fig. A-6), but this will have to be determined when the coolant distribution optimization runs are made. The results in the table indicate that the required reduction in heat-transfer rate could be made by injecting air at a rate of 3.5 percent of the mass flow going through the throat.

### Helium Injection

Helium injection and air injection calculations are compared in Fig. A-7 for the same flow situation described above ( $d^* = 0.75$  in. nozzle,  $p_{in} = 3,500$  atm,  $T_{in} = 9,700$  K). However, the BLIMP calculations were very difficult to run, and in order to get convergent solutions, it was necessary to adjust the coolant injection distribution until finally the distribution shown at the top of the figure was used. The coolant distribution is obviously not a practical one — with reduced coolant flow rates right at the peak heat-transfer rate location. Further work on these calculations is needed, and the coolant injection distribution needs to be optimized.

Nevertheless, the direct comparison given in Fig. A-7 indicates that helium cooling is much more effective than air cooling whenever the same weight of gas is injected.

#### Transpiration-Cooled Throat

A sketch of a possible approach to designing a transpiration-cooled throat is given in Fig. A-8. The coolant would be injected through a series of very small passages which are etched into very thin platelets as shown in Section A-A. The platelets are then diffusion bonded together to give a composite structure as strong as the original material. Most any coolant injection distribution could be obtained by varying the size and number of cooling passages.

Injecting a fluid into the throat region of the Free-Piston Impulse Tunnel against the high pressures there could be a problem. For the severe case considered, the pressures on the aerodynamic side of the throat vary from 3,500 atm on the upstream side, down to 150 atm on the downstream side. Since the coolant in the small passages flows through 2-D sonic throats, the pressure in the coolant reservoir must be equal to about twice the highest aerodynamic pressure, i.e., 7,000 atm. The best way of generating this pressure is through a gunpowder-driven piston, similar to that used for TCNT tests in the range (or similar to the light-gas gun), see Fig. A-8.

The feasibility of this approach needs to be investigated to see if the platelet structure can withstand the high pressure loads (7,000 atm), and the high shear loads. Also, the flow rates need to be estimated. Undoubtedly, the throat would be very expensive.

#### A4.0 CONCLUDING REMARKS

1. Operation of the Free-Piston Impulse Tunnel at the extreme reservoir conditions being considered will result in intense throat heating. This situation is summarized in the following table, where the peak, cold-wall, heat-transfer rate is given for some of the more severe conditions:

Test Conditions	$p_{00}$ , atm	$T_{00}$ , K	$T_w = 540^\circ\text{R}$ $\dot{q}$ (Btu/ft <sup>2</sup> -sec)
a	10,000	10,000	756,600
b	4,000	10,000	368,600
c	3,500	9,700	310,200
d	1,800	9,000	165,300
e	1,000	7,280	76,800

BLIMP code calculations of the heat-transfer rate compare well with the limited experimental data available from high-performance test facilities, and were used extensively for the predictions here.

2. A heat sink conduction-heating approach, where the throat absorbs the intense (but short) heat pulse, can be used at the lowest test condition (test condition "e" in the table above) using a pure molybdenum throat. This approach has been explored in depth at GALCIT T5, (Refs. A-6 and A-10) and more recently at the High Enthalpy - Gottingen (HEG) Shock Tunnel in Germany (Ref. A-10). Throats made of beryllium-copper, Narloy-Z, tungsten, TZM, etc., were tried at GALCIT T5 before pure molybdenum was chosen. Until new materials (or coatings) are developed with a higher " $\rho c k T^2$ " (with other acceptable properties such as high hardness, high strength, and low coefficient of thermal expansion), it appears that the heat sink approach is limited to throat heat-transfer rates of 80,000 – 100,000 Btu/ft<sup>2</sup>-sec, with run times of 2 msec. Cooling of the nozzle throat, or possibly the use of an ablating throat, will be necessary for the more severe test conditions in the Free-Piston Impulse Tunnel.
3. A thermal analysis indicates that transpiration cooling could be used with either air or helium coolants to reduce the throat heat-transfer rates to acceptable levels for 1- to 1.25-msec runs in the large Free-Piston Impulse Tunnel throat, at reservoir conditions of  $p_0 = 3,500$  atm,  $T_0 = 9,700$  K. A sketch (Fig. A-8) of a possible hardware approach to a transpiration-cooled throat is given, with pressurization to 7,000 atm in the coolant reservoir being generated by a gunpowder-driven piston, and with the coolant flowing through very small 2-D sonic throats etched in platelets. Even though the thermal analysis indicates that transpiration cooling is a possible approach for some of the severe test conditions, several aspects of this approach need to be evaluated:

Will the diffusion-bonded platelets be able to carry the pressure/shear loads imposed on them at the operating temperature of the throat?

Can the coolant flow rates and distribution be obtained?

What will a throat section cost? Even if one throat were relatively cheap, an expensive development effort could be required, with the loss of several throats during the process. The run time of the facility will have to be controlled closely, so that the expensive transpiration-cooled throat is not damaged.

Will one transpiration-cooled throat design suffice for a range of test conditions?

What is the effect of the injected coolant on the free-stream flow? Even though mass injection rates of only 3-1/2 percent of the total throat mass flow are being suggested, this is 44 percent of the mass flow through the very thin, uncooled boundary-layer flow. This could cause boundary-layer separation (a "blown" boundary layer), and result in flow gradients in the test section. The relatively cold air or helium injectants will contaminate the free stream to at least a mild extent.

A transpiration-cooling expert of the caliber of Mr. Hank Moody of ATSS should be involved in many of the items listed above. Computer calculations with a fully viscous layer code could indicate contamination effects.

4. Some of the problems of the transpiration-cooled throat would not be present in a film-cooled throat. An example of a film cooling experiment in an arc facility is shown in Fig. A-9 and described in Ref. A-11. The film-cooled throat structure would be stronger, high coolant flow injection rates should be feasible, and the rates would be easier to vary. A film-cooled throat would also be cheaper. However, film cooling is not as thermally efficient as transpiration cooling, and higher coolant injection rates would be necessary. This might be the most practical approach for the Free-Piston Impulse Tunnel. Estimates of the cooling effectiveness of film cooling need to be made.
5. It is also possible that an ablating material of some kind might be a reasonable choice for some part of the operating envelope of the Impulse Tunnel. Graphite, carbon phenolic, etc., are candidate throat materials. However, the large pressures and shears involved in the Free-Piston Impulse Tunnel operation (at severe test conditions) might make this choice impractical. This needs to be investigated.

## REFERENCES

- A-1. Evans, R. Michael. "Users' Manual - Boundary Layer Integral Matrix Procedure, Including Gas Phase Kinetics - KBLIMPA." Aerotherm UM-75-62, March 1975.
- A-2. Noonan, Barry J. and Rand, James L. "Recent Heat Transfer Measurements at High-Stagnation Enthalpy and High Reynolds Number." Sixth BOWACA Symposium at National War College, Fort McNair, Washington, DC, October - November 1963 (also see NOL TR-63-276).
- A-3. Enkenhus, K. R. and Maher, E. F. "The Aerodynamic Design of Axisymmetric Nozzles for High-Temperature Air." NAVWEPS Report 7395, February 1962.

- A-4. Powars, Charles A. and Kendall, Robert M. "Users' Manual – Aerotherm Chemical Equilibrium (ACE) Computer Program." Aerotherm UM-69-7, May 1969.
- A-5. Schneider, P. J. *Temperature Response Charts*. John Wiley & Sons, Inc., New York and London, 1963.
- A-6. Brouillette, Martin "Design Modifications to T5 and Their Implementation." GALCIT Report FM 91-3. 1991.
- A-7. Rohsenow, Warren M. and Hartnett, James P. "Handbook of Heat Transfer." McGraw-Hill Book Co., 1973.
- A-8. Authors Unknown. "Mach 10 to 20 Electrothermal Wind Tunnel Feasibility Study and Demonstration." GASL TR 342, Final Report, Vol. I.
- A-9. Schoner, Robert J. "Users' Manual - Aerotherm Charring Material Thermal Response and Ablation Program - Version 3." AFRPL-TR-70-92, April 1970.
- A-10. "CALTECH T5 Produces High Flow Enthalpies." *Aviation Week and Space Technology*, September 14, 1992.
- A-11. Lewis, Henry F and Horn, Dennis D. "A Film Cooling Experiment on a Convergent-Divergent Nozzle." AEDC-TR-66-78, June 1966.

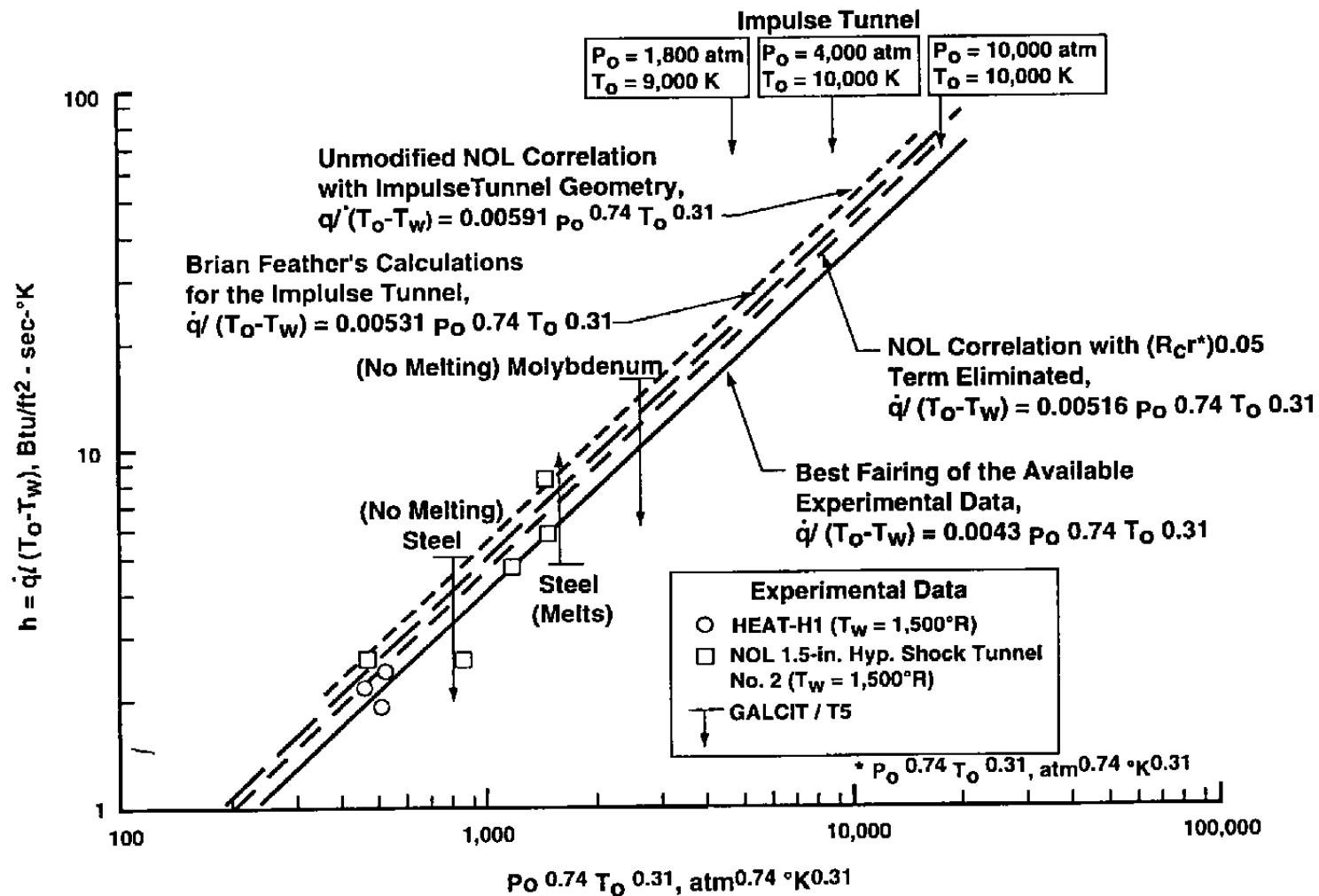


Figure A-1. Correlation of throat convective heat-transfer rates for high-performance facilities.

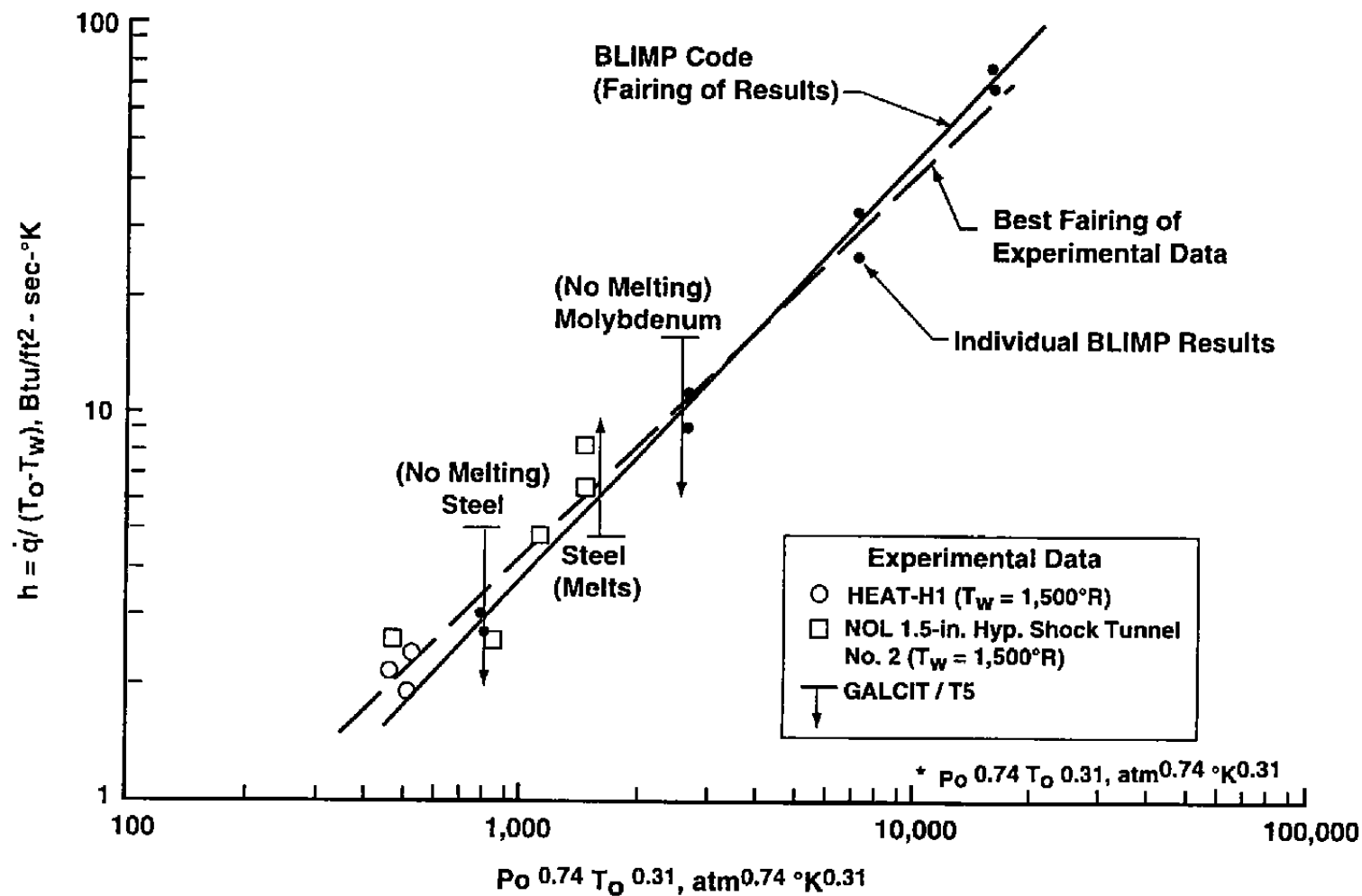


Figure A-2. Comparison of experimental data and BLIMP code calculations.

All Dimensions in Inches

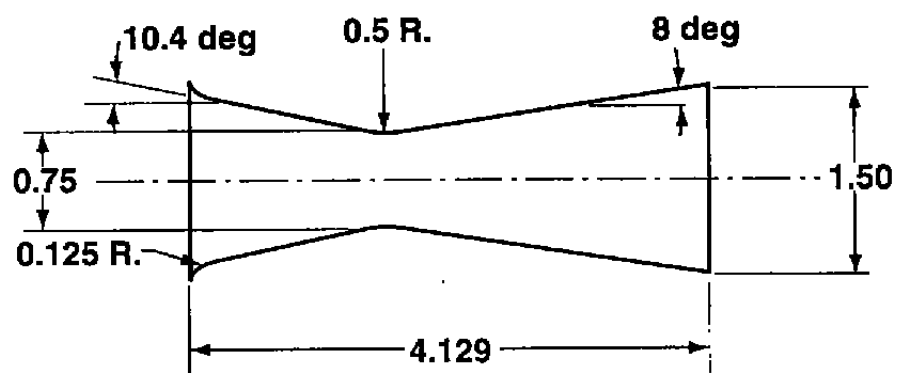


Figure A-3. Aerodynamic contour of the large throat for the Impulse Tunnel.

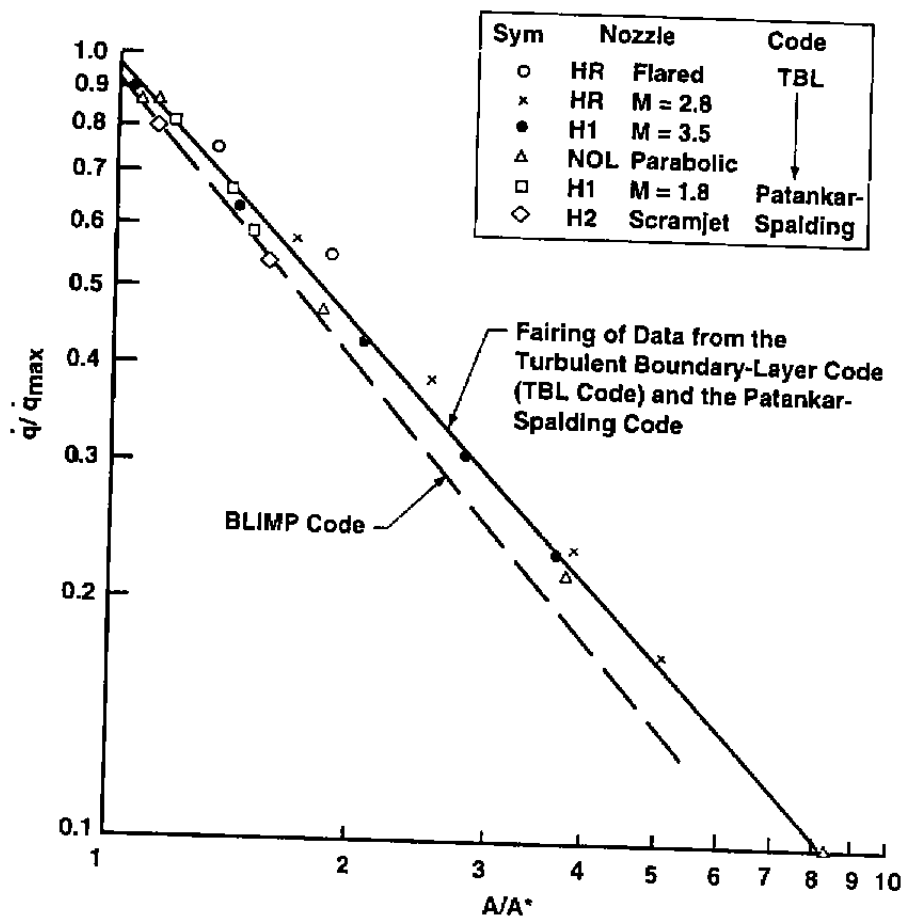


Figure A-4. Correlation of throat convective heat-transfer rate distributions in the supersonic part of the nozzle.

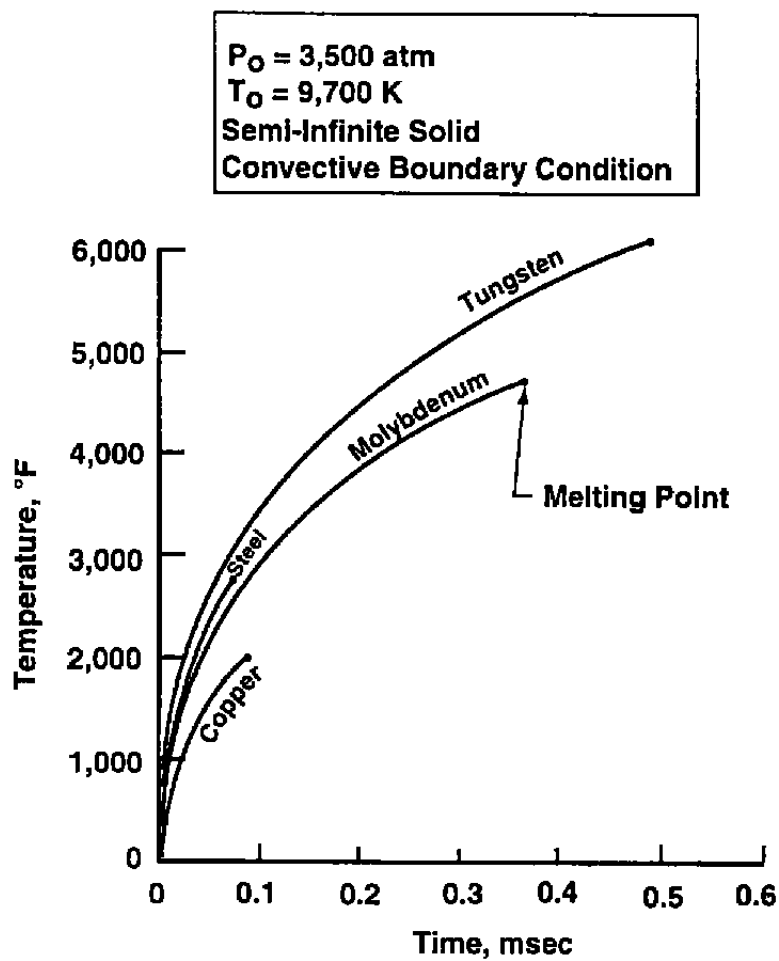


Figure A-5. Temperature rise in various throat materials for a severe test condition.

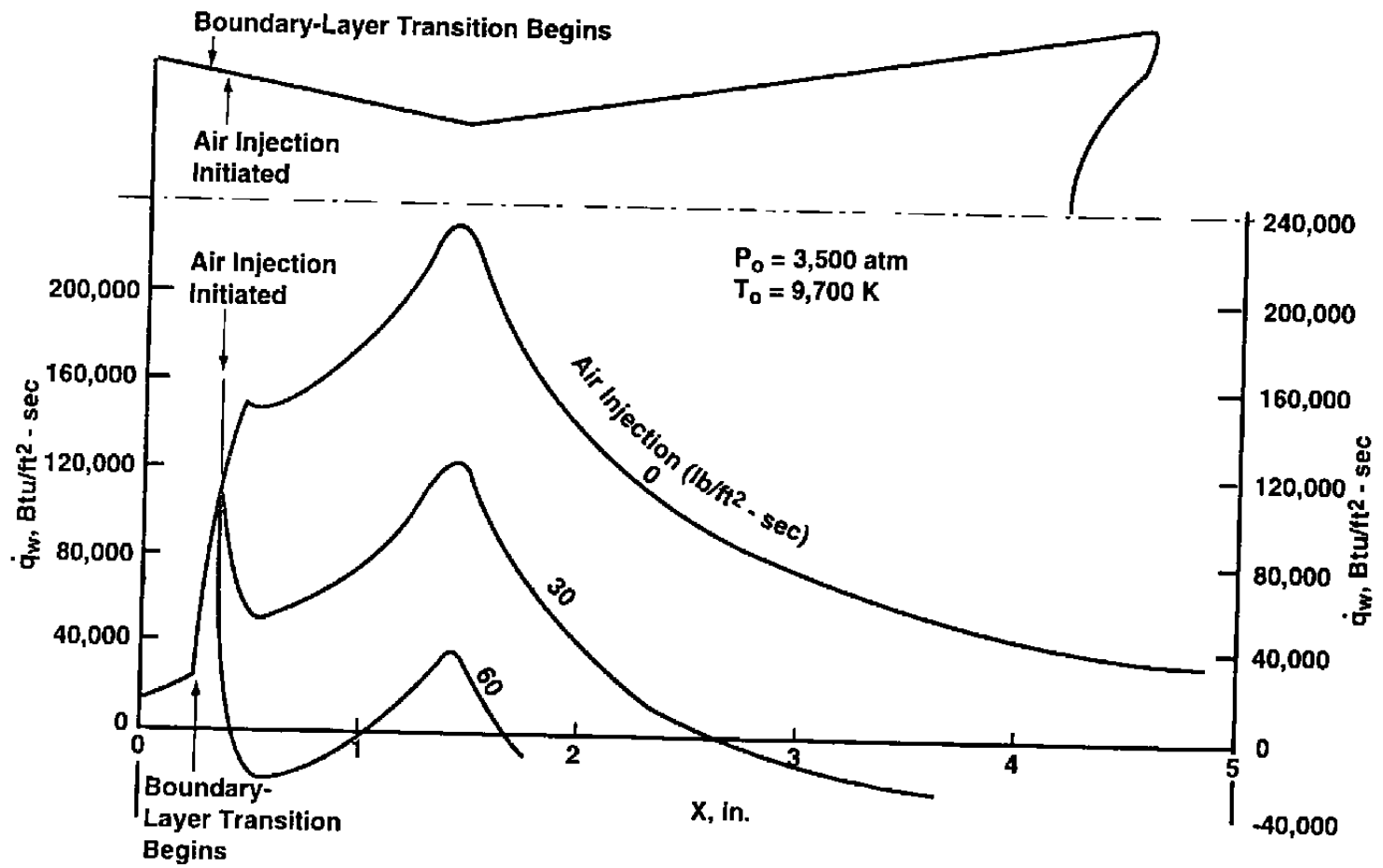


Figure A-6. Reduction in the hot wall ( $T_w = 5200^\circ\text{R}$ ) heat-transfer rate by air injection.

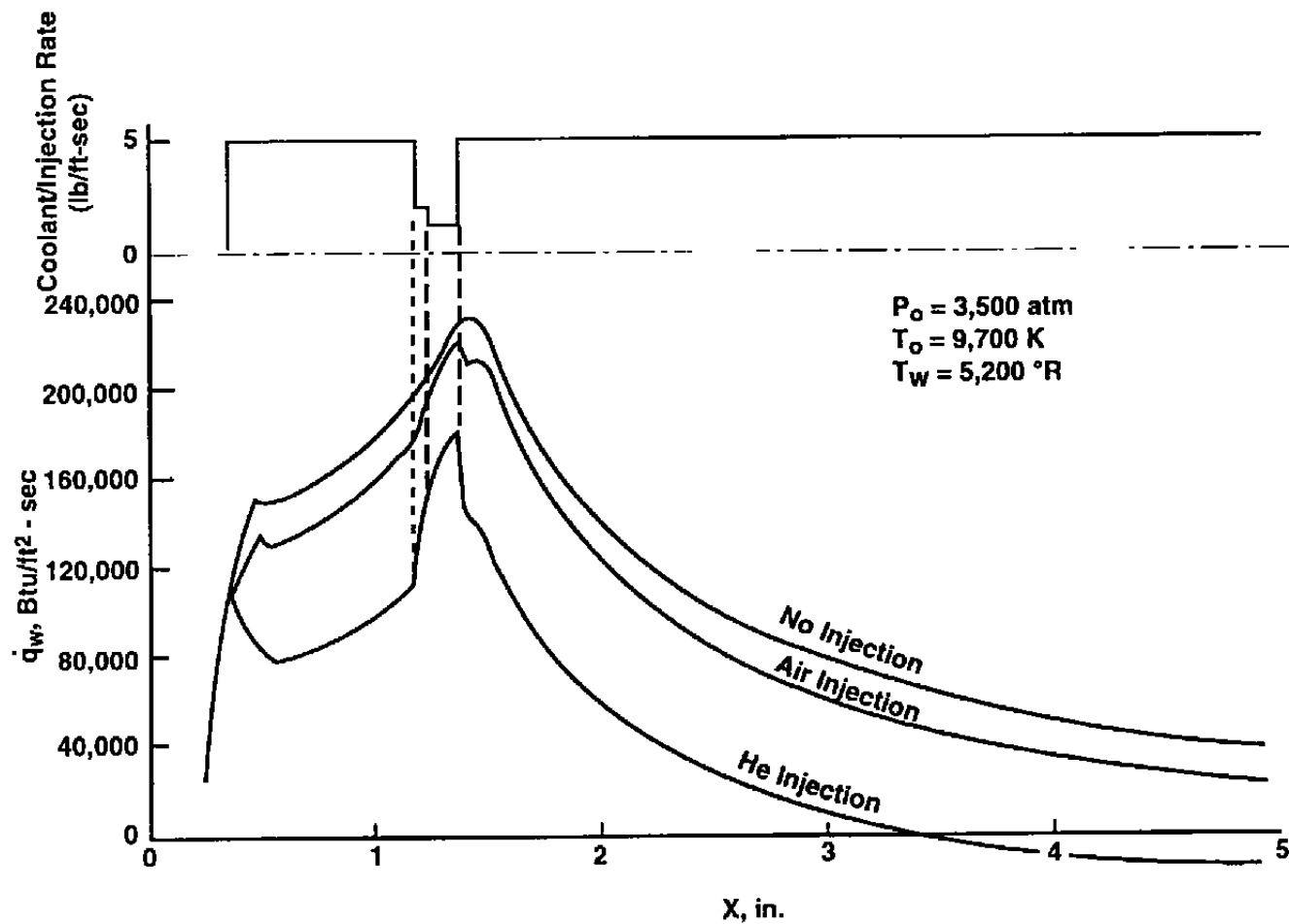


Figure A-7. Relative effectiveness of helium and air coolants.

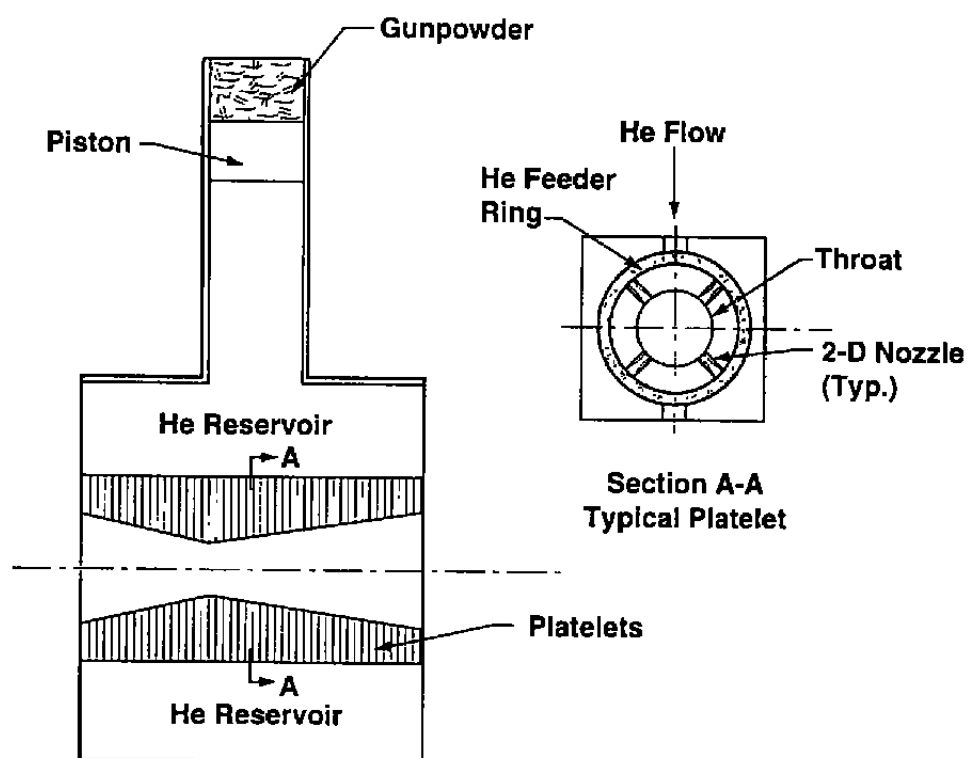


Figure A-8. Transpiration-cooled throat.

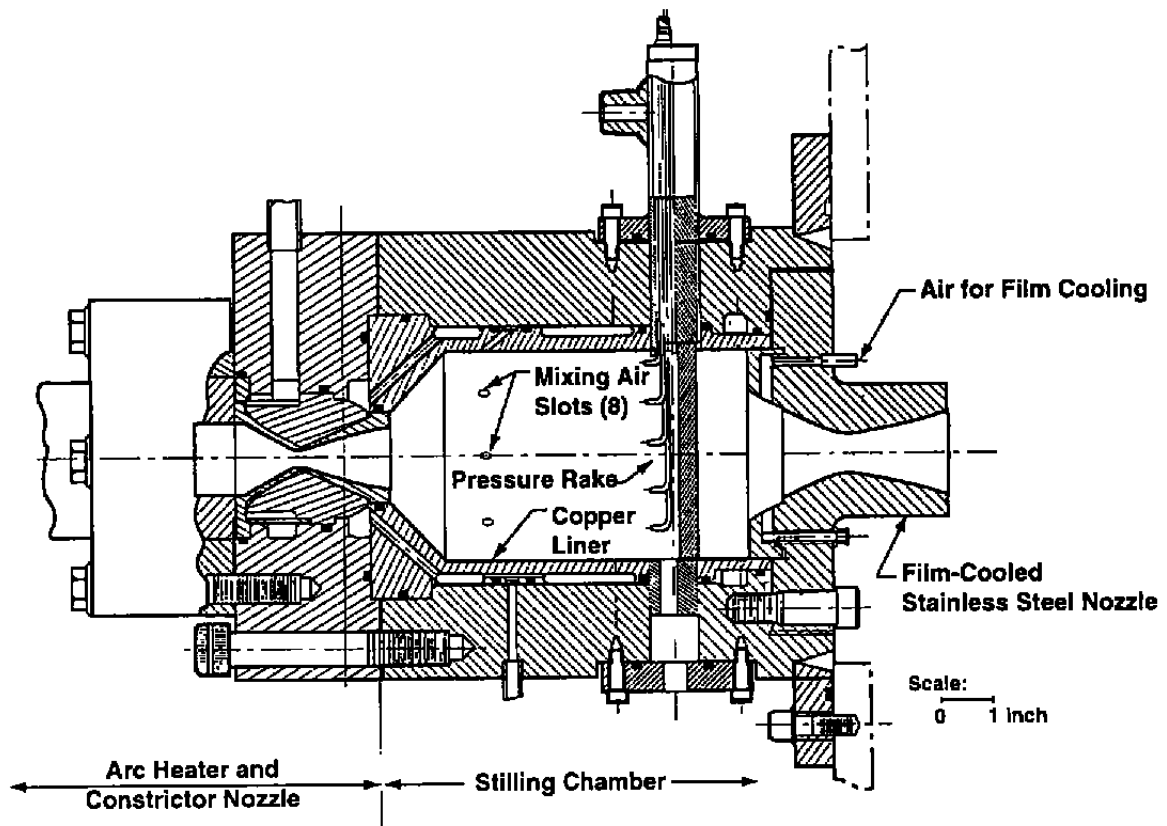


Figure A-9. The film-cooling experiment of Lewis and Horn in an arc heater (Ref. A-11).

## NOMENCLATURE

$A_{ex}$	Area of nozzle exit
$A^*$	Area of nozzle throat
BUS	Bus control subsystem
CI	Typical cone model pressure gage identification
CFD	Computational fluid dynamics
$C_h$	Heat-transfer coefficient
$c_p$	Specific heat at constant pressure
$C_p$	Pressure coefficient
E	Energy
ECS	Event control subsystem
Fansteel-60	Tantalum alloy (90-percent Ta, 10-percent W)
FCS	Fire Control Subsystem
GALCIT	Graduate Aeronautical Laboratories California Institute of Technology
GDACS	Data Acquisition and Control System
H5	Theoretical reflected shock enthalpy
H5'	Calculated reservoir enthalpy
HCS	Host Computing Subsystem
$H_o$	Nozzle stagnation enthalpy
HPS	High-pressure section

HPS2	Pressure gage upstream of high-pressure diaphragm
$K$	Thermal conductivity
$L$	Model length
LVDT	Linear voltage differential transformer, measuring facility recoil
$M_c$	Mach number at nozzle exit
$M_s$	Shock tube Mach number
$P$	Pressure
$P^*$	Pressure at nozzle throat
$P_1$	Initial shock tube charge pressure
$P_2$	Initial compression tube charge pressure
$P_4$	High-pressure section diaphragm burst pressure
$P_5$	Theoretical reflected shock pressure
$P_5'$	Measured reservoir pressure
PLIF	Planar laser-induced fluorescence
$P_o$	Nozzle stagnation pressure
PT	Pump tube
PT4	Typical pitot rake pressure gage identification
$Q \text{ DOT}$	Heat-transfer rate
$R_c$	Rockwell hardness
$R_g$	Diaphragm groove radius

$R_i$	Inside radius of hemispherical diaphragm
RMT	Remaining metal thickness at groove base
$R_o$	Outside radius of hemispherical diaphragm
$r_s$	Isentropic compression ratio
S	Surface distance
S5	Theoretical reflected shock entropy
SDS	Static Data Subsystem
ST	Shock tube
ST1	Typical shock tube pressure gage designation
$T$	Temperature rise of coaxial thermocouple
T1	Typical coaxial thermocouple identification
$T_3$	Initial helium temperature
$T_4$	Helium temperature at diaphragm burst
T5	Theoretical reflected shock temperature
T5*	Calculated reservoir temperature
$T_b$	Diaphragm petal thickness at base
$T_c$	Diaphragm crown thickness
TDS	Transient data subsystem
$T_m$	Material melt temperature
TMS	Time Measurement Subsystem

TZM	Molybdenum alloy
U	Test flow velocity
$U^*$	Velocity at nozzle throat
$U_e$	Velocity at nozzle exit
V	Specific volume
$V_f$	Final helium volume at diaphragm burst
$V_i$	Initial helium volume in compression tube
X	Axial location
$X_o$	Monatomic oxygen mole fraction
$\gamma$	Ratio of specific heats for helium
$\rho$	Material density
$\rho_e$	Density at nozzle exit